A GENERAL THERMAL THICKNESS MODEL AND A HEATING RATE RELATED IGNITION CRITERION FOR COMBUSTIBLE SOLIDS

by

Ning Tian

A dissertation submitted to the faculty of
The University of North Carolina at Charlotte
in partial fulfillment of the requirements
for the degree of Doctor of Philosophy in
Mechanical Engineering

Charlotte

2013

Approved by:

_____
Dr. Aixi Zhou

_____
Dr. Harish Cherukuri

_____
Dr. Jozef Urbas

_____
Dr. Gloria D. Elliott

_____
Dr. Jing Zhou

ABSTRACT

NING TIAN. A general thermal thickness model and a heating rate-related ignition criterion for combustible solids (Under the direction of DR. AIXI ZHOU)

The objective of this research is to investigate the ignition behavior of combustible solid materials in fire. Three key tasks were conducted for it: (1) a new theoretical temperature profile prediction model, referred as General Thermal Thickness (GTT) model, was proposed and then validated by the experimental data from E-glass/polyester composite panels at different heat fluxes; (2) a new ignition criterion (the Heating Rate-related Ignition Temperature (HRIT) criterion) was proposed and its accuracy under various heat fluxes was shown by comparing with experimental data of different materials; (3) uncertainty and sensitivity analyses were conducted on a new integrated ignition prediction model (i.e. the GTT combined with the HRIT ignition criterion), to investigate the variations in ignition and identify key affecting factors.

A simplified heat transfer model was constructed and solved in order to theoretically predict the temperature profile of the GTT combustible solid materials subjected to one-sided heating. The theoretical solution of the GTT model was validated by experimental data from intermediate-scale calorimeter fire tests of E-glass fiber reinforced polyester composite panels at three heat flux levels. The GTT model was also verified by results from finite element modeling predictions. Compared with the classical theoretical models (such as thermally thick (TTK) and thermally thin (TTN) models), the GTT model is more accurate and it is valid through the whole range of thermal thickness.

Since existing ignition criteria cannot handle the variations of external heat flux and surrounding environmental conditions, a new ignition criterion referred as Heating Rate-related Ignition Temperature (HRIT) criterion, was proposed, developed and validated. In the new HRIT ignition criterion both the surface temperature and its increasing rate are used to determine ignition. The accuracy of the HRIT ignition criterion under different external heat fluxes was validated by the piloted ignition data of a thermoplastic material (Black PMMA), a thermoset composite material (E-glass fiber reinforced polyester composite) and a cellulosic material (Red Oak) subjected to different external heat fluxes. The adaptability of the HRIT criterion in different surrounding environmental conditions was also discussed.

Both local and global sensitivity and uncertainty analyses were performed to understand the variations and identify important factors affecting the ignition process. First, the local sensitivity analysis was applied to the GTT model and the HRIT criterion separately. Then a Monte Carlo analysis using the Latin Hypercube Sampling method was performed on the integrated ignition prediction model (the GTT model combined with HRIT ignition criterion), yielding the global sensitivity coefficients (or important index) and uncertainty ranges of the ignition.

In summary, unlike classical temperature profile prediction models such as thermally thick or thermally thin models whose applications are restricted by thermal thickness, the new GTT model proposed in this research is valid within the whole range of thermal thickness. The challenge of the existing ignition criteria handling varying heat fluxes and surrounding environment was resolved by the new HRIT ignition criterion, and the accuracy of the HRIT criterion was validated by experimental data from three materials. The important affecting factors and

uncertainties during ignition process were identified in this research through the uncertainty and sensitivity study, which can serve as a guideline for fire safety design.

ACKNOWLEDGEMENTS

First, I want to thank Dr. Aixi Zhou, my academic advisor, spiritual mentor, and brother. It is a great joy to work with Aixi. I first met with Aixi in 2011, and was introduced into the field of fire safety science and engineering. Since then Aixi like a torch always lightens the road of my academic world using his profound knowledge and insightful logic with constant enthusiasm and patience. I cannot thank him enough.

I also would like to thank Dr. Harish Cherukuri, the co-chair of my committee, for his service and kind encouragement. I learned so much from him about the numerical method, finite element method, and solid mechanic.

My special thanks go to Dr. Jozef Urbas, the member of my committee, for his discussions and guidance in my research. His broad knowledge and insightful thinking inspired me every time when I confronted with troubles in my research.

I want to thank Dr. Gloria D. Elliott, the member of my committee, for her help and kind suggestion. I am impressed by her knowledge and kindness. I appreciate her service and efforts in the committee so much.

Also I want to thank Dr. Jing Zhou, the member of my committee, for her kindness and inspiration. She is always ready to help.

Finally but most importantly, I want to thank my wife, my father and mother, my father-in-law and mother-in-law, my relatives and friends for their love, support, and encouragement. It is you make me the happiest man in the world.

TABLE OF CONTENTS

LIST OF TABLES

LIST OF FIGURES

LIST OF SYMBOLS

A	the rate constant [1/s]
Bi	Biot number [--]
c	heat capacity [$\mathrm{J/(kg\ K)}$]
E	activation energy [J/kg.mol]
h	the heat convection coefficient [$\mathrm{W/(m^2\ K)}$]
H	effective heat of combustible gas [J/kg]
L	thickness of the slab [m]
L_v	total heat of gasification [kJ/kg]
$\dot{m}''$	the mass flux [$\mathrm{kg/(m^2\ s)}$]
$\dot{q}''$	the heat flux [$\mathrm{W/\ m^2}$]
$\dot{Q}(x,t)$	the effective heat source or sink within the solid [$\mathrm{W/m^3}$]
Q_s	the heat of sold decomposition per unit mass [$\mathrm{kJ/kg}$]
Q_m	the heat of moisture desorption per unit mass [$\mathrm{kJ/kg}$]
R	gas Constant 8.314 [kJ/(K.mol)]
$STIR$	surface temperature increasing rate [K/sec]
T	the temperature [K]
$\dot{T}$	temperature rate [K/s]
v	Velocity [m/sec]
α	equal to $\frac{\lambda}{\rho C}$
β	constant related to ignition [sec/K]
ϵ	shift coefficient [--]
ε	the emissivity of surface (--)
δ	$= \mathrm{STIR_{ig}} - \mathrm{STIR_{ig}^c}$ [K/sec]
σ	Stefan-Boltzmann constant [$5.67 \times 10^{-11}\mathrm{kW/(m^2K^4)}$]

ρ	density [kg/ m^3]
λ	thermal conductivity [w/(m K)]
μ	the separation constant or eigenvalues

Subscript

ch	char
cr	critical
e	external
eff	effective
F	flame
g	gas
ig	ignition
i	initial
m	moisture
min	minimum
n/N	integer (1,2,3…)
net	net
o	original
r	radiation
s	solid
surf	surface

Superscript

cr	critical
inf	infinite

LIST OF ABBREVIATIONS

CC	Pearson correlation coefficient
CCDF	complementary cumulative distribution function
CDF	cumulative distribution function
CPIC	condensed phase related ignition criterion
HRIT	heating rate-related ignition temperature
GPIC	and the gas phase related ignition criterion
GTT	general thermal thickness
MPs	material properties
MLR	mass loss rate
PCC	partial correlation coefficient
RCC	rank Pearson correlation coefficient
PRCC	partial rank correlation coefficient
SA	sensitivity analysis
SRRC	standardized rank regression coefficients
SRC	standardized regression coefficients
STIR	surface temperature increasing rate
TTK	thermally thick
TTN	thermally thin
UA	uncertainty analysis

CHAPTER 1: MOTIVATION AND BACKGROUND

1.1. Motivation

The subject of ignition is fundamental to fire science and of great practical importance. The ignition is referred to the initiation of the combustion which is a chemical process of oxidation that occurs at a rate fast enough to produce temperature rise and usually light either as a glow or flame [1]. From fire safety perspective, ignition is essentially important not only because it is the initiation of a fire (the commencement of dramatic release of heat, smoke, CO/CO_2 and dramatic consumption of O_2,) but also because it plays a significant role in the growth of fire. According to different standards, the ignition can be classified into different categories. In general the ignition can be categorized as desired (such as the ignitions in engines) and undesired ignition (such as accidental fires). Depending on whether a flame exists or not, ignition be classified as smoldering ignition [2] and flaming ignition, and based on whether a pilot exists, the ignition be classified as spontaneous ignition and piloted ignition.

The focus of this research is to investigate and predict the piloted flaming ignition of combustible solid materials subjected to an external heat source theoretically for the fire safety purpose because: (1) piloted flaming ignition occurs at a lower threshold value; (2) the spread of fire between objects and the flame spread over continuous fuel surfaces are both piloted ignition process; and (3), in practice, it is usually impossible to excluded all possible external pilot sources [3].

1.2. Mechanism of Piloted Ignition

The piloted flaming ignition mechanism has been intensely investigated since the fire science began. Initially it was believed that the piloted flaming ignition would occur when the surface temperature of the solid material exceeded a certain value. The Fire Triangle is a simple model for understanding the necessary ingredients for fires. In Fire Triangle model, the three elements a fire needs to ignite was summarized in [4] as: (1) the substance must be sufficiently heated so that an adequate concentration of pyrolysate exists at some location away from the surface; (2) an adequate concentration of an oxidizer (typically, air) must be mixed in with the fuel vapors so that a flammable fuel/oxidizer gas mixture exists somewhere above the surface; (3) either the temperature of the pyrolysate/air mixture must become high enough or else a sufficient external energy source such as a pilot flame or a spark must be introduced (for piloted ignition to occur). Now most researchers agree the mechanism of piloted flaming ignition of solids as that the piloted ignition will take place when the lower flammability limit (LFL) of combustible gases from pyrolysis is attained at the location of the pilot, as summarized in In the Society of Fire Protection Engineer Handbook of Fire Protection Engineering (Chapter 2-11 [5]).

To illustrate the mechanism of piloted ignition clearly, the piloted ignition process of a combustible slab with general thermal thickness subjected to one-side external heat flux is described as following (FIGURE 1.1). First the surface of the solid will absorb the majority of energy when heat is transferred into the solids by radiation or convection from an external heating source. The remaining fraction of energy can be absorbed in-depth, transmitted through the materials or reflected (Pages 305-308, [6]). The temperature of the solid increases as energy is taken in. The solid will also convect and re-radiate energy into the gas phase. Meanwhile, at certain

temperatures, moisture vapor and pyrolysis volatiles will be generated and then transferred into gas phase(Chapter 1, [7]). The vaporization and pyrolysis usually are endothermic.

Flashing starts at the moment when the LFL of combustible gases is achieved at the location of the pilot. If the concentration of combustible gas above the LFL is sustained, stable flaming combustion can be achieved. After ignition, a portion of the energy generated from the flame accumulates in the reaction volume as a temperature rise of the volatile-air mixture and a portion is lost to the surrounding environment and solid by convection and radiation. The flaming material becomes an external heating source for other un-ignited materials, thus leading to further fire growth.

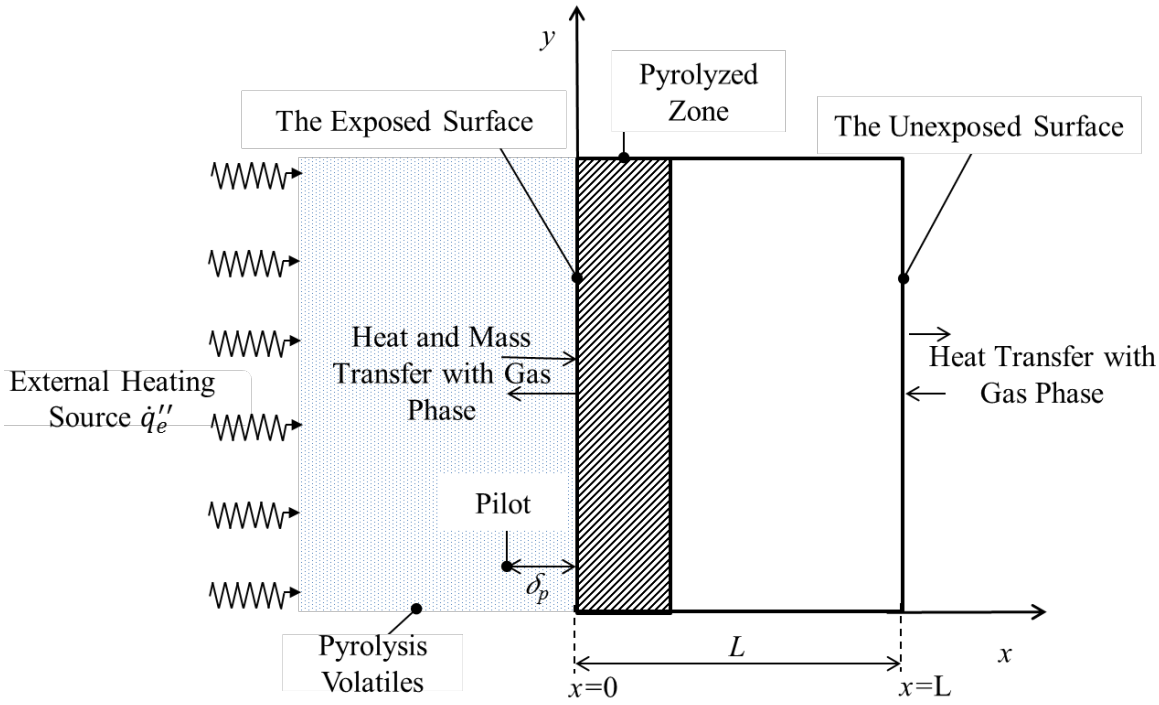

FIGURE 1.1: Schematic of ignition process of combustible solids

1.2.1. Mathematical Model of Ignition Process

The mathematical description of the ignition process goes into two directions: one is the simplified model and the other is the comprehensive model. In simplified model, the closed-form solution is obtained for the daily engineer calculation use. For the comprehensive model, numerical solution is required.

Lots of efforts were made towards to the two directions. In the comprehensive model direction, Bamford [8] in 1946 presented a model to calculate the temperature profile and pyrolysis of wood slab subjected to symmetrically heat by a flame on each face, assuming the energy was only absorbed by the surface. The pyrolysis rate was simulated by unimolecular law and the gas phase was not considered in Bamford's model. Realizing the importance of the gas phase and in-depth absorption of the incident radiation in solid phase, Kashiwagi [9] proposed a comprehensive model which could take these two factors into account. In Kashiwagi's model, the gas phase was described by four governing equations: mass conversation, energy conservation, fuel species conservation, and oxidizer species conservation. The in-depth incident radiation was modeled by Beer's Law. The movement conservation of gas phase was not included in Kashiwagi's model. It was concluded by Kashiwagi that the effect of the pyrolysis of a solid fuel is negligible on the radiative ignition. To examine the different ignition criteria, Gandhi [10] developed a more comprehensive model, in which the movement behavior of gas phase was included and the pyrolysis of solid phase was modeled by the Arrhenius Equation. Gandhi concluded that the reversal of the gas temperature gradient at the solid-gas interface was a necessary condition for ignition to occur. In 1998, Atreya [3] gave a comprehensive review of ignition. The moisture effect was considered in the solid phase, and solid-gas phase boundary layer was well defined.

It can be seen that the comprehensive models include the mathematically description of the complex physical and chemical processes which are involved in both solid and gas phases. These coupled differential equations need to be solved simultaneously, thus theoretically solutions are not possible. The numerical solution becomes the only option, such as the finite element method (FEM). One can obtain fairly accurate temperature profile such as the work presented in [11], in which the material properties changes according to temperature increasing was also considered. However, special expertise and effort in numerical implementation are required. Hence a comprehensive mathematical model is not suitable for the daily design calculation.

Because of its simplicity, the simplified model is more suitable for the daily design calculation. Lawson and Simms [12] were the pioneers to use the inert-heating equation as a starting point to study the ignition behavior of wood. In their model, they assumed that the back surface temperature of specimens was constant (or the thickness of the specimen was semi-infinite) and the temperature of air remained unchanged during the ignition process. This model is referred to as the thermally thick model (TTK) and it is popular model in use now. However, this theoretically solution of TTK model is complex to use. Thus an approximation of this solution was derived for sufficiently long TTI prediction in [12]. But this approximation solution was not accurate for experimental data with short or intermediates TTI. Hence the approximation solution for short TTI cases was proposed in [13]. To cover the whole range of TTI, a piecewise-continuous approximation was proposed to cover the whole range of TTI in [14]. Using a statistical approach, a simple approximation solution with a wide range of TTI for theoretical solution of TTK was developed in [15]. These approximate solutions of TTK model, as simple and useful tools, can be used in

analyzing fire tests experimental data and design calculations such as in [16, 17]. Atreya [18] gave a closed-form solution of the TTK model with the pyrolysis effects taken into account by Arrhenius Equation. However the solution is quite complicated for day-to-day use.

Another classical simplified theoretical model is thermally thin (TTN) model, in which the temperature gradient across the thickness direction is assumed to be zero. This assumption simplifies the solution of TTN model.

The thermal thickness of the solid materials can be cauterized by Biot number. The Biot number is defined as Equation 1.1.

$$Bi = hL/\lambda \qquad \text{Equation 1.1}$$

where h is the heat convection coefficient, L is the thickness of the material, λ is the heat conductivity of the material.

If *Bi* of a material is much less than 1, the solid can be considered as thermally thin. If *Bi* is much larger than 1, the solid can be considered as thermally thick [19]. In practice, the fire protection engineers need to use their own experience to decide whether *Bi* of a material in the specific application can be considered as much less or larger than 1.

When the actual thermal conditions are closely approximate to either the TTK or TTN assumptions, the predictions can be acceptable for fire safety design purpose. However, in many practical cases, the thermal thickness of materials is intermediate, which is not thick enough to be considered as semi-infinite or thin enough to assume zero temperature gradient. Some empirical correlations were proposed for intermediate thermal thickness material in [20-22]. These correlations are not physical base, and validated only for the specific conditions. Hence it is hard to extend the empirical correlations to different conditions.

To summarize, the existing TTK and TTN models over simplify the geometry effects of the material, and the intermediate thermal thickness models are not general enough for the fire safety design purpose. In addition, the definition of the thermal thickness is not clear enough to apply. Hence a simple and physic-based model, which can be applied to the material with General Thermal Thickness (GTT), without the need to categorize the thermal thickness, is in an urgent need for daily fire protection design.

1.2.2. Ignition Criteria

As discussed above, the mechanism of the pilot ignition has been well understood, however, it is quite unempirical (sometimes even impossible) to use the LFL at the pilot location as a criterion to determine the ignition because both chemical and physical relations involved both solid and gas phases must be solved simultaneously. Hence, for simplicity and practical uses, different indirect ignition criteria have been used to predict the piloted ignition instead of directly using the LFL at the pilot location. Since the piloted ignition involves both condensed phase (solid) and gas phase, we can classify the indirect ignition criterion into two categories: condensed phase related ignition criterion (CPIC), and the gas phase related ignition criterion (GPIC).

The ignition criterion that relates to the ignition commencement to certain properties of the condensed phase is referred to as Condensed Phase-related Ignition Criterion (CPIC). This kind of ignition criteria includes: Critical Surface Temperature (T_{ig}) [12, 13, 22, 23], Critical Average Solid Temperature [24], Critical Mass Flux [8, 25-29], Critical Char Depth [30].

The concept that the solid material should have a unique critical surface temperature at ignition (or ignition temperature) has been accepted since the scientific

study of ignition began [6]. Definition of ignition temperature is the lowest temperature at which the sustained combustion of a material can be initiated under specified conditions [1]. Usually the surface temperature at the following three conditions are considered as the ignition temperature in practice: the flashing point [18], the onset jump of the surface temperature [31], onset of flaming [32]. The measurement of ignition temperature usually can be accomplished by thermal couples or IR-pyrometer.

Because ignition temperature criterion is simple to use, comparably accurate, and is easy to relate to the fire spread, the ignition temperature criterion has been widely used in practice (Chapter 2-7, [5]) and has been proven to be the most useful ignition criterion [3]. It has been used as the ignition criterion in the algorithms of Fire Dynamics Simulator (FDS), a popular and practical tool for solving practical fire problems and studying fundamental fire dynamics and combustion phenomena [33].

Although the concept of ignition temperature has been widely embraced by researchers and engineers, it comes with limitations. For example, the ignition surface temperature is not a constant but changes with external heat flux [4, 11, 31, 32, 34-39]. Experimental observations also showed that a solid material will not undergo piloted ignition if the external heat flux is lower than its critical heat flux for piloted ignition, even if the actual surface temperature is higher than the established surface ignition temperature. In addition, it is hard for ignition temperature criterion to determine the extinguishment of fire.

Martin [24] postulated that ignition occurred only when the entire solid attained an average temperature that exceeded a critical value, referred to as Critical Average Solid Temperature ignition criterion. However, in principle, the Critical

Average Solid Temperature criterion is similar to the Critical Surface Temperature ignition criterion.

Price [40] indicated that ignition was due to exothermic reaction at the surface of the solid and that a surface reaction rate greater than a prescribed critical value would ensure ignition, referred to as critical surface temperature increase rate [10]. The criterion is rarely applied according to the author' knowledge.

The concept of critical Mass Loss Rate (MLR) at ignition was first proposed by Bamford et al. [8] for piloted flaming ignition of wood. Physically, the concept of MLR at ignition can be interpreted as the critical flow of volatiles sufficient to support a nascent flame, and the flame will be extinguished if the flow of volatiles is reduced below it. However, to utilize the concept of MLR to determine ignition, the pyrolysis (and volatiles diffusion) process needs to be predicted first. The prediction of pyrolysis process is usually not as accurate as expected. In addition, the critical mass flux is also not a fixed value, but within a range [26], which is affected by airflow rate [28, 29, 38], radiant heat flux, and oxygen content [27] as summarized by Nelson et al. [25] in 1995. And MLR ignition criterion is hard to relate to the fire spread.

Critical Char Depth was proposed by Sauer [30] to be a criterion to determine the ignition of wood. The material is considered as the char when the mass loss falls to a certain value which is determined by the damage function proposed by Williams [41]. This criterion is hard to applied for the practical application [42].

On the other hand, the gas phase related ignition criterion (GPIC) uses a certain property of the gas phase to determine the ignition. Compared to CPICs, the GPIC is more complicated to apply because both the gas phase and the condensed phase need to be involved in the calculation. The available gas phase related ignition criteria include: Critical Total Reaction Rate in the boundary layer [9], Gas

Temperature Gradient Reversal at the solid-gas interface [43], and Critical Gas Phase Combustion Energy Density [44]. Because they are complicate to use and difficult to relate to fire spread, GPICs are not as popular as CPIC ignition criteria. The following is the brief summary of this ignition criterion.

In 1974 Kashiwagi [9] found that there was a finite range of values for pyrolysis or gas phase reaction activation energy for which ignition would occur (Critical Total Reaction Rate in the boundary layer). Deverall and Lai [43] theoretically showed that for solids that underwent ignition through gas-phase exothermic oxidation reactions, a reversal in the sign of the boundary layer gas temperature gradient at the solid-gas interface was a definite indication of ignition, referred as Gas Temperature Gradient Reversal at the solid-gas interface ignition criterion. Lyon [44] showed that the onset of piloted ignition (flash point) of combustible polymers occurred when a gas phase combustion energy density was 1.9 MJ/m^3 that describes the lower flammability limit of fuel vapor–air mixtures.

All the ignition criteria discussed above are listed in TABLE 1.1. It needs to be mentioned that none of the ignition criteria (neither condense nor gas phase related ignition criterion) can serve as the universal criterion to determine the instant of ignition, because they are deduced from experimental observations, not direct intrinsic material properties to be closely related to the ignition event. Also it may be noted that the all the existing ignition criteria are trying to use one single value of the properties to determine the ignition behavior which includes the complicate physical and chemical processes in both solid and gas phases, under copious conditions. That is one of the major reasons why the current ignition criteria confronting with problem in real applications, taking the most widely used ignition temperature criterion and physically more correct mass loss rate ignition criterion as an example: neither of

criteria can handle the variations of conditions such as moisture, airflow, external heat flux, and oxygen concentration; Critical Surface Temperature ignition criterion also cannot explain the critical heat flux phenomenon, and the MLR at ignition criterion cannot be used to determine the fire spread which is critical in fire science.

TABLE 1.1: The ignition criterion

Ignition Criterion	Onset Condition
Critical Surface Temperature [12, 13, 22, 23]	$T_{surf} \geq T_{ig}$
Critical Average Temperature [24]	$T_{mean} \geq T_{ig,mean}$
Critical Surface Temperature Increase Rate [40]	$\frac{\partial T_{surf}}{\partial t} \geq STIR_{ig}$
Critical Mass Loss Rate [8, 25-29]	$MLR \geq MLR_{ig}$
Critical Char Depth [30]	$\delta_{ch} \geq \delta_{ch,ig}$
Critical Total Reaction Rate in the boundary layer [9]	$\int_0^{\infty} (reaction\ rate) dy \geq R$
Gas Temperature Gradient Reversal at the solid-gas interface [43]	$\left(\frac{\partial T_g}{\partial y}\right)_{y=0} = 0$
Critical Gas Phase Combustion Energy Density [44]	$Q''' \geq 1.9\ MJ/m^3$

Hence, the author sees an urgent need for a new ignition criterion, which is general enough to be applied in various conditions, and meanwhile simple-to-use and easy-to-relate to fire spread.

1.3. Variations in Ignition

It was reported that the ignition could be affected by the properties of solid materials, moisture concentration [45], surface absorptivity and spectral characteristics of the radiant sources, material transparency (Pages 305 - 308[6]), even the external heat flux, specimen thickness [20-22], and airflow rate [46, 47]. In

practical application, all these properties can be varying. Hence for fire safety design purpose, it is essential to understand how the ignition behavior will vary due to variations of material properties, external heating source, and surrounding environmental conditions, and identify the important factors.

Usually the sensitivity and uncertainty analysis is used to evaluate the impact from uncertainty in input(s) on the model output(s). The focus of sensitivity analysis is to evaluate the importance of the inputs. The focus of uncertainty analysis is to evaluate the uncertainty of the outputs brought by the variations of the inputs. Hence, the sensitivity and uncertainty analysis technology is the perfect tool to investigate the variations of the ignition behavior brought from variations in the real fire condition and to identify the important factors [48-50].

Sensitivity analysis (SA) and uncertainty analysis (UA) has been conducted to evaluate the variation of egress time [51], the heat fire detector model [52], thermal response of FRP panel exposed to fire [53] and fire spread model in a Chaparral Landscape [54], but there are few papers investigating uncertainty and sensitivity of ignition behavior. Hence, in this study, the SA and UA study will be conducted to understand the variation of the piloted flaming ignition behavior of combustible solid materials and give a guide to analyze the uncertainty and importance of factors for fire safety purpose.

1.4. Research Objectives and Approaches

From the above discussion, there are three unsolved Tasks in the current literatures: (1) the physical based theoretical analytical solution to predict the temperature profile of the combustible solids with the General Thermal Thickness (GTT); (2) a physical based and simple-to-use ignition criterion which is capable to handle the variations of conditions and meanwhile is easy to relate to fire spread; and

(3) a comprehensive understanding of the variations of the ignition behavior brought from variations of material properties, external heating source, and surrounding environmental conditions.

The objective of this research is to resolve above Tasks. For Task (1), the challenges exist in two stages: (I) how to develop and validate the GTT analytical solution, and (II) how to find a simple and accurate approximation solution for the daily engineer calculation. In Chapter 2 of this dissertation, the Challenge (I) of Task (1) will be resolved; an analytical solution for the solid material with general thermal thickness (GTT) is proposed and validated by the intermediate-scale fire tests. For Challenge (II), a primarily approximation of the closed-form solution is proposed too.

Regarding to Task (2), the challenges also exist in two stages: (I) how to construct the ignition criterion; and (II) how to validate the ignition criterion against every condition. In Chapter 3, a new ignition criterion (HRIT) which is physical base, simple to use and easy to relate to fire spread, will be proposed and validated. Its capability to handle variations of the eternal heat fluxes is proved by PMMA, E-glass/polyester, and Red Oak data. Its potential ability to deal with the surrounding environmental conditions (such as airflow rate, moisture, and etc.) is disused and explained too.

For Task (3), the accurate ignition prediction model and appropriate uncertainty and sensitivity techniques are essential to evaluate the uncertainty and identify the important factors of the ignition behavior. Hence in Chapter 4, the ignition prediction model is chosen as the integrated ignition prediction model, the General Thermal Thickness (GTT) model with the Heat Rate-related Ignition Temperature (HRIT) criterion developed and validated in Chapter 2 and 3 respectively. The local sensitivity analysis technique and the most popular global

sensitivity and uncertainty method, the Monte Carlo simulation using Latin Hypercube Sampling (LHS) method, are employed to conduct sensitivity and uncertainty analysis. The experimental data from Cone Calorimeter test of E-glass/Polyester composite are used as the base to compare with and validate the SA and UA results. Through the study in Chapter 4, the important factors and uncertainty ranges are identified for the piloted ignition of E-glass/Polyester composites. The findings can serve as a guide for fire safety design of FRP materials for infrastructure applications

At the end of this dissertation, the conclusion and future work are summarized in Chapter 5.

CHAPTER 2: GENERAL THERMAL THICKNESS MODEL

2.1. Abstract

This Chapter presents a physical base theoretical analytical solution to predict the temperature profile of the combustible solids with the General Thermal Thickness (GTT) subjected to one-sided heating. The data from the intermediate-scale calorimeter fire tests of E-glass fiber reinforced polyester composite panels at three heat flux levels are used to validate the GTT model. The GTT model is also verified by using results from finite element modeling predictions. The ability of GTT model to predict time-to-ignition (TTI), the surface temperature after ignition and mass loss of combustible solid materials are also presented.

2.2. Introduction

General, there are two design approaches to ensure the fire safety of combustible solid materials: a prescriptive-based design approach and a performance-based design approach. In the prescriptive-based design approach (Chapter 26, [55]), the materials are required to meet the criteria described in the referred standard fire tests (such as ASTM E84 and ASTM E119). In the performance-based design approach [56], the behavior of materials and structures must be evaluated against selected design fire scenarios to meet all performance criteria set by the project stakeholders. Typical fire performance criteria include two categories: (1) life safety (or tenability) criteria that address the survivability of persons exposed to fire and its

products, such as air temperature, radiant heat flux, concentrations of carbonmonoxide (CO), carbon dioxide (CO_2) and oxygen (O_2), and smoke obscuration (or visibility); and (2) non-life safety criteria, such as structural integrity and continuity, fire spread, damage to exposed properties, and damage to the environment. An acceptable design must satisfy all the fire performance criteria against all the anticipated fire scenarios during the trial design evaluation process.

Ignition is an important fire performance parameter of a combustible material. Physically, ignition is the commencement of dramatic release of heat, smoke, CO/CO_2 and dramatic consumption of O_2, thus directly related to life safety fire performance criteria. When evaluating the fire performance of a material, Time-to-Ignition (TTI) is used to compare the ignitability of different materials (e.g., ASTM E1623 and ASTM E1354), the larger the TTI under the same heating condition, the better the material's resistance to ignition. In fire safety egress design, ignition is used as the start point when calculating the Available Safe Egress Time (ASET) to be compared with the Required Safe Egress Time (RSET). Life safety from fire is achieved if RSET is shorter than ASET. The TTI of combustible solids can be obtained by fire testing or model prediction. Fire testing requires special apparatus, trained expertise and other resources and associated costs. It may be required when comparing the ignition resistance of different materials for research and development purpose. However, when performing day-to-day fire safety design calculations, it is imperative that we are able to estimate the TTI of a combustible material through simple calculations by using verified and validated mathematical models.

Thermally-thick (TTK) and thermally-thin (TTN) models are two classical simple theoretical tools using the ignition temperature as the criterion to determine the ignition behavior of combustible solids. The TTK model in [12] assumed that the

back surface temperature of specimens was constant (or the thickness of the specimen was semi-infinite) and the temperature of air was unchanged during the ignition process. An approximation of the TTK model's theoretical solution was derived for sufficiently long TTI in [12]. However, this approximation was not accurate for experimental data not extending to very long TTI. Later the approximation solution for short TTI cases was proposed in [13]. A piecewise-continuous approximation was proposed to cover the whole range of TTI in [14]. Using a statistical approach, a simple approximation solution with a wide range of TTI for theoretical solution of TTK cases was developed in [15].These approximate solutions of TTK model, as simple and useful tools, can be used in analyzing fire tests experimental data and design calculations such as in [16, 17]. In a TTN model, the temperature gradient is assumed to be zero. Thus the solution of a TTN model can be simpler [5].

If the actual thermal conditions were close enough to the TTK or TTN assumptions, the TTI predictions can be acceptable for fire safety design purpose. However, in many practical cases, it is unlikely that the thickness of a specimen barely affects the TTI (as in the TTK model), or the TTI has a linear relation with specimen thickness (as in the TTN model). In these cases, the TTI usually has a nonlinear relation with the material thickness, which can be referred as intermediate thermal thickness. An empirical correlation for wood materials TTI $\propto L^{-n}$ (where L is the specimen thickness) was presented in [20] for intermediate thickness (12-19mm) woods. For intermediate thickness specimen with insulated or constant back surface temperature TTI $\propto \sqrt{L}$ was suggested in [21]. An implicit relation between TTI and material properties for intermediate thermal thickness wood with insulated back surface was given in [22], which was only validated for the wood materials tested. Hence it is hard to extend the empirical correlations to other conditions

So far no useful simple theoretical solution has been verified and validated to predict the exposed surface temperature and TTI for a combustible solid material with general thermal thickness (GTT) without categorizing the thermal thickness of materials. Though by using numerical methods, such as the finite element method (FEM), one can obtain fairly accurate surface temperature such as the work presented in [11], special expertise and effort in numerical implementation are required. There is a lack of validated simple analytical expressions for temperature rise and TTI estimations that can be used for the fire safety design and analysis of combustible solids on a day-to-day basis.

The goal of this Chapter is to present, verify and validate a simplified theoretical model to predict the temperature increase and TTI of combustible solid materials of general thermal thickness subjected to one-sided heating. To achieve this goal, a simplified heat transfer model to predict the surface temperature of GTT solid panels was developed. The TTK and TTN models were included to compare with the GTT model. The theoretical solution of the GTT model was further simplified by the truncation method for practical use. To consider the effect of heating rate on the pyrolysis process, a modified Arrhenius equation was introduced to predict the mass loss. Intermediate-scale Calorimeter (ICAL) fire tests of pultruded E-glass/polyester panels at various heat flux levels were performed to obtain intermediate-scale fire testing data in a controlled condition with well-defined thermal boundary conditions to validate the GTT model. The GTT model was also verified by using predicted results for the same specimens and boundary conditions from FEM models, including TTI, surface temperature and mass loss rate per unit area.

2.3. General Thermal Thickness Model

As described in the Society of Fire Protection Engineer Handbook of Fire Protection Engineering (Chapter 2-11 [5]), the piloted ignition will take place when the lower flammability limit (LFL) of combustible gases from pyrolysis is attained at the location of the pilot. Hence the mass transfer, heat transfer and conservation of moment equations for both solid and gas phases need to be solved simultaneously to obtain the volatile concentration relative to LFL at the pilot location to determine the TTI of solid materials. Numerical methods must be used to solve these equations simultaneously. To obtain an analytical solution of the problem, further simplification of the equations must be made. By using the critical exposed surface temperature as the ignition criteria instead of LFL at the pilot location in the gas phase, the problem and its governing equations can be greatly simplified. With this simplification, the mass transfer in the gas phase can be ignored, and the gas temperature is also out of the interest of this study. We only need to focus on the solid phase. The mass and heat transfer model presented here for solid phase was summarized in [3]. By assuming that pyrolysis gases and moisture are transported instantaneously into gas phase, the balance of mass for a solid panel with general thermal thickness as FIGURE 1.1 is given by Equation 2.1

$$\frac{\partial \rho_s}{\partial t} + \frac{\partial \rho_m}{\partial t} = -\frac{\partial \dot{m}''}{\partial x} \qquad \text{Equation 2.1}$$

The term on the right-hand-side of Equation 2.1 corresponds to the total mass loss. And the terms on left-hand-side relate to mass loss caused by pyrolysis and water evaporation respectively.

Equation 2.2 is the one-dimensional balance of energy

$$\rho_s c_s \frac{\partial T_s}{\partial t} = \frac{\partial}{\partial x}\left(\frac{\partial \lambda_s T_s}{\partial x}\right) + \dot{Q}(x,t) \quad \text{Equation 2.2}$$

The term $\dot{Q}(x,t)$ is the effective heat source or sink within the solid and can be expressed as Equation 2.3

$$\dot{Q}(x,t) = \frac{\partial \dot{q}_r''}{\partial x} - \dot{m}'' \frac{\partial H_g}{\partial x} + (Q_s - H_s + H_g)\frac{\partial \rho_s}{\partial t} + (Q_m - H_m + H_g)\frac{\partial \rho_m}{\partial t} \quad \text{Equation 2.3}$$

The first term on the right-hand-side of Equation 2.3 accounts for the in-depth absorption of radiation energy from external heating source. This term is very small for opaque materials, such as FRP materials in this study, and can be set to zero (Pages 305 - 308, [6]). The second term accounts for heat loss caused by mass transported into the gas phase. The third and fourth terms correspond to the energy required for thermal decomposition and moisture desorption, respectively. Q_s is the heat of solid decomposition per unit mass and Q_m is the heat of moisture desorption per unit mass. The enthalpy is defined as $H_j = \int_{T_0}^{T} c_j dT$, with j represents for *s* and *m*.

The boundary condition at the exposed surface (FIGURE 1.1) is shown in Equation 2.4

$$-\lambda \frac{\partial T_s}{\partial x} = -h\left(T_s - T_g\right) - \varepsilon\sigma\left(T_s^4 - T_g^4\right) + \dot{q}_e'', for\ x = 0, t > 0 \quad \text{Equation 2.4}$$

Where $\dot{q}_e''$ is the constant external heat flux, h is the heat convection coefficient and ε is the emissivity.

The thermal condition at the unexposed surface is given as

$$-\lambda_s \frac{\partial T_s}{\partial x} = h\left(T_s - T_g\right) + \varepsilon\sigma\left(T_s^4 - T_g^4\right), for\ x = L, t > 0 \quad \text{Equation 2.5}$$

where T_g is the air temperature at infinity. If thermal insulation is applied at the back surface, $\boldsymbol{\varepsilon}$ is set to be zero and *h* can be obtained from the thermal properties of the insulation.

The initial condition can be written as

$$T_s(x, 0) = T_0, \text{for } x \geq 0, t = 0 \qquad \text{Equation 2.6}$$

Here our focus is the theoretical solution of temperature field. To obtain an analytical solution for above equations, we need to decouple the partial differential equations and linearize the boundary conditions. The following assumptions are made to achieve this: (1) The samples are dry and the effect of pyrolysis on temperature increase is negligible, (2) The surrounding environment temperature remains constant (T_0), and (3) The heat convection and re-radiated terms are combined into an effective convection term. Based on Assumption (1), the effects from moisture and pyrolysis on temperature increase can be neglected, and $\dot{Q}(x, t)$ is equal to zero. It was shown that the TTI of wood will increase substantially with increased moisture content [45]. Hence this model is limited to dry materials such as FRP composites. So the balance of energy Equation 2.2 can be simplified as

$$\rho_s c_s \frac{\partial T_s}{\partial t} = \frac{\partial}{\partial x}\left(\lambda_s \frac{\partial T_s}{\partial x}\right) \qquad \text{Equation 2.7}$$

Now the balance of energy Equation 2.7 is decoupled from the balance of mass Equation 2.1.

From Assumption (2) and (3), the boundary conditions Equation 2.4 and Equation 2.5 can be written as:

$$-\lambda \frac{\partial T_s}{\partial x} = -h_{eff}(T_s - T_0) + \dot{q}''_e, \text{for } x = 0, t > 0 \qquad \text{Equation 2.8}$$

$$-\lambda\frac{\partial T_s}{\partial x} = h_{eff}(T_s - T_0), \text{for } x = L, t > 0 \qquad \text{Equation 2.9}$$

The effective convection coefficient h_{eff} is assumed a constant during the analytical process, though based on Assumption (3) h_{eff} is a function of surface temperature. The effect of this constant h_{eff} assumption will be discussed later in this paper.

Then the heat transfer model can be simplified as governing Equation 2.7 with boundary conditions Equation 2.8 and Equation 2.9, and initial condition Equation 2.6. If the back surface is totally insulated, h_{eff} should be set as zero as Equation 2.10

$$-\lambda\frac{\partial T_s}{\partial x} = 0, for\ x = L, t > 0 \qquad \text{Equation 2.10}$$

So we can obtain the back surface insulated heat transfer model with Equation 2.6, Equation 2.7, Equation 2.8 and Equation 2.10. Equation 2.11 and Equation 2.12 show the solutions for un-insulated and insulated back surface conditions respectively. The Equation 2.11 can be obtained from Appendix A, in which the analytical solution of a slab under un-insulated conditions subjected to time dependent external heat flux $\dot{q}''(t)$ is given, by assuming constant external heat flux (set $F_n(s) = 0$). And Equation 2.12 can be obtained by following the similar procedures described in Appendix.

$$T_s(x,t) = T_0 + \dot{q}_e''\left[\frac{\lambda + h_{eff}(L - x)}{h_{eff}(2\lambda + h_{eff}L)}\right]$$

$$+ \sum_{n=1}^{N} \theta_n \left[\cos(\mu_n x) + \frac{h_{eff}}{\lambda\mu_n}\sin(\mu_n x)\right] e^{-\alpha\mu_n^2 t}, N \to \infty, t \geq 0 \qquad \text{Equation 2.11}$$

With $\theta_n = -\frac{2\dot{q}_e''\lambda}{[\mu_n^2\lambda^2 + h_{eff}^2]L + 2h_{eff}\lambda}, \tan\mu_n L = \frac{2\lambda h_{eff}\mu_n}{\lambda^2\mu_n^2 - h_{eff}^2}$

$$T_s(x,t) = T_0 + \frac{\dot{q}''_e}{h_{eff}} + \sum_{n=1}^{N} \theta_n \left[\cos(\mu_n x) + \frac{h_{eff}}{\lambda \mu_n}\sin(\mu_n x)\right] e^{-\alpha \mu_n^2 t},$$

$$N \to \infty, t \geq 0, \qquad \text{Equation 2.12}$$

With $\theta_n = -\frac{2\dot{q}''_e \lambda}{[\mu_n^2\lambda^2 + h_{eff}^2]L + h_{eff}\lambda}$, $\tan\mu_n L = \frac{h_{eff}}{\lambda \mu_n}$

Before flaming, the external heat flux is considered as constant, and the temperature field can be predicted by Equation 2.11 and Equation 2.12. After flaming, the flaming effect on temperature filed can be accounted by adding time-dependent effective heat flux $\dot{q}''_F(t)$ to initial external heat flux $\dot{q}''_e$ as net external heat flux:

$$\dot{q}''_{net}(t) = \begin{cases} \dot{q}''_e & (t < t_{ig}) \\ \dot{q}''_e + \dot{q}''_F(t) & (t \geq t_{ig}) \end{cases} \qquad \text{Equation 2.13}$$

Replacing $\dot{q}''_e$ in the exposed boundary condition Equation 2.8 with net external heat flux $\dot{q}''_{net}(t)$, the new boundary condition Equation 2.8 with flame effects is obtained.

The solution with flame effects for un-insulated condition is given as Equation 2.14 and the solving procedure is described in Appendix A. Equation 2.15 is the solution for insulated condition, which can be obtained by using the same procedure described in Appendix. To be clear, the thermal properties of the material were assumed to be constant prior to flaming in Appendix A. Equation 2.14 and Equation 2.15 will not be accurate for materials whose thermal properties change significantly after ignition.

$$T_s(x,t) = T_0 + (\dot{q}''_e + \dot{q}''_F)\left[\frac{\lambda + h_{eff}(L-x)}{h_{eff}(2\lambda + h_{eff}L)}\right] + \sum_{n=1}^{N}[\theta_n e^{-\alpha\mu_n^2 t} +$$

$$\int_0^t e^{\alpha\mu_n^2(s-t)} F_n(s)ds]\left[\cos(\mu_n x) + \frac{h_{eff}}{\lambda\mu_n}\sin(\mu_n x)\right], N \to \infty, t \geq 0 \qquad \text{Equation 2.14}$$

With $\theta_n = -\frac{2\dot{q}''_e\lambda}{[\mu_n^2\lambda^2 + h_{eff}^2]L + 2h_{eff}\lambda}$, $F_n(s) = -\frac{2\lambda}{[\mu_n^2\lambda^2 + h_{eff}^2]L + 2h_{eff}\lambda}\frac{d\dot{q}''_F}{ds}$,

$$\tan\mu_n L = \frac{2\lambda h_{eff}\mu_n}{\lambda^2\mu_n^2 - h_{eff}^2}$$

$$T(x,t) = T_0 + \frac{\dot{q}_e'' + \dot{q}_F''}{h_{eff}} + \sum_{n=1}^{N}\left[\theta_n e^{-\alpha\mu_n^2 t} + \int_0^t e^{\alpha\mu_n^2(s-t)}F_n(s)ds\right]\left[\cos(\mu_n x) + \frac{h_{eff}}{\lambda\mu_n}\sin(\mu_n x)\right], \quad N \to \infty \geq 0 \qquad \text{Equation 2.15}$$

With $\theta_n = -\frac{2\dot{q}_e''\lambda}{[\mu_n^2\lambda^2 + h_{eff}^2]L + h_{eff}\lambda}$, $F_n(s) = -\frac{2\lambda}{[\mu_n^2\lambda^2 + h_{eff}^2]L + h_{eff}\lambda}\frac{d\dot{q}_F''}{ds}$,

$$\tan\mu L = \frac{h_{eff}}{\lambda\mu}$$

2.4. Thermally Thick (TTK) Model and Thermally Thin (TTN) Model

If we assume that the thickness of the specimen is semi-infinite, the GTT model before ignition can be reduced to the TTK model as,

$$\rho_s c_s \frac{\partial T_s}{\partial t} = \frac{\partial}{\partial x}\left(\lambda_s \frac{\partial T_s}{\partial x}\right) \qquad \text{Equation 2.16}$$

$$T_s(x,0) = T_0, \text{for } x \geq 0, t = 0 \qquad \text{Equation 2.17}$$

$$-\lambda\frac{\partial T_s}{\partial x} = -h_{eff}(T_s - T_0) + \dot{q}_e'', \text{for } x = 0, t > 0 \qquad \text{Equation 2.18}$$

$$T_s = T_0, \text{for } x = \infty, t > 0 \qquad \text{Equation 2.19}$$

And its solution [57] is

$$T_s(x,t) = T_0 + \frac{\dot{q}_e''}{h_{eff}}\text{erfc}\left(\frac{x}{2\sqrt{\alpha t}}\right) - \frac{\dot{q}_e''}{h_{eff}}e^{\frac{h_{eff}x}{\lambda} + \frac{\alpha h_{eff}^2 t}{\lambda^2}}\text{erfc}\left(\frac{x}{2\sqrt{\alpha t}} + \frac{h_{eff}\sqrt{\alpha t}}{\lambda}\right) \qquad \text{Equation 2.20}$$

If we ignore the temperature gradient through the thickness of a specimen, we can obtain the TTN model with un-insulated back surface boundary condition as

$$\rho_s c_s L \frac{\partial T_s}{\partial t} = -2h_{eff}(T_s - T_0) + \dot{q}''_e \quad \text{Equation 2.21}$$

$$T_s = T_0, t = 0 \quad \text{Equation 2.22}$$

And its solution is

$$T_s = T_0 + \frac{\dot{q}''_e}{2h_{eff}}\left[1 - exp\left(-\frac{2h_{eff}t}{L\rho c_s}\right)\right] \quad \text{Equation 2.23}$$

2.5. Intermediate Scale Fire Tests

To provide experimental data to validate the above models, fire experiments using an Intermediate-scale Calorimeter (ICAL) were performed [11, 58]. The ICAL was developed to measure the fire properties of products in a manner representative of their end use conditions [59]. The apparatus and the test procedures are described in details in ASTM E1623 [60]. The following properties of a material can be measured by the ICAL: time to ignition, mass loss and mass loss rate, heat release rate, effective heat of combustion, smoke and gas production, and surface temperature. The ICAL consists of a radiant panel assembly in the vertical orientation, a sample holder in the vertical orientation (and in parallel to the radiant panel), a weighing platform, a radiant panel constant irradiance control system, an infrared pyrometer, and an exhaust collection system. The radiant panel together with the constant irradiance control system is designed to ensure a uniform heat flux on the 1000mm by 1000mm testing surface area of the sample holder. By adjusting the distance between the sample holder and the radiant panel, different heat flux levels can be achieved for the exposed surface of the testing specimen. For this experimental setup, the thermal boundary conditions of the specimen surfaces are well defined as: The exposed side is subjected to a constant heat flux, and the unexposed surface is subjected to ambient laboratory condition.

The specimens for the ICAL tests were pultruded E-glass/polyester panels. The specimen size was 1000mmx 1000mm x 6.35 mm. The fiber faction was 28.7% by volume and 40% by weight. The material properties are shown in TABLE 2.1. Prior to tests, the specimens were maintained in a conditioned room at 23 ± 3°C and 50 ± 5% relative humidity for several months. The ICAL tests were conducted at three heat flux levels: 25, 35, and 45kW/m^2(the maximum heat flux from the ICAL is 50kW/m^2). For each heat flux level, at least two specimens were tested. Basic reaction-to-fire properties, such as TTI, surface temperatures, mass loss, and heat release, were recorded during each test. If consistent reaction-to-fire properties are measured, then the average properties from the two tests will be used. If no-consistent reaction-to-fire properties are obtained, a third or fourth test will be performed till consistent results are obtained, and the reported data are taken as the average from the consistent tests. During ICAL tests, two specimens generated very consistent results at each heat flux level. Thus a total of six ICAL tests were performed. The mass loss was measured by a Sartorius IS 150 weighing platform, which has a 0-150 kg weight range with a measuring accuracy of 1g.

To measure surface temperatures on the exposed surface and the back surface, special thermocouples (TCs) of 0.127 mm diameter (type K with error limit of 2.2 °C or 0.75% of the temperature in °C) were used. For each surface, four locations were used to measure surface temperature history. The average of the measurements from the four locations is taken as the surface temperature for a specimen. The locations and layout of the TCs for the exposed and the back surfaces are shown in FIGURE 2.1. (a).

TABLE 2.1: Material properties of pultruded E-glass/polyester panels

Basic Properties	
Virgin Density [kg/m³]	1888
Char Density [kg/m³]	1133
Dimension [mm×mm×mm]	1000×1000×6.35
Thermal Properties	
Specific Heat [J/kg.K]	2068.8
Heat Conductivity [w/m K]	0.2
Heat Convection Coefficient [w/m² k]	10
Exposed Surface Temperature at Flashing [°C]	356±13°C
Exposed Surface Temperature at Sustained Flaming[°C]	424 ± 5 °C
Critical / Minimum Heat Flux [kW/m²],	9.73 / 23.2
Emissivity $\boldsymbol{\varepsilon}$[--]	0.99
Decomposition Properties	
Rate Constant [1/s]	34377066771
Reaction Order [-]	4.4463
Activation energy [J/kg.mol]	149026
Critical Temperature rate $\dot{T}_{Critical}$ [K/s]	5
Shift Coefficient $\boldsymbol{\epsilon}$ [--]	0.0000225
Effective Heat Convection [w/m² k] at External Heat Flux [kW/m²], 25, 35, and 45	
General Thermal Thickness (GTT)Model	32.10 / 38.17 / 44.03
Thermally-thick (TTK) Model	38.88 / 46.39 / 53.36
Thermally-thin (TTN) Model	38.88 / 46.39 / 53.36

It is critical that the TCs measure the surface temperature during the whole process of fire testing. For the exposed surface, the surface will recede after the resin is burned during fire test. To ensure good surface contact between the TC junction and specimen surface, a special TC mounting method was used. For each TC, two holes of 17.5 mm apart and 0.7 mm in diameter were drilled through the specimen along the thickness direction. TC leads were then pulled through the holes such that the TC junction on the exposed surface was positioned in the middle of the holes. To keep a good contact between the TC junction and the exposed surface during testing, approximately 5g of weight was hung on the TC lead wires as shown in FIGURE 2.1. (b). For the back surface, TC wires were attached to the surface using high temperature epoxy to ensure that the TC junctions always had good contact with the surface all the time during fire test.

To provide validation data for temperatures measured by TCs on the exposed surface, a calibrated infrared pyrometer (Heitronics Model KT19.81 with a 0-1000°C temperature range and wavelength band of 8-10 mm) was positioned behind a slot in the ICAL radiant panel and was aimed just above the TC junction of TC #2. The spectral emissivity setting of the pyrometer was maintained at 1.0 during all ICAL tests. The infrared pyrometer was calibrated at the factory with a blackbody furnace. Its limit of error is 0.5°C. The pyrometer was used for all the six tests. Results showed that temperatures measured by the infrared pyrometer were quite consistent with the TC temperature measurement at the same location. Thus this special TC mounting method for surface temperature measurement was validated. The results from all ICAL fire tests will be presented together with modeling results in the “Results and Discussion” section. All ICAL data presented at a certain point are an average value together with its standard deviation.

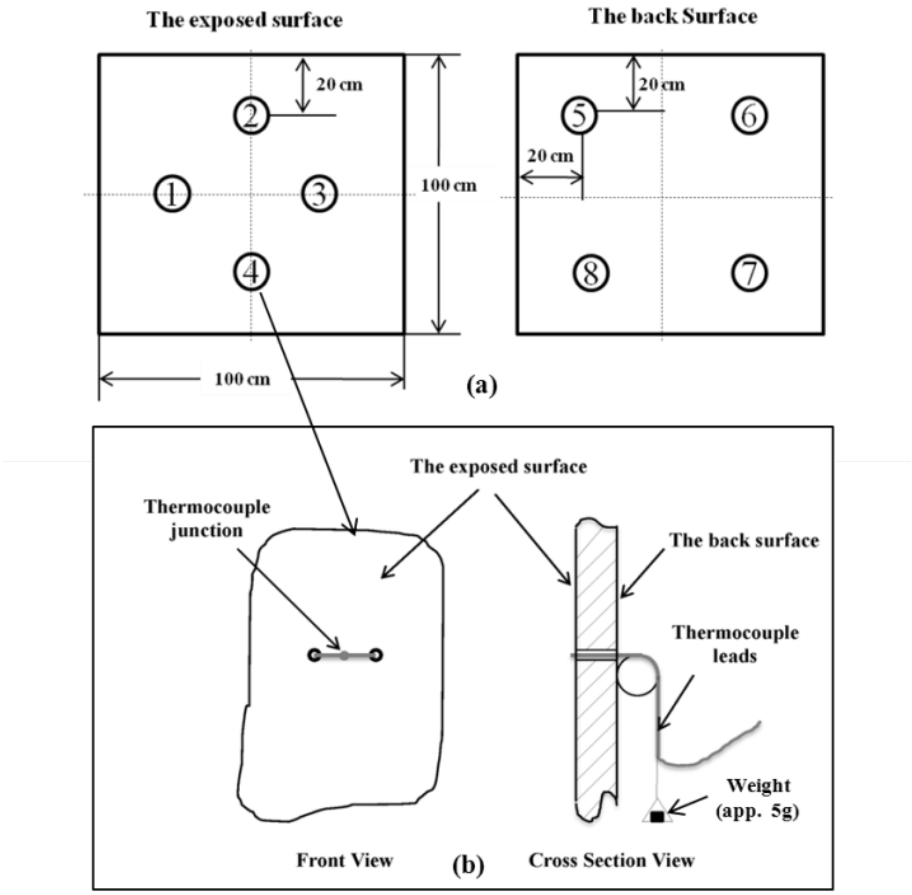

FIGURE 2.1: Layout and instrumentation of thermocouple

2.6.Procedures to Calculate Time-to-Ignition

Since the ICAL data are used to validate the GTT model, the procedures for applying the GTT model to a specimen subjected to one-sided constant heat flux heating with an un-insulated back surface (the thermal boundary conditions of an ICAL specimen) is described here. The same procedures can be directly applied for insulated back surface condition. Procedures for using the TTK and TTN models are also briefly discussed for comparison purpose.

By setting $x=0$ in Equation 2.11, we have the exposed surface temperature of the GTT model as shown in Equation 2.24

$$T_{surf}(t) = T_0 + \dot{q}''_e \left[\frac{\lambda + h_{eff}L}{h_{eff}(2\lambda + h_{eff}L)}\right] + \sum_{n=1}^{N} \theta_n e^{-\alpha\mu_n^2 t}, N \to \infty, t \geq 0 \quad \text{Equation 2.24}$$

With $\theta_n = -\frac{2\dot{q}''_e\lambda}{[\mu_n^2\lambda^2 + h_{eff}^2]L + 2h_{eff}\lambda}$, $\tan\mu_n L = \frac{2\lambda h_{eff}\mu_n}{\lambda^2\mu_n^2 - h_{eff}^2}$

The exposed surface temperature of the TTK model can be obtained in the similar way by setting *x=0* in Equation 2.20.

$$T_{surf} = T_0 + \frac{\dot{q}''_e}{h_{eff}}\left[1 - e^{\frac{\alpha h_{eff}^2 t}{\lambda^2}} \operatorname{erfc}\left(\frac{h_{eff}\sqrt{\alpha t}}{\lambda}\right)\right] \quad \text{Equation 2.25}$$

In this paper, we will use Equation 2.26, which was the approximation of Equation 2.25 and proposed and validated in [15], to calculate the surface temperature for the TTK model.

$$T_{surf} = T_0 + \frac{\dot{q}''_e}{h_{eff}} \frac{1}{1 + 0.73\left(\frac{h_{eff}^2 t}{\lambda\rho C}\right)^{-0.55}} \quad \text{Equation 2.26}$$

It may be noticed that with constant ignition temperature Equation 2.26 implies that if $\dot{q}''_e$ is put on the x-axis and $(t_{ig})^{-0.55}$ on the y-axis, the experimental data will fall in a straight line.

The exposed surface temperature of the TTN model is given by Equation 2.23.

The effective convection coefficient h_{eff} needs to be obtained for Equation 2.23 Equation 2.24, and Equation 2.26 to predict TTI. Usually h_{eff} is obtained as (Pages 260 - 263,[6]),

$$h_{eff} = \frac{\dot{q}''_{cr} \text{ (or } \dot{q}''_{min})}{T_{ig} - T_0} \quad \text{Equation 2.27}$$

where the critical heat flux, $\dot{q}''_{cr}$, is the theoretical lowest external heat flux at which the material will ignite at $t_{ig}=inf$. It can be obtained as the x-axis intercept of

the $(t_{ig})^{-0.55}$ vs $\dot{q}''_e$ curve based on Equation 2.26. Using the data in TABLE 2.2, the critical heat flux for this material was determined as 9.73 kW/m². And the minimum heat flux, $\dot{q}''_{min}$, is the average of the lowest flux at which ignition occurs and the highest flux at which no ignition occurs for long exposure times [5]. In the ICAL tests, the E-glass/polyester samples did not ignite under 25 kW/m² external heat flux, but it was reported in [39] that the ignition occurred at 25 kW/m² in Cone Calorimeter Tests. Hence 25 kW/m² was determined as the $\dot{q}''_{min}$ for the E-glass/polyester composite in this paper. Then according to Equation 2.27 with T_{ig}=356 °C given in TABLE 2.1, the effective heat convection coefficients are 29.40 and 75.53 w/m² k based on $\dot{q}''_{cr}$ and $\dot{q}''_{min}$ respectively.

TABLE 2.2: Comparison of TTI from ICAL experiment and predictions

Heat Flux [kW/m²]	Time-to-ignition (sec)					
	ICAL (Average)	FE-FR*	FE-IR**	TTN	TTK	GTT
35	110	88	97	308	131	112
45	60	54	53	232	70	62

*: Finite-rate FE model; **: Infinite-rate FE model.

We here propose a new average method to obtain h_{eff}. From Assumption (3) or definition of h_{eff} we can get Equation 2.28

$$h_{eff} = h + \varepsilon\sigma[T_{surf}^2(t) + T_0^2][T_{surf}(t) + T_0] \qquad \text{Equation 2.28}$$

We use the average value from initial temperature T_0 to surface temperature at infinity $T_{surf}(\infty)$ to approximate the effective convective coefficient as shown in Equation 2.29

$$h_{eff} = \frac{1}{T_{surf}(\infty) - T_0}\int_{T_0}^{T_{surf}(\infty)} [h + \varepsilon\sigma(T^2 + T_0^2)(T + T_0)]dT$$

$$= h + \frac{1}{4}\varepsilon\sigma T_{surf}^3(\infty) + \frac{7}{12}\varepsilon\sigma T_{surf}^2 T_0 \qquad \text{Equation 2.29}$$

$$+ \frac{13}{12}\varepsilon\sigma T_{surf}(\infty) T_0^2 + \frac{25}{12}\varepsilon\sigma T_0^3$$

Where the exposed surface temperature $T_{surf}(\infty)$ for the GTT model is given in Equation 2.30, and TTK and TTN models are given in Equation 2.31, obtained from Equation 2.24, Equation 2.23 and Equation 2.25 by setting $t \to \infty$

$$T_{surf}(\infty) = T_0 + \dot{q}_e'' \left[\frac{\lambda + h_{eff} L}{h_{eff}(2\lambda + h_{eff} L)}\right] \qquad \text{Equation 2.30}$$

$$T_{surf}(\infty) = T_0 + \frac{\dot{q}_e''}{h_{eff}} \qquad \text{Equation 2.31}$$

Substitute Equation 2.30 or Equation 2.31 into Equation 2.29, then h_{eff} can be obtained by solving Equation 2.29.

FIGURE 2.2 shows the comparison of effective heat convection coefficient at 25 kW/m² external heat flux with the material properties shown in TABLE 2.1. The experimental value of h_{eff} in FIGURE 2.2 is obtained according to Equation 2.28 using the exposed surface temperature from ICAL tests. It can be seen from FIGURE 2.2 that the minimum heat flux method releases an unrealistically high approximation and the average method and critical heat flux method gave an acceptable approximation. Since h_{eff} is a function of surface temperature, it is not possible to use a constant value to approximate h_{eff} accurately under any circumstance. In this study, the average method will be used to determine h_{eff} based on the following two considerations: (1) The h_{eff} obtained by the average method gave a better surface temperature prediction compared with the critical and the minimum heat flux methods as shown in FIGURE 2.3. (2) The average method requires no extra experiments

compared with the critical and the minimum heat flux methods in which the critical and the minimum heat flux needs to be obtained from tests.

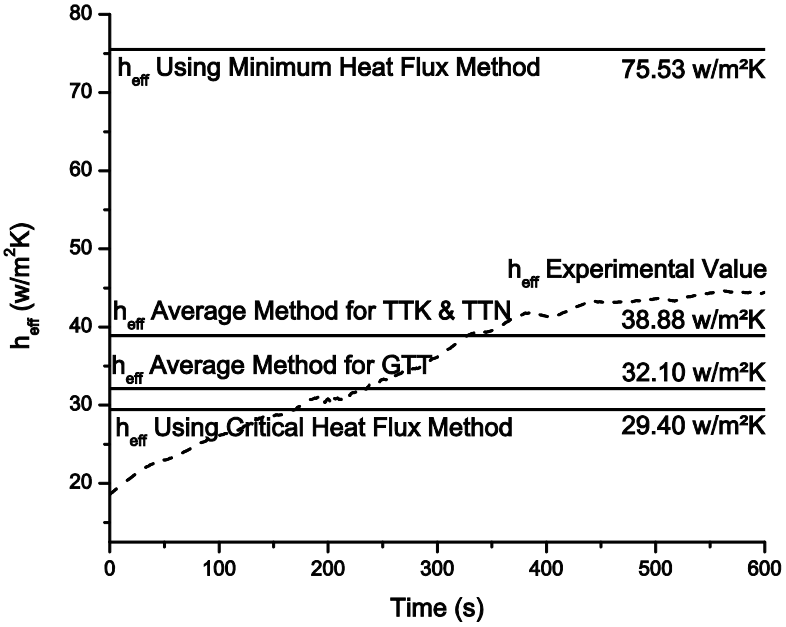

FIGURE 2.2: Comparisons of h_{eff} approximations

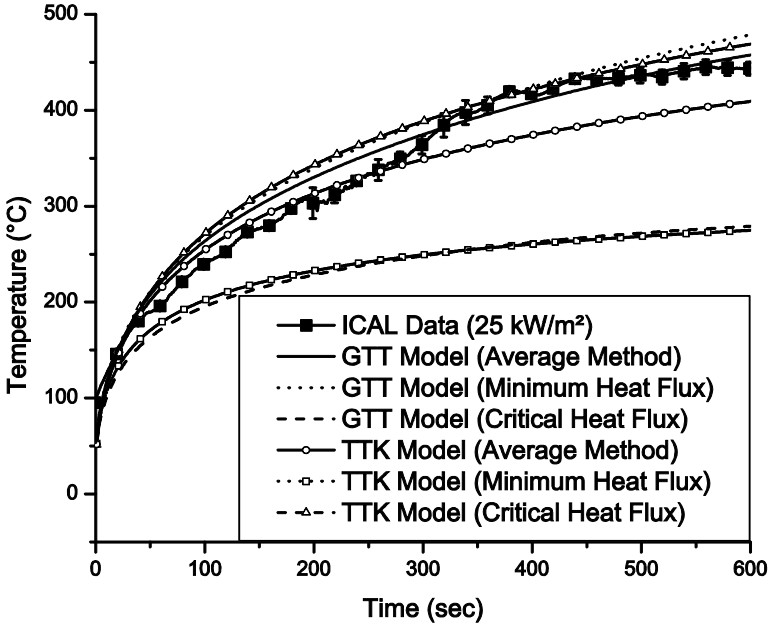

FIGURE 2.3: Surface temperature predictions using different h_{eff} approximation

Now Equation 2.24 is mathematically complete solution with no unknown parameters, but it is still not practical for day-to-day design calculations. The obstacle is the infinite series in the solutions. Since we know the surface temperature of a material cannot be infinite, the infinite series in Equation 2.24 must converge to a finite value,

$$\sum_{n=1}^{N} \theta_n e^{-\alpha \mu_n^2 t} = M_{ICAL}, N \to \infty, t \geq 0 \qquad \text{Equation 2.32}$$

With $\theta_n = -\frac{2\dot{q}_e'' \lambda}{[\mu_n^2 \lambda^2 + h_{eff}^2]L + 2h_{eff}\lambda}, \tan \mu_n L = \frac{2\lambda h_{eff} \mu_n}{\lambda^2 \mu_n^2 - h_{eff}^2}$

The larger the N value, the more accurate Equation 2.32 will be. But in practice, a smaller N value is preferred, because it will save the cost of calculation. FIGURE 2.4 shows the exposed surface temperature predictions using Equation 2.24 corresponding to different N values using material properties shown in TABLE 2.1. It shows that when N is greater than 5, the prediction of surface temperature converges to the same line. So in this study, N is set to 5. In general, the N value should be chosen based on specific conditions. For composite materials within practical thickness range, N=5 to 10 is suggested.

Now set the exposed surface temperature equal to the critical surface temperature at ignition

$$T_{surf}(t_{ig}) = T_{ig} \qquad \text{Equation 2.33}$$

Then TTI (t_{ig}) can be solved from Equation 2.33, or by using plot chart.

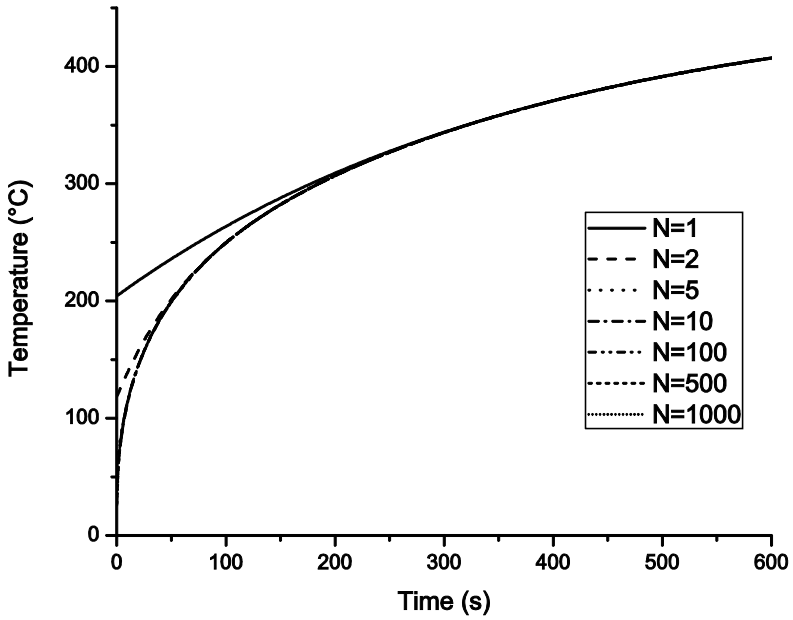

FIGURE 2.4: Convergence property of exposed surface temperature prediction of the GTT model

2.7. Effect of Combustion Flame on Temperature and Mass Loss

2.7.1. Effect of Combustion Flame on Temperature

The solution with combustion flame effect is given in Equation 2.14, in which the effective flame heat flux $\dot{q}''_F$ and the effective heat convection h_{eff} are unknown.

In [61] the flame effect under different external heating flux for the same FRP composite material in this paper was studied. It was reported that the maximum flame effect was achieved at the very beginning of flaming ignition, and then decreased almost linearly and became very small (approaching to zero) at the end (FIGURE 4 of [61]). According to this observation, the effective flame heat flux arriving at the specimen is approximated as a linear function of the average flame flux as Equation 2.34

$$\dot{q}''_F = \begin{cases} 2\dot{q}''_{Faverage}\left(1 - \frac{t}{t_{burn}}\right), & t_{ig} < t < t_{burn}, \\ 0, & \text{otherwise} \end{cases} \qquad \text{Equation 2.34}$$

Where $\dot{q}''_{Faverage}$ is the average of effective flame flux, $\dot{q}''_F$ is the effective flame flux function of time, t_{burn} is burning time starting from flaming ending with extinguishment.

Then in order to estimate h_{eff}, the exposed surface temperature at $t \to \infty$ is obtained as Equation 2.35

$$T_{surf}(\infty) = T_0 + [\dot{q}''_e + \dot{q}''_F(\infty)]\left[\frac{1}{h_{eff}} - \frac{\lambda}{h_{eff}(2\lambda + h_{eff}L)}\right] \qquad \text{Equation 2.35}$$

From Equation 2.34, we can obtain $\dot{q}''_F(\infty) = 0$. Since our primary concern is the temperature of the composite prior to ignition and during flaming, not after flame extinction, we set

$$T_{surf}(\infty) = T_0 + \left[\dot{q}''_e + \dot{q}''_{Faverage}\right]\left[\frac{1}{h_{eff}} - \frac{\lambda}{h_{eff}(2\lambda + h_{eff}L)}\right] \qquad \text{Equation 2.36}$$

The effective heat convection coefficient can be determined by substituting Equation 2.36 into Equation 2.29. N in the equation can be set to 5 as discussed in the previous section.

2.7.2. Effect of Combustion Flame on Mass Loss

The modified Arrhenius equation [11] shown as Equation 2.37 is used to describe the relationship between pyrolysis and temperature of composite material.

$$\frac{\partial \rho_s}{\partial t} = -A(\rho_o - \rho_{ch})\left(\frac{\rho_s - \rho_{ch}}{\rho_o - \rho_{ch}}\right)^n \exp\left[-\frac{E}{R(T - T_{sh})}\right] \qquad \text{Equation 2.37}$$

Where ρ_s, $\rho_o$and $\rho_{ch}$are the density at time t, the original density and char density of the composite respectively. The Arrhenius parameters, rate constant *A*, reaction order *n* and activation energy *E* can be determined by using Thermogravimetric Analysis (TGA) or Differential Scanning Calorimetry (DSC). $T_{sh}$is the temperature shift function which is used to model the effect of changing

heating rates. T_{sh} was obtained using an experimental method in [11]. Here a theoretical expression of the temperature shift function is proposed as Equation 2.38,

$$T_{sh} = \begin{cases} = 0 & , \frac{\partial T}{\partial t} < \dot{T}_{Cr} \\ = \epsilon \dot{q}'' \mathrm{Max}\left\{\frac{\partial T}{\partial t}\right\}, & \frac{\partial T}{\partial t} \geq \dot{T}_{Cr} \end{cases} \quad \text{Equation 2.38}$$

where $\dot{T}_{Cr}$ and ϵ are the critical temperature changing rate and a shift coefficient, they are constants for a specific material.

Since the solid is assumed to be dry, then the balance of mass Equation 2.1 becomes

$$\frac{\partial \rho_s}{\partial t} = -\frac{\partial \dot{m}''}{\partial x} \quad \text{Equation 2.39}$$

Integrating Equation 2.39over the thickness direction, the mass loss per unit area is obtained as,

$$\dot{m}'' = \int_0^L \frac{\partial \dot{m}''}{\partial x} dx = \int_0^L -(\frac{\partial \rho_s}{\partial t}) dx \quad \text{Equation 2.40}$$

2.8. Results and Discussion

2.8.1. Temperature and Time-to-Ignition

During experiments, there was no flashing or flaming observed at 25kW/m² level during the 30 minutes fire test. Both flashing (at T_s=356 ± 13 °C) and sustained flame (at T_s=424 ± 5 °C) were observed at 35kW/m² and 45kW/m² levels. In fire testing, ignition temperature is defined as the lowest surface temperature at which sustained flaming of a material is achieved under specified test conditions [60]. In this study the surface temperature at flashing is used as the ignition temperature based on the following two considerations. First, theoretically, ignition starts at the flashing point when the LFL of combustible gases is initially attained at the pilot location. Second, using the surface temperature at flashing as ignition temperature in practice

leads to a more conservative and safer design compared with using the surface temperature at sustained flaming.

FIGURE 2.5, FIGURE 2.6, and FIGURE 2.7 show the comparisons of the exposed surface temperature from ICAL experiments and predictions from the FEM model [11], the GTT model and the TTN and TTK models at heat flux levels of 25, 35 and 45kW/m². The error bars in the ICAL data represent standard deviation.

Comparisons at 25kW/m² flux level are shown in FIGURE 2.5. Generally, finite-rate and infinite-rate predictions from FEM models showed higher exposed surface temperature predictions than GTT, TTK and TTN models. The GTT model showed lower predictions of exposed surface temperature in the beginning and then higher predictions after 280s compared with FE finite-rate model. This was mainly caused by the fact that the effective heat convection coefficient was assumed as an average value between the initial temperature and the temperature at infinity in the model.

The TTK model predicted lower exposed surface temperature compared with the FEM models and the GTT model. This was mainly caused by the infinite thickness assumption. However, overall it has good agreement with experimental data before 256s.

The TTN model predictions were much off compared to the experimental data and FEM predictions. This is because the specimens tested cannot be considered as thermally thin samples. Among all the models, the GTT model showed the best agreement with experimental data for the exposed surface temperature. However, this does not necessarily mean that the GTT model is more correct than the other models. The FEM models performed well in predicting the back surface temperatures. For the GTT model, the back surface temperature predictions were low.

FIGURE 2.6 and FIGURE 2.7 show comparisons of temperatures for specimens at 35kW/m² and 45kW/m² heat flux levels. Sustained flaming and ignition were observed at both levels. One can see that predictions from models before ignition showed similar results as in FIGURE 2.5 (no ignition). Hence, the FEM models gave shorter TTI predictions, and the TTK model gave longer predictions. The TTN model predicted unrealistically long TTI as shown in TABLE 2.2. The GTT model showed best overall agreement with experimental data.

Since the FEM, TTK and TTN models did not take flame effect into account, the exposed surface temperature after ignition was not well captured by these models. However, the FEM models provided good predictions on the back surface temperature. The TTK model prediction was fairly lower than experimental results after ignition. The TTN model predictions were not in agreement with experimental data at all.

The average flame fluxes arriving at the composite were determined as 4.5 kw/m² and 3.5 kw/m² at heat flux levels of 35 kw/m² and 45 kw/m² respectively [61]. The effective flame heat flux was approximated by Equation 2.34.

Overall, the GTT model with flame effect showed acceptable higher predictions of both the exposed and back surface temperatures. However, the temperature transition between the flashing point and flame point is not well presented in the GTT model. That is because the effective flame heat flux used in the model was simple, i.e., a linear function of time. More sophisticate model for effective flame heat flux is needed for a better prediction.

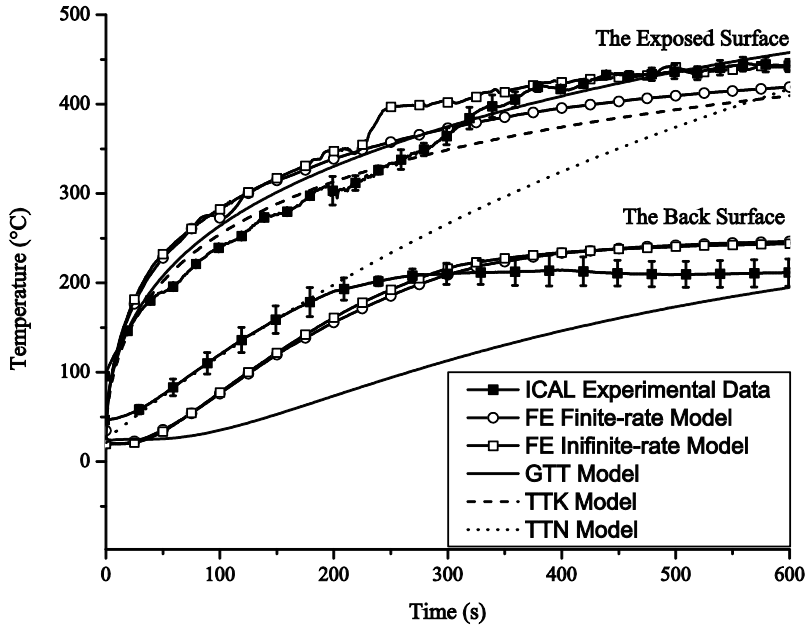

FIGURE 2.5: Comparisons of temperatures at the exposed surface and the back surface at 25 kW/m²

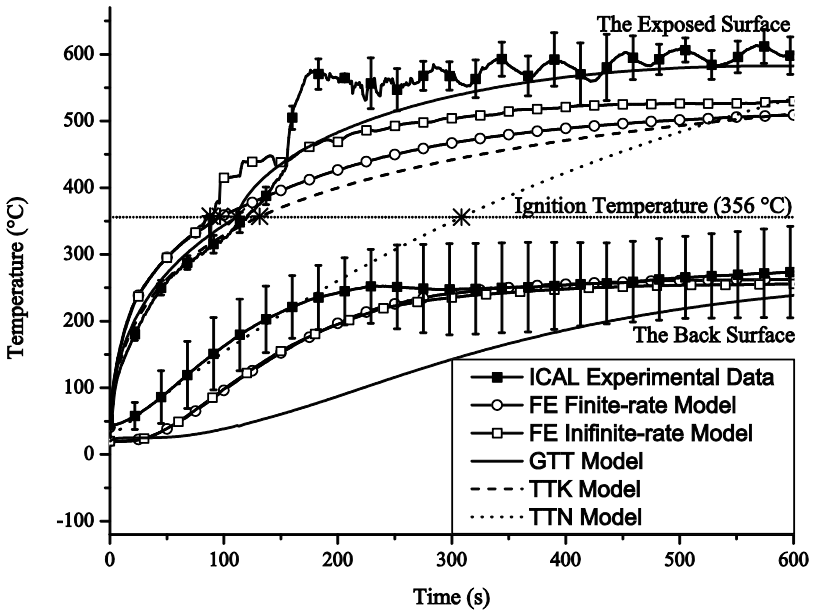

FIGURE 2.6: Comparisons of temperatures at the exposed surface and the back surface at 35 kW/m²

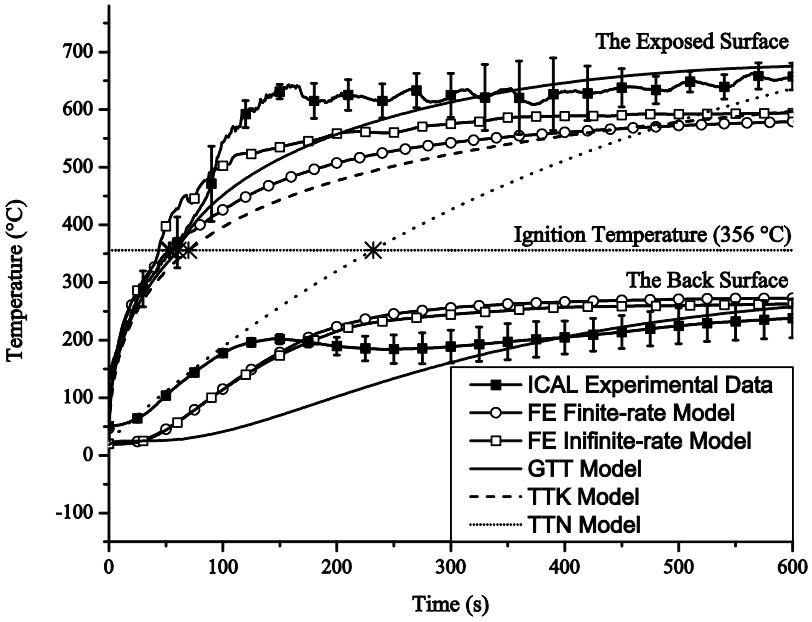

FIGURE 2.7: Comparisons of temperatures at the exposed surface and the back surface at 45kW/m²

2.8.2. Mass Loss and Mass Loss Rate per Unit Area

FIGURE 2.8, FIGURE 2.9, and FIGURE 2.10 show the mass loss rate per unit area subjected to external heat flux levels of 25kW/m², 35kW/m² and 45kW/m². It may be noted that the mass loss rate per unit area has the same unit as mass loss flux. The measurement of mass loss of composite is a scalar not a vector, hence we use mass loss rate per unit area to describe the mass loss of solid. It can be seen in FIGURE 2.8 that the FEM models showed better results compared with the GTT model. For flux levels of 35kW/m² and 45kW/m² (FIGURE 2.9 and FIGURE 2.10), the GTT model with flame effects showed good agreement, though the predicted values were higher than experimental data at the peak point. A more complicate temperature shift function is needed for more accurate mass loss rate predictions.

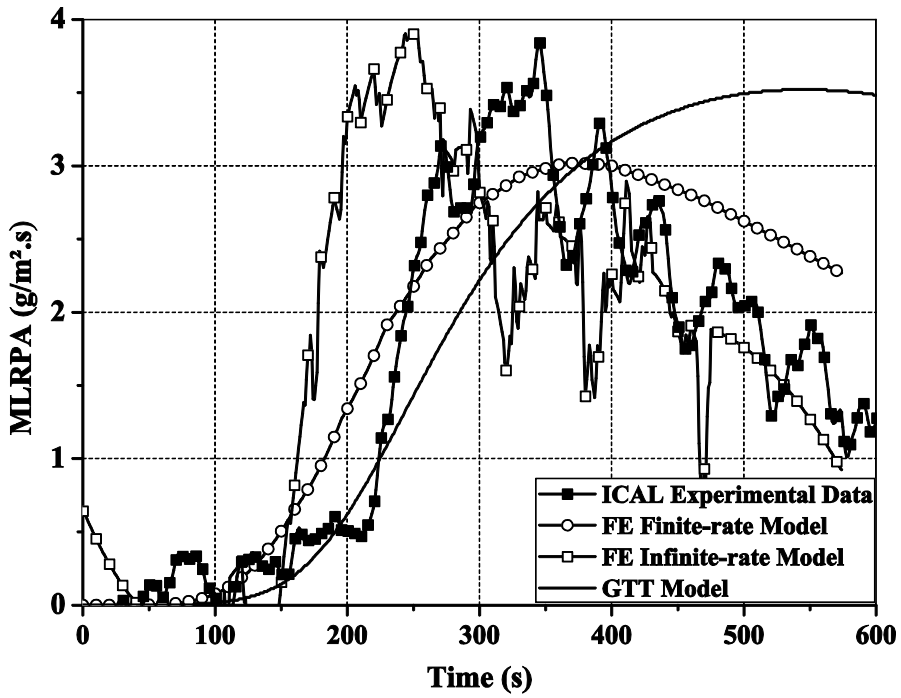

FIGURE 2.8: Comparisons of mass loss rate per unit area at 25kW/m²

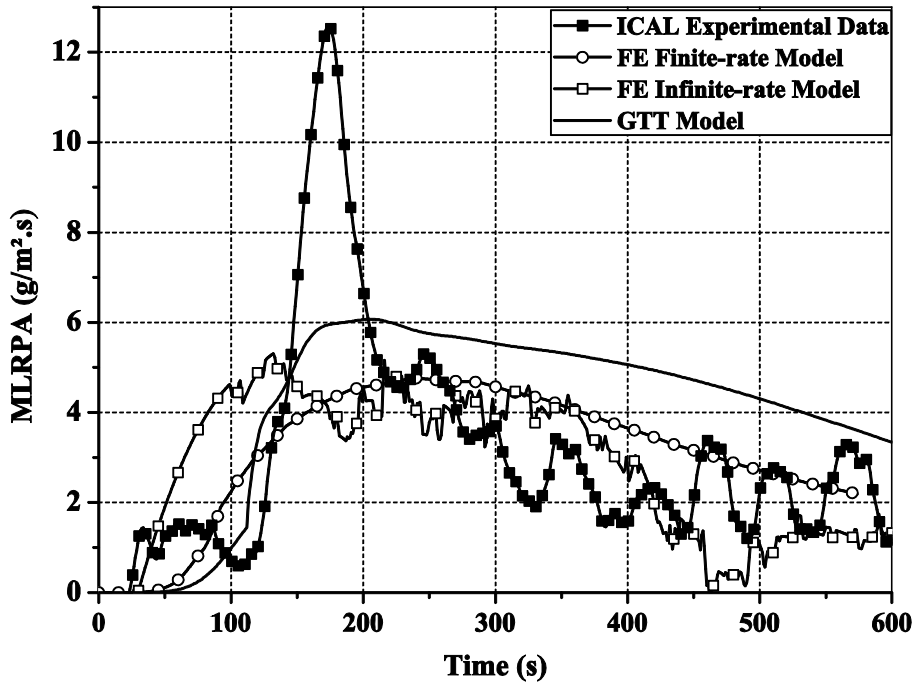

FIGURE 2.9: Comparisons of mass loss rate per unit area at 35kW/m²

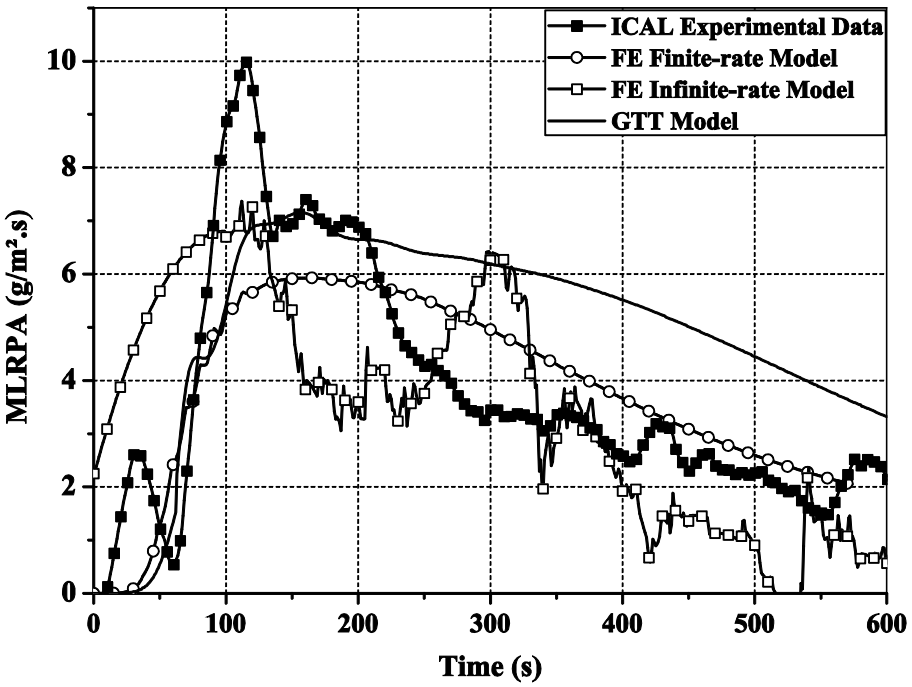

FIGURE 2.10: Comparisons of mass loss rate per unit area at 45kW/m²

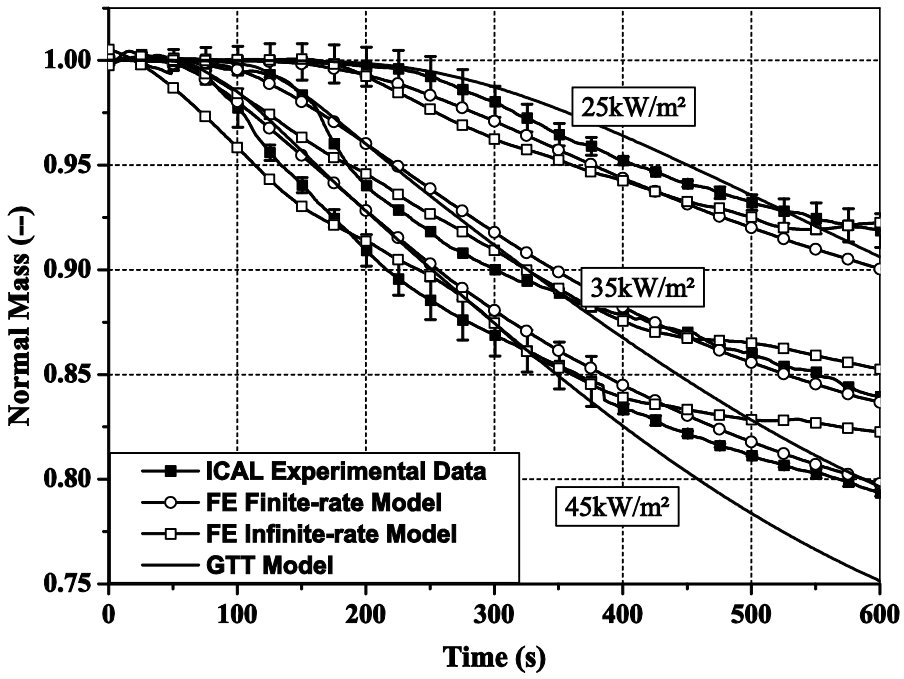

FIGURE 2.11: Comparisons of normalized mass

FIGURE 2.11 shows the normalized mass under external heat fluxes of 25kW/m², 35kW/m² and 45kW/m². Overall the results of the GTT model had higher but acceptable predictions comparing with the experiment data. Since the exposed surface temperature predictions were higher than those from experiment, mass loss is expected to be larger than the experimental data.

2.9. Conclusion

A simplified heat transfer model for predicting temperature increase, TTI and mass loss of combustible solid materials with general thermal thickness subjected to one-sided constant heat flux was developed, verified and validated. For practical use, an approximation of the theoretical solution was provided. The GTT model was validated by more agreeable temperature rise at the exposed surface and TTI predictions compared with ICAL experiment data of pultruded E-glass/polyester specimens. The ability of the GTT model to predict the temperature and mass loss (as well as mass loss rate) after ignition was also evaluated. By using a simple approximation of effective flame heating flux, the predictions were within acceptable range for fire safety design calculations. A more sophisticated flame heating flux model and temperature shift function for modified Arrhenius equation is recommended to get better temperature and mass loss predictions after ignition.

CHAPTER 3: HEATING RATE-RELATED IGNITION CRITERION FOR COMBUSTIBLE SOLIDS

3.1. Abstract

To construct a new ignition criterion which is capable to handle the variations of conditions, and meanwhile is easy to use and relate to fire spread, the author uses ignition temperature criterion as a start point to construct the new ignition criterion, referred as Heating Rate-related Ignition Temperature (HRIT) criterions, because the ignition temperature criterion is easy to use and relate to fire spread. In HRIT criterion, both surface temperature and its heating rate are used to determine the ignition. Predictions from HRIT ignition criterion compare well with experimental results of piloted ignitions of a thermoplastic material (Black PMMA), a thermoset composite material (E-glass fiber reinforced polyester composite) and a cellulosic material (Red Oak) subjected to variations of external heat fluxes. Potential factors affecting the accuracy and predictive capability of HRIT criterion are discussed at the end of this chapter. The method and its procedures to construct the heating rate-related temperature ignition criterion can be used to obtain the same ignition criterion for other combustible solids.

3.2.Introduction

Observations show that piloted ignition of a combustible solid will take place when the concentration of combustible gases from pyrolysis related to the Lower Flammability Limit (LFL) is attained at the location of the pilot (Chapter 2-11,

[5]). However, for simplicity and practical uses, different indirect ignition criteria have been used to predict the piloted ignition instead of directly using the LFL at the pilot location. Such indirect ignition criteria include Critical Surface Temperature (T_{ig}) [12, 13, 22, 23], Critical Average Solid Temperature [24], Critical Mass Flux [8, 29, 62, 63], Critical Char Depth [30], Critical Local Gas Temperature [38], Critical Total Reaction Rate in the boundary layer [9], Gas Temperature Gradient Reversal at the solid-gas interface [9, 43], and Critical Gas Phase Combustion Energy Density [44]. Among these criteria, due to its simplicity and reasonable accuracy, the Critical Surface Temperature criterion has been widely used in practice (Chapter 2-7, [5]), and has been proven to be the most useful ignition criterion [3]. The Critical Surface Temperature criterion has been used as the ignition criterion in the algorithms of Fire Dynamics Simulator (FDS), a popular and practical tool for solving practical fire problems and studying fundamental fire dynamics and combustion phenomena [33].

Although the concept of surface ignition temperature has been widely embraced by researchers and engineers, it comes with inherent limitations. For example, the ignition surface temperature of wood is not a constant but changes with external heat fluxes [4]. The same conclusion can also be drawn for thermoplastic material (e.g., PMMA) [31, 32, 34-38] and thermoset composites (e.g., E-glass/polyester) [11, 39]. The variation of surface ignition temperature under different external heat fluxes can be more than one hundred of Celsius degrees (e.g., the ignition temperature of PMMA ranges from 250 to 392 °C). Experimental observations also showed that a solid material will not undergo piloted ignition if the external heat flux is lower than its critical heat flux for piloted ignition, even if the actual surface temperature is higher than the established surface ignition temperature.

To address the above limitations of the surface temperature ignition criterion, this paper attempts to construct and validate a new ignition criterion which maintains the simplicity of the surface temperature ignition criterion, and meanwhile overcomes its limitations and improves the predictive capability. To achieve this goal, a generalized method was developed to account for the effect of heating rate on piloted ignition and a Heating Rate-related Ignition Temperature (HRIT) equation was constructed as the proposed ignition criterion. The new criterion was validated by comparing its predictions with experimental results of piloted ignition of three types of materials, a thermoplastic material (black PMMA), a thermoset composite material (E-glass/polyester) and a cellulosic material (Red Oak wood). Factors that affect the accuracy and predictive capability of the new criterion are also discussed.

3.3. Development of A Heating Rate-related Ignition Criterion

In this section a new ignition criterion integrating surface temperature and its heating rate for combustible solids will be developed based on theoretical relations and empirical evidences, referred as the Heating Rate-related Ignition Temperature criterion and simplified as the HRIT criterion. In this new ignition criterion, both Surface Temperature and its increasing rate are used to determine the ignition behavior. The details of the development of the HRIT criterion and its physical meaning are described in the following paragraphs.

Based on the surface temperature criterion for piloted ignition, a solid material will ignite when Equation 3.1 is satisfied,

$$T_{surf}(t) \geq T_{ig} \qquad \text{Equation 3.1}$$

In practice, the T_{ig} of a specific material in Equation 3.1 is usually considered as a constant value. However, experimental observations [4, 11, 31, 32, 34-39] have shown that T_{ig} is not only affected material properties (MPs) but also affected

external heat flux ($\dot{q}_e''$). As shown in FIGURE 3.1 to FIGURE 3.3 the ignition temperatures of PMMA, E-glass/Polyester Composite and Red Oak wood are affected by external heat flux $\dot{q}_e''$. And $\dot{q}_e''$ must be higher than the critical heat flux for piloted ignition ($\dot{q}_{cr}''$), which is defined as the minimum external heat flux required to achieve piloted ignition of an exposed sample.

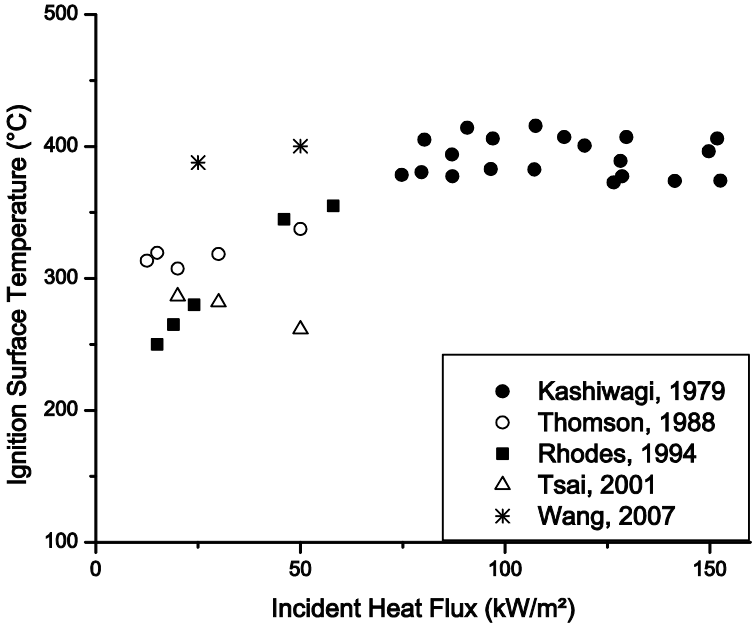

FIGURE 3.1: The ignition surface temperature of black PMMA at various external heat fluxes

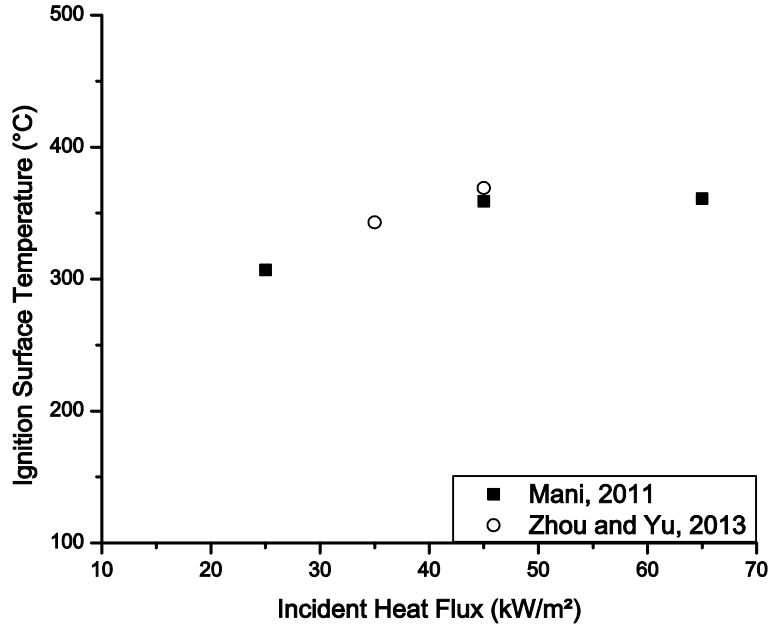

FIGURE 3.2: The ignition surface temperature of E-glass/Polyester at various external heat fluxes

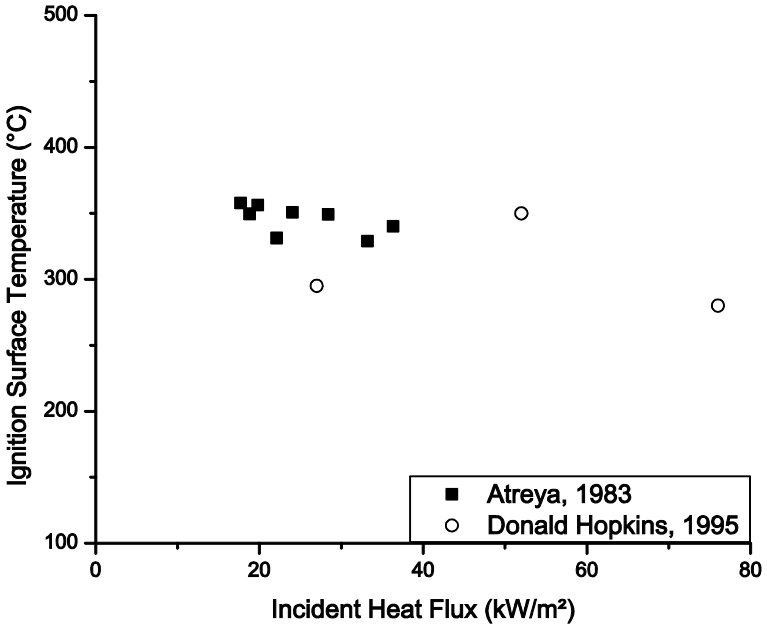

FIGURE 3.3: The ignition surface temperature of Red Oak at various external heat fluxes

These observations can be expressed by Equation 3.2.

$$T_{ig} = F(MPs, \dot{q}_e'') , \qquad \dot{q}_e'' \geq \dot{q}_{cr}'' \qquad \text{Equation 3.2}$$

It is obvious that the MPs such thermal and pyrolysis properties can affect the ignition temperature because these properties will affect the heat transfer and pyrolysis processes. The effect of $\dot{q}_e''$ on the ignition temperature is explained as the following. For a certain material, the external heat flux $\dot{q}_e''$ can directly affect the temperature, its increasing rate and temperature gradient through the thickness of the material. Thus, $\dot{q}_e''$ will affect the amount and rate of the pyrolyzed material, and consequently the amount of pyrolysis volatiles at the pilot location, which is eventually revealed as the Ignition Temperature (T_{ig}) changes. In principle, both temperature increasing rate and temperature gradient can be used with surface temperature to determine ignition. However, the temperature gradient is very difficult to measure. Hence the Surface Temperature Increasing Rate (STIR) is used by author because of following: (1) STIR increases with the increasing of external heat flux $\dot{q}_e''$ similar to temperature gradient (will be explained in the following section); (2) STIR is relatively easy to measure compared with temperature gradient.

In the following section, based on empirical observations and theoretical relations, the surface temperature and its increasing rate (or STIR) will be used to construct the Heating Rate-related Ignition Temperature (HRIT) criterion. To achieve this goal, the General Thermal Thickness (GTT) is used to as theoretical tool to construct the HRIT ignition criterion, instead of thermally thin or thermally thick models is due to the GTT model's broader applications. The GTT model does not require any assumption on thermal thickness, thus can be applied to materials with any thermal thickness.

Equation 3.3 is the solution of general thermal thickness model with the un-insulated back surface condition developed in Chapter 2.

$$T_{surf}(t) = T_0 + \dot{q}_e'' \left[\frac{\lambda + h_{eff}L}{h_{eff}\left(2\lambda + h_{eff}L\right)}\right] + \sum_{n=1}^{N} \theta_n e^{-\alpha\mu_n^2 t}, N \to \infty, t \geq 0 \quad \text{Equation 3.3}$$

With $\theta_n = -\frac{2\dot{q}_e''\lambda}{\left[\mu_n^2\lambda^2 + h_{eff}^2\right]L + 2h_{eff}\lambda}, tan\mu_n L = \frac{2\lambda h_{eff}\mu_n}{\lambda^2\mu_n^2 - h_{eff}^2}$

Differentiate both sides of Equation 3.3 with respect to time; we can get the Surface Temperature Increase Rate at ignition $STIR_{ig}$ as

$$STIR_{ig} = \dot{q}_e'' \left[\sum_{n=1}^{N} \frac{2\alpha\lambda\mu_n^2}{\left[\mu_n^2\lambda^2 + h_{eff}^2\right]L + 2h_{eff}\lambda} e^{-\alpha\mu_n^2 t_{ig}}\right], N \to \infty, t \geq 0 \text{ with } tan\mu_n L = \frac{2\lambda h_{eff}\mu_n}{\lambda^2\mu_n^2 - h_{eff}^2} \quad \text{Equation 3.4}$$

It may be noticed in Equation 3.4, both $STIR_{ig}$ and t_{ig} are unknown parameters. To understand the relation between $STIR_{ig}$ and $\dot{q}_e''$, we need to replace t_{ig} with known parameter, $\dot{q}_e''$.

Based on experimental observations the t_{ig} will decrease with the increase of $\dot{q}_e''$, it is reasonable to assume that the time-to-ignition is function of external heat flux Equation 3.5

$$t_{ig} = f_{t_{ig}}(\dot{q}_e'') \quad \text{Equation 3.5}$$

By combining Equation 3.5 into Equation 3.4 we can summarize $STIR_{ig}$ as a function of the corresponding heat flux $\dot{q}_e''$, and their relation can be described as Equation 3.6

$$STIR_{ig} = f_{STIR_{ig}}(\dot{q}_e'') \quad \text{Equation 3.6}$$

Assuming the Equation 3.6 is reversible, then we can get Equation 3.7

$$\dot{q}_e'' = {f_{STIR_{ig}}}^{-1}(STIR_{ig}) \quad \text{Equation 3.7}$$

We designate T_{ig}^{cr} as the surface temperature at ignition and $STIR_{ig}^{cr}$ as STIR at ignition when subjected to the critical heat flux of pilot ignition ($\dot{q}_{cr}''$). $\dot{q}_{cr}''$ is minimum external heat flux required to achieve piloted ignition of an exposed sample, which can be determined through experiments (e.g., 30 minutes, ASTM-E1354-11[64]).

Set δ as Equation 3.8

$$\delta = STIR_{ig} - STIR_{ig}^{cr} \quad \text{Equation 3.8}$$

Combining Equation 3.7 and Equation 3.8 into Equation 3.2 with the assumption of constant MPs in Equation 3.2 before ignition, Equation 3.2 can be rewritten as

$$T_{ig} = f(\delta), \delta \geq 0 \quad \text{Equation 3.9}$$

Apply the above procedure using Equation 3.10, the GTT solution with an insulated back surface condition obtained in Chapter 2; Equation 3.9 can also be concluded.

$$T_{surf}(t) = T_0 + \frac{\dot{q}_e''}{h_{eff}} + \sum_{n=1}^{N} \theta_n e^{-\alpha \mu_n^2 t}, N \to \infty, t \geq 0$$
$$\text{With } \theta_n = -\frac{2\dot{q}_e''\lambda}{\left[\mu_n^2\lambda^2 + h_{eff}^2\right]L + h_{eff}\lambda}, tan\mu_n L = \frac{h_{eff}}{\lambda\mu_n} \quad \text{Equation 3.10}$$

Hence Equation 3.9 is validated for both un-insulated and insulated back surface conditions. Next the author will show how to obtain expression of Equation 3.9. To achieve this, first the physical boundary conditions for Equation 3.9 need to be constructed.

The condition at $\delta = 0$ as shown in Equation 3.11 describes the minimum condition for a material to ignite (subjected to critical heat flux $\dot{q}_{cr}''$).

$$T_{ig}^{cr} = f(0) \qquad \text{Equation 3.11}$$

When δ or $\dot{q}_e''$ are very large (i.e., approaching infinity), the solid surface temperature increases very fast and ignition will occur quickly at a certain temperature. We designate this temperature as T_{ig}^{inf} and assume T_{ig}^{inf} is a constant. That is to say

$$\delta \to +\infty, \quad T_{ig}^{inf} = f(\infty) \qquad \text{Equation 3.12}$$

There are more than one solution of the HRIT Equation 3.9 with boundary conditions Equation 3.11 and Equation 3.12, such as Equation 3.13 and Equation 3.14.

$$T_{ig} = T_{ig}^{inf} - \frac{STIR_{ig}^{cr}}{STIR_{ig}}\left(T_{ig}^{inf} - T_{ig}^{cr}\right) \qquad \text{Equation 3.13}$$

$$T_{ig} = T_{ig}^{inf} - \left(T_{ig}^{inf} - T_{ig}^{cr}\right) \cdot \mathrm{e}^{-\beta[STIR_{ig} - STIR_{ig}^{cr}]} \qquad \text{Equation 3.14}$$

where β is the constant describing how fast T_{ig}^{cr} changes to T_{ig}^{inf} (i.e., the shape of the curve). Compared to Equation 3.13, Equation 3.14 is more agreeable with experimental data (e.g., piloted ignition of thermoplastic, thermoset and cellulosic materials) and also numerically more stable when $STIR_{ig}$ approaches to zero.

Combining Equation 3.1 and Equation 3.14, the ignition criterion can be obtained as Equation 3.15

$$T_{surf} \geq T_{ig}^{inf} - \left(T_{ig}^{inf} - T_{ig}^{cr}\right) \cdot \mathrm{e}^{-\beta[STIR - STIR_{ig}^{cr}]} \qquad \text{Equation 3.15}$$

FIGURE 3.4 shows the ignition and non-ignition zones defined by Equation 3.15. T_{ig}^{inf} is larger than T_{ig}^{cr} in FIGURE 3.4, but it is not necessarily always the case for all materials. For instance, the T_{ig}^{inf} of Red Oak is smaller than its T_{ig}^{cr} [15, 18,

65]. Mathematically, the proposed HRIT Equation can handle any situation. Physically, it may be easy to understand why T_{ig}^{inf} is higher than T_{ig}^{cr} for non-charring materials, such as PMMA.

This result is physically reasonable because of the temperature distribution along the depth inside the solid sample. Because ignition delay is longer at lower external heat fluxes, the thermal wave penetrates deeper into the sample and the pyrolysis zone is thicker. Therefore, to supply a given pyrolysate mass flux, a relatively lower temperature is required [47].

But the relationship between T_{ig}^{inf} and T_{ig}^{cr} is complicated for charring materials (such as red oak wood), because the charring process and the char affect the pyrolysis process. The rate and amount of charring as well as the properties of the char will affect the pyrolysis process. For charring materials, the relationship between T_{ig}^{inf} and T_{ig}^{cr} depends on the charring process and char properties of each specific material, in additional to thermal and pyrolysis properties of the material. Hence the relation between T_{ig}^{inf} and T_{ig}^{cr} becomes uncertain for charring materials, T_{ig}^{inf} may be greater or smaller than T_{ig}^{cr}.

Rearranging Equation 3.15 we can get Equation 3.16.

$$T_{surf} - T_{ig}^{inf} + (T_{ig}^{inf} - T_{ig}^{cr}) \cdot \mathrm{e}^{-\beta[\frac{STIR - STIR_{ig}^{cr}}{STIR_{ig}^{c}}]} \geq 0 \qquad \text{Equation 3.16}$$

Equation 3.16 can be explained as the following: when the surface temperature and the surface temperature increasing rate satisfy the Equation 3.16, the piloted ignition will occur. This indicates both surface temperature (T_{surf}) and its increasing rate (*STIR*) are factors determining the ignition behavior.

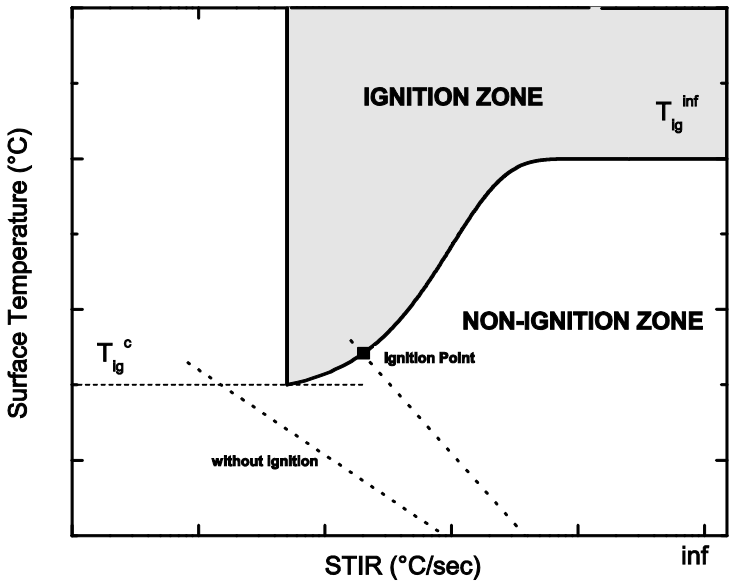

FIGURE 3.4: The schematic of Ignition Zones

3.4. Application of the New Ignition Criterion to Solid Materials

In this section, the capability of the HRIT criterion is demonstrated by comparing its predictions with experimental data on the piloted ignition of black PMMA, E-glass reinforced polyester composite, and Red Oak wood. These three materials were chosen for validation because the three materials are good representatives for the three kinds of combustible solid materials, thermoplastic, thermoset, and cellulosic materials. Furthermore, many experimental data for the piloted ignition of these three materials are available in the literature.

3.4.1. Application to Thermoplastic Material (Black PMMA)

FIGURE 3.1 shows the ignition temperature of black PMMA subjected to external heat fluxes from 11.2kW/m² up to 150kW/m² [31, 32, 34-38]. The details of experiments are listed in TABLE 3.2, with its material properties given in TABLE

3.1. The experimental data were used to determine T_{ig}^{inf}, T_{ig}^{cr}, $STIR_{ig}^{cr}$ and β so that the specific HRIT equation for black PMMA can be constructed.

As defined, T_{ig}^{inf} is ignition temperature subjected to the external heat flux approaching to infinite. In practice, it is not feasible to obtain infinite external heat flux. But based on the ignition zone shown in FIGURE 3.4, we know the ignition temperature will remain constant after certain heat flux (or STIR). Hence if the ignition temperature tends to be constant value with the increasing of external heat flux, that constant ignition temperature can be considered as T_{ig}^{inf}.

TABLE 3.1: Properties of the three materials used in the study

Material	Density ρ [kg/m³]	Heat Conductivity λ [W/m K]	Specific Heat Capacity c [J/kg.K]	Thermal Inertia $\alpha = \frac{\lambda}{\rho c}$ [m²/s]	Emissivity [--]
Black PMMA	1190 [36]	0.19 [35]	1812.3	8.81×10^{-8} [36]	0.95 [36]
E-glass / Polyester [11]	1888	0.2	1840	7.72×10^{-8}	0.99
Red Oak [18]	689	0.174	1368.168	1.85×10^{-7}	0.75

TABLE 3.2: Details of experimental results for piloted ignition

Authors & Year	Apparatus	Material	Specimen Size (mm)	Measured Method	Ignition Temperature
Kashiwagi, 1979 [32]	CO_2 Laser Heating Source	Black PMMA	75 x 75 x 12	thermocouple melted into surface	Onset of flaming
Thomson, 1988 [35]	ISO Ignitability Apparatus	Black PMMA	65 x 65 x 6	Thermocouple melted into the center surface	firepoint
Rhodes, 1994 [36]	Cone Calorimeter	Black PMMA	100 x 100 x 25	thermocouple melted into surface	Onset “Jump” of surface temperature
Tsai, 2001 [31]	Cone Calorimeter	Black PMMA	100 x 100 x 25	three thermocouples were located at surface	Onset “Jump” of surface temperature
Wang ,2007 [37]	Cone Calorimeter	Black PMMA	100 x 100 x 20	thermocouples in the hole of surface	Onset point
Mani, 2011 [39]	Cone Calorimeter	E-glass/ polyester	100 x 100 x 6.35	At the surface	Onset point
Zhou and Yu, in press [11]	ICAL	E-glass/ polyester	1000 x 1000 x 6.35	Four thermocouples were located under the surface IR Pyrometer	Onset point
Atreya, 1983 [18]	Fire Test Chamber	Red Oak	2 in diameter disk with ¾ in thickness	Measured below surface	Flashing point
Hopkins, 1995 [65]	Cone Calorimeter	Red Oak	100 x 100 x 31.75	Measured below surface	Onset point

Here the T_{ig}^{inf} was chosen as the average ignition surface temperature (392 °C) from 100 kW/m² to 150 kW/ m² [32] for the following reasons: First, in this range the ignition temperature tends to keep constant as shown in FIGURE 3.1. Second, 100 kW/m² to 150 kW/ m² is the largest heat flux available. Third, the ignition times for 100 kW/m² to 150 kW/ m² is 4 to 7 seconds, which is closed to the concept of instant ignition.

T_{ig}^{cr} and $STIR_{ig}^{cr}$ are the Ignition Surface Temperature and the ignition Surface Temperature Increasing Rate subjected to critical heat flux $\dot{q}_{cr}''$. The critical external heat flux of PMMA was reported as 11.2 kW/m² in [35], but its surface temperature curve was not available. The lowest heat flux with available temperature curve data is 15 kW/m². Hence the ignition surface temperature (250 °C) and its surface temperature increase rate (0.25°C/sec) measured under 15 kW/m² [36] were used as T_{ig}^{cr} and $STIR_{ig}^{cr}$.

β is the constant describing transition from T_{ig}^{cr} to T_{ig}^{inf}. It can be obtained through curve fitting using data set from [36] as listed in TABLE 3.3

Substitute the constants T_{ig}^{cr}, $STIR_{ig}^{cr}$, β and T_{ig}^{inf} into Equation 3.14, the HRIT Equation for black PMMA can be obtained as Equation 3.17.

$$T_{ig} = 392 - 142 \cdot exp[-0.4(STIR_{ig} - 0.25)] \qquad \text{Equation 3.17}$$

TABLE 3.3: Comparisons of predicted and experimental T_{ig} and t_{ig} for Black PMMA

External Heat flux [kW/m²]	Measured T_{ig} [°C]	STIR at ignition [°C/sec]	HRIT T_{ig} prediction [°C] and deviation [%]	GTT T_{ig} prediction [°C] and deviation [%]	Measured t_{ig} [sec]	GTT t_{ig} prediction [sec] and deviation [%]
15	250	0.25	250, (0.0)	251, (0.4)	263	238, (9.5)
19	265	0.47	262, (-1.2)	263, (-0.8)	135	144, (-6.7)
24	280	0.96	285, (1.8)	280, (0.0)	81	97, (-19.8)
46	345	2.28	329, (-4.7)	342, (-0.9)	Not measured	37
58	355	5.60	375, (5.7)	364, (2.5)	Not measured	28

The deviations of the ignition temperature prediction from Equation 3.17 with measured value at different external heat flux in [36] are within 6.0 % as shown in TABLE 3.3 and FIGURE 3.5. It may be noticed that only Rhodes (1994) data [36] of the 5 groups data shown in FIGURE 3.1 were used to compare in FIGURE 3.5. That is because other 4 data did not provide surface temperature curve to obtain STIR at ignition to compare. The same situation happened to Red Oak Sections too.

Next how to use the validated HRIT Equation 3.17 to determine the ignition in modeling will be introduced. First substitute the obtained constants $T_{ig}^{c}, STIR_{ig}^{c}$, β and T_{ig}^{inf} into Equation 3.16, the Ignition Zone for black PMMA can be obtained from Equation 3.18 as shown in FIGURE 3.5.

$$T_{surf} - 392 + 142 \cdot exp[-0.4(STIR - 0.25)] \geq 0 \qquad \text{Equation 3.18}$$

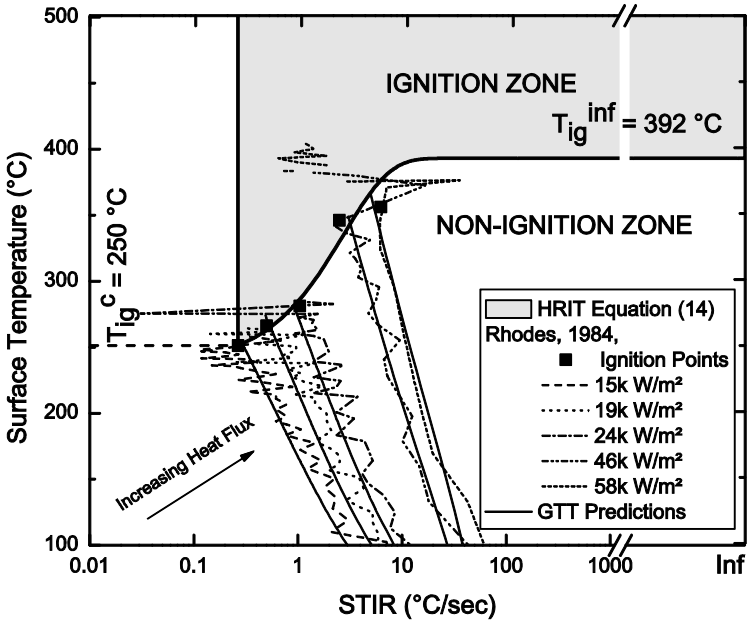

FIGURE 3.5: The ignition and non-ignition zones of black PMMA

If the point (STIR,T_{surf}) from temperature prediction model satisfies Equation 3.18, the material is considered to be ignited, and the point (STIR,T_{surf}) is the ignition point ($STIR_{ig}, T_{ig}$). Then the time-to-ignition (t_{ig}) can be determined using temperature prediction model by setting T_{surf}=T_{ig}.

The GTT model Equation 3.10 is chosen as the temperature prediction model for PMMA, according to the data obtained condition in [36]. And N is set to 5 in Equation 3.10 based on the recommendation in [66]. It can be seen in FIGURE 3.5 that the predicted curves using the GTT Equation 3.10 agree well with the experimental data. The predicted ignition points are shown as the intercepts between the prediction curves and Ignition Zone. Their deviations are less than 2.5% as shown in TABLE 3.3.

3.4.2. Application to Thermoset Material (E-Glass Reinforced Polyester Composite)

The experimental data used to identify the ignition zone of E-glass/polyester composite panels are from [11, 39]. The fiber fraction of the composite was 28.7% by volume and 40% by weight.

FIGURE 3.2 shows the ignition temperature of the composite subjected to external heat fluxes from 25kW/m² to 65kW/m². The test details are listed in TABLE 3.2. The material properties can be found in TABLE 3.1. Due to the limit available experimental data, the T_{ig}^{inf} was chosen as the average ignition surface temperature (363 °C) under external heat flux 45kW/m² and 65kW/ m² [11, 39]. The critical heat flux of E-glass/polyester composites was reported as 16~17kW/m^2 [67]. However, the surface temperature history curve under critical heat flux is not available, hence T_{ig}^{cr} and $STIR_{ig}^{cr}$ were assigned as ignition temperature (307 °C) and surface temperature increase rate (0.46°C/sec) at the lowest external heat flux (25 kW/m²) available. β was calculated through curve fitting using data in TABLE 4 [11, 39]. The HRIT Equation for E-Glass / Polyester composite is given by Equation 3.19 and its corresponding Ignition Zone is illustrated in FIGURE 3.6.

$$T_{ig} = 363 - 56 \cdot exp[-1.365(STIR_{ig} - 0.46)] \qquad \text{Equation 3.19}$$

The differences between the ignition temperature predicted by HRIT Equation 3.19 and the experimental data are within 3.0 % as shown in TABLE 3.4.

The time to ignition and ignition temperature also were predicted using the validated HRIT Equation 3.19 and GTT model. Both Equation 3.3 and Equation 3.10 were used to construct Surface Temperature vs STIR curves according to the boundary conditions in [11, 39]. N is set to 5 in Equation 3.3 and Equation 3.10. The deviation of predicted time-to-ignition and ignition temperature from the HRIT and

the GTT model are less than 12% and less than 5.5 % respectively as shown in TABLE 3.4.

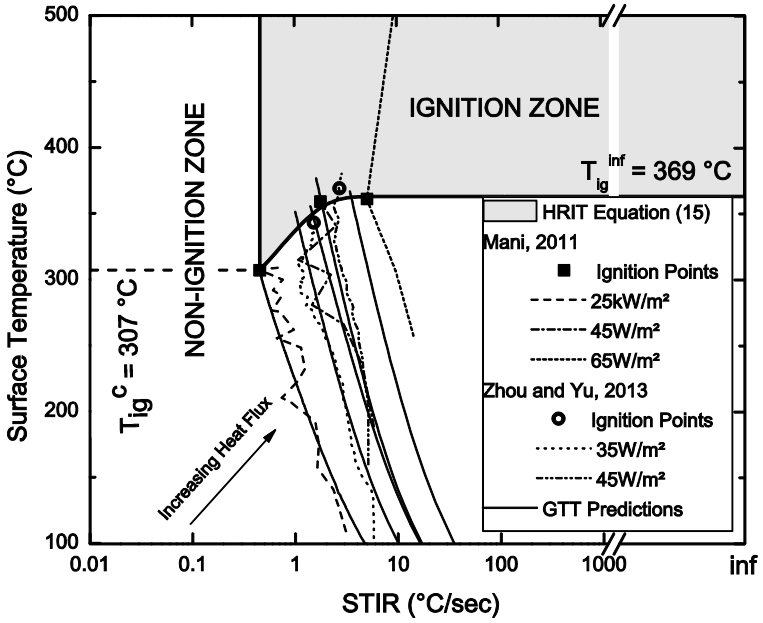

FIGURE 3.6: The ignition and non-ignition zones of E-glass/Polyester

TABLE 3.4: Comparisons of predicted and experimental T_{ig} and t_{ig} for E-glass/polyester composite

External Heat flux [kW/m²]	Measured T_{ig} [°C]	STIR at ignition [°C/sec]	HRIT T_{ig} prediction [°C] and deviation [%]	GTT T_{ig} prediction [°C] and derivation [%]	Measured t_{ig} [sec]	GTT t_{ig} prediction [sec] and deviation [%]
25 (Cone)	307	0.46	307, (0.0)	307, (0.0)	181	199, (-9.9)
35 (ICAL)	343	1.56	351, (2.2)	341, (-0.6)	110	110, (0.0)
45 (Cone)	359	1.81	354, (-1.4)	356, (-0.8)	80	76, (5.0)
45 (ICAL)	369	2.78	361, (-2.3)	349, (-5.4)	60	53, (11.7)
65 (Cone)	361	5.17	363, (0.6)	363, (0.6)	31	33, (-6.5)

3.4.3. Application to Cellulosic Material (Red Oak Wood)

The ignition properties of woods have been studied since the fire science began and its ignition behavior is quite complicate. Here we choose dry Red Oak as a representative cellulosic material because many ignition data are available in the literature. Material properties and experimental details are in TABLE 3.1 and TABLE 3.2 respectively. FIGURE 3.3 shows the ignition temperature of Red Oak as a function of heat flux between 17.7kW/m² and 76kW/m² [18, 65]. The ignition surface temperature (280°C) under 76kW/m²[65] was used as T_{ig}^{inf}. The critical heat flux of red oak is reported as 12.42kW/m^2 [68]. But since we don't have the surface temperature curve at the critical heat flux, the ignition temperature (358 °C) and surface temperature increasing rate (0.1 °C/sec) at the minimum available heat flux 17.4 kW/m² [18] are used as T_{ig}^{cr} and $STIR_{ig}^{cr}$. β was obtained through curve fitting using data set from [18]. The HRIT expression for red oak is shown as Equation 3.20 and the corresponding Ignition Zone illustrated in FIGURE 3.7. The differences between the predictions and experimental data are within 8.0 %.

$$T_{ig} = 280 + 78 \cdot exp[-0.1(STIR_{ig} - 0.1)] \qquad \text{Equation 3.20}$$

Equation 3.3 and Equation 3.4 are utilized to predict surface temperature vs STIR curves. N is set to 5 in Equation 3.3 and Equation 3.4. To keep FIGURE 3.7 clear, not all the predictions and experimental data are shown. But all the predictions are summarized in TABLE 5. It can be seen that the t_{ig} prediction in

TABLE 3.5 for Red Oak is not as good as the predictions for black PMMA and E-glass/polyester composites, that is because the conditions under which experiments were conducted was not exactly the same as the conditions under which the GTT Equation 3.3 and Equation 3.4 were developed.

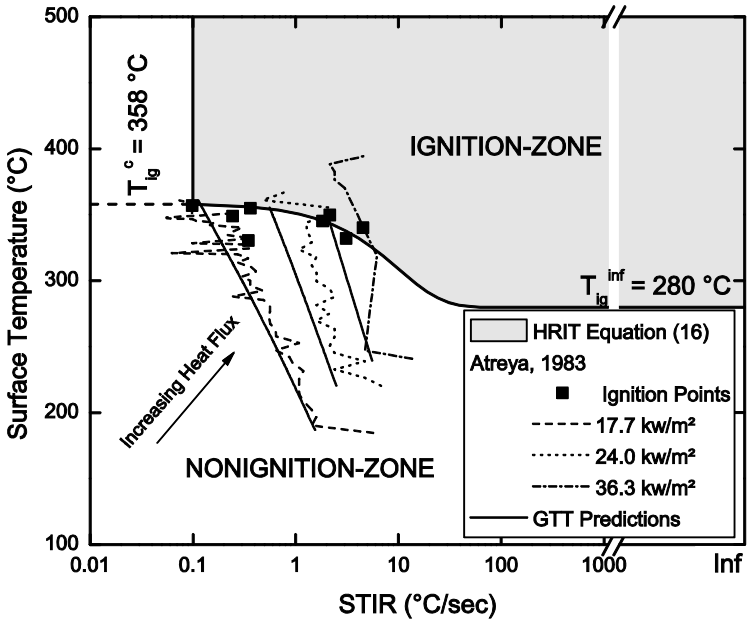

FIGURE 3.7: The ignition and non-ignition zones of Red Oak

TABLE 3.5: Comparisons of predicted and experimental T_{ig} and t_{ig} for Red Oak

External Heat flux [kW/m²]	Measured T_{ig} [°C]	STIR at ignition [°C/sec]	HRIT T_{ig} prediction [°C] and deviation [%]	GTT T_{ig} prediction [°C] and derivation [%]	Measured t_{ig} [sec]	GTT t_{ig} prediction [sec] and deviation [%]
17.7	358	0.10	358, (-0.0)	358.0, (0.0)	504	509, (-1.0)
18.8	350	0.24	357, (-0.2)	357.5, (-2.1)	310	360, (-16.1)
19.8	356	0.36	356, (-0.2)	357.0, (-0.3)	223	346, (-55.2)
22.1	331	0.35	356, (-7.7)	355.5, (-7.4)	140	170, (-21.4)
24.0	351	2.15	344, (1.8)	354.5, (-1.0)	100	150, (-50.0)
28.4	349	1.83	346, (-0.1)	351.5, (-0.7)	55	86, (-56.4)
33.2	329	3.09	338, (-1.7)	348.0, (-5.8)	44	65, (-47.7)
36.3	340	4.50	330, (3.0)	343.0, (-0.9)	37	46, (-24.3)

3.5. Discussion and Conclusion

The capability of the specific HRIT Equation 3.14 to predict the variation of ignition temperature due to different external heat fluxes under different testing conditions has been demonstrated for three different materials in the previous section.

However, it needs to be pointed out that the data used for T_{ig}^{cr} and $STIR_{ig}^{cr}$ for the three materials to obtain Equation 3.17, Equation 3.19 and Equation 3.20 are values from experimental results at the lowest heat flux for each material from limited available test results. The T_{ig}^{inf} values are from available experimental results under the highest external heat flux for each material. Hence Equation 3.17, Equation 3.19 and Equation 3.20 can be used if a material was subject to the same range of external heat flux. Outside this range, Equation 3.17, Equation 3.19 and Equation 3.20 should be used with caution.

In addition, according to the LFL concept, the piloted ignition behavior of a solid material is not only determined by its properties but also by the environmental gas phase properties. Hence, any factors affecting the solid or gas phase properties will change T_{ig}^{cr}, $STIR_{ig}^{cr}$, β and T_{ig}^{inf} in Equation 3.14, such as, the moisture content (MC), air flow velocity (V) and other possible factors as summarized in [6] (Pages 243-248). It was found that the ignition temperatures of radiata pine shifted up with increasing moisture content (from 0% to 30%) [45] and ignition temperatures of black PMMA moved up with increasing flow velocity (from 1 m/s to 1.75 m/s) [47].

Hence if a condition includes any of above factors which was extremely different from conditions when Equation 3.17, Equation 3.19 and Equation 3.20 were obtained, modifications for the HRIT Equations will be required. Further systematic

study is recommended to quantify the effects of these factors on T_{ig}^{inf}, T_{ig}^{cr}, $STIR_{ig}^{cr}$ and β, so that HRIT Equation accounting for various situations can be obtained.

In summary, a new ignition criterion considering the effect of heating rate on the piloted ignition of solids was developed and validated. The new criterion is represented as the HRIT Equation. In the HRIT criterion, both ignition temperature and its heating rate were used to determine ignition. By comparing the predictions from the new criterion with experimental data on the piloted ignition of thermoplastic, thermoset and cellulosic materials, it was demonstrated that differences from the predictions and experimental observations are within 8%. Factors influencing the solid and gas phase properties will affect the T_{ig}^{inf}, T_{ig}^{cr}, $STIR_{ig}^{cr}$ and β in HRIT criterion. Further systematic studies are needed to quantify the effects of different factors on the predictive capability of the HRIT criterion. The method and its procedures to construct the HRIT equation can be used to obtain the HRIT Equation for other solid materials.

CHAPTER 4: UNCERTAINTY AND SENSITIVITY ANALYSIS OF IGNITION PREDICTION MODEL

4.1. Abstract

The piloted flaming ignition of combustible solid materials is affected by many factors, such as properties of the combustible materials, heating source and surrounding environmental conditions. Hence for fire safety design purpose, it is essential to understand how the ignition behavior will vary due to variations of these properties. To achieve this, the sensitivity and uncertainty analysis on the GTT model and HRIT ignition criterion developed in Chapters 2 and 3, is conducted in this Chapter. The organization of this Chapter is as the following: first, the current sensitivity and uncertainty analysis techniques are briefly introduced; after that, the local sensitivity analysis is conducted on the GTT model and the HRIT criterion respectively; then a global sensitivity and uncertainty analysis, through the Monte Carlo simulation using the Latin Hypercube Sampling (LHS) method, is performed to the integrated ignition prediction model (the GTT combined with the HRIT ignition criterion). Based on the sensitivity and uncertainty analysis results, some useful conclusions are obtained, which can be served as a guide for fire safety design.

4.2. Introduction to Sensitivity and Uncertainty Analysis

The main purpose of sensitivity and uncertainty analysis is to evaluate the impact from the uncertainty in input(s) on the model output(s). The sensitivity analysis focuses on identifying the importance of the inputs while the focus of uncertainty analysis is to evaluate the uncertainty of the outputs brought by the variations of the inputs. This makes the sensitivity and uncertainty analysis techniques

the perfect tool to understand the variation of the ignition behavior due to variations of the properties of materials, heat source and surrounding environmental conditions, and to identify the importance of influencing factors.

Per Saltelli et al [50], sensitivity analysis (SA) methods can be classified into two categories: local sensitivity analysis and global sensitivity analysis. Local SA techniques reveal the local effect of the input variables on output(s) of the model by varying one input parameter at a time and holding other parameters constant. On the other hand, global SA techniques examine the global response of a model over the variation of all input parameters simultaneously.

The local SA is straight forward to understand. Compared with local analysis, the global SA is more complicated. There are many approaches to conduct the global analysis [50]. In this chapter, the Monte Carlo method based on the Latin Hypercube Sampling (LHS) technique is employed to conduct the global analysis. This method is chosen because of its flexibility and ease of implementation.

The uncertainty is usually evaluated by cumulative distribution function (CDF) and complementary cumulative distribution function (CCDF). The CDF describes the probability that the variable will be found at a value less than or equal to. Meanwhile CCDF presents the probability the variable with a larger value.

The details of sensitivity and uncertainty analysis techniques used in this chapter are summarized in the following paragraphs based on [48-50, 52]

4.2.1. Local Sensitivity Analysis

The underlying idea of sensitivity and uncertainty analysis is to evaluate the impact of the inputs (x) on the model outputs (y) as shown in Equation 4.1

$$y = f(x) \qquad \text{Equation 4.1}$$

Where f is the representation of model between x and y

x is the input parameters as shown in Equation 4.2, where nx is the number of input parameter *x*.

$$x = [x_1, x_2, \dots x_{nx-1}, x_{nx}] \quad \text{Equation 4.2}$$

y is the output parameters in Equation 4.3, while ny is the number of output y

$$y = [y_1, y_2, \dots y_{ny-1}, y_{ny}] \quad \text{Equation 4.3}$$

Local SA reveals the local effect of the input variables x_i on the model output y by varying one input parameter at a time while holding the other parameters constant. The local sensitivity can be evaluated through plotting the output y against the input factor x_i or first order partial derivative. In this study, the plotting method is used to investigate the local sensitivity of input parameter on the output.

4.2.2. Global Sensitivity Analysis

Global SA technique examines the global response of a model over the variation of all input parameters. In global SA, all input parameters are varied simultaneously, and each of them will be varied throughout the entire range. The input matrix (*X*) is obtained from the LHS procedure. The output vector (*Y*) is calculated by running the input matrix (*X*) through the integrated ignition prediction model (the GTT model with the HIRT ignition criterion)

Monte Carlo Method Using Latin Hypercube Sampling

The Monte Carlo Method is a popular global analysis method, which includes the following stages: (1) statistical distributions to each input variables are assigned. In this Chapter, the input variables are assigned as uniform distribution which means that each input in all the intervals of the same length on the distribution is equally probable; (2) then according to the distribution of variables, the input(s) variable is sampled in its feasible range; (3) the output(s) is obtained by running the sampled

input(s) through the given model; (4) using the obtained input(s) and corresponding output(s), the uncertainty and global sensitivity analysis can be conducted.

Latin Hypercube Sampling (LHS)

There are several sampling techniques, such as random sampling and Latin Hypercube Sampling (LHS). LHS allows an un-biased estimate of the average model output, with the advantage that it requires fewer samples than simple random sampling to achieve the same accuracy [69, 70], which by far is the most popular sampling scheme. Hence, LHS is used here. In the LHS method, sampling is performed independently for each parameter. The input parameter x_i range as Equation 4.4 is divided into *ns* equal (probability) intervals, where *ns* represents the size of sampling.

$$[Min(x_i), Max(x_i)] \qquad \text{Equation 4.4}$$

Each input variable will be randomly chosen from the intervals of the corresponding variable and each interval is chosen once only until the entire range for each parameter is explored. Then the input parameter matrix (*X*) can be obtained, consisting *ns* rows for the number of simulations and *nx* columns corresponding to the number of varied inputs, as shown in Equation 4.5

$$X = \begin{bmatrix} x_{1,1} & \cdots & x_{1,nx} \\ \vdots & \ddots & \vdots \\ x_{ns,1} & \cdots & x_{ns,nx} \end{bmatrix} \qquad \text{Equation 4.5}$$

where $x_{j,i}$ is the element of input matrix *X*, $i \in [1, nx], j \in [1, ns]$.

The rank transformed matrix RX can be obtained by ranking the LHS matrix.

$$RX = \begin{bmatrix} rx_{1,1} & \cdots & rx_{1,nx} \\ \vdots & \ddots & \vdots \\ rx_{ns,1} & \cdots & rx_{ns,nx} \end{bmatrix} \qquad \text{Equation 4.6}$$

where $rx_{j,i}$ is the rank of $x_{j,i}$.

The output (Y) can be obtained by running through the given model using the LHS sample matrix (X) as the following,

$$Y = \begin{bmatrix} y_{1,1} \\ \vdots \\ y_{1,ns} \end{bmatrix} \quad \text{Equation 4.7}$$

The rank transformed vector of output can be obtained as

$$RY = \begin{bmatrix} ry_{1,1} \\ \vdots \\ ry_{1,ns} \end{bmatrix} \quad \text{Equation 4.8}$$

where $ry_{j,1}$ is the rank of $y_{j,1}$.

The LHS (or Rank Transformed) matrix and the corresponding output (or Rank Transformed) matrix can be used for an uncertainty analysis and global sensitivity analysis.

Methods to Evaluate Global Sensitivity

There are many methods to evaluate the global sensitivities. The simplest procedure is scatter plot, which can reveal nonlinear or other unexpected relationships between the inputs and the output [52]. A scatter plot is simply a plot where the horizontal axis refers to the values of a sampled uncertain variable, while the vertical axis represents the corresponding values of the output. The global sensitivities can also be evaluated by the Pearson correlation coefficient (CC), the Partial Correlation Coefficient (PCC), the Standardized Regression Coefficients (SRCs) and the corresponding coefficients calculated with rank-transformed data (RCCs, SRRCs, and PRCCs).

The Pearson correlation coefficient is a simple method to provide a measure of the linear relationship between x_i and y. The Pearson correlation $r_{xy}(i)$ between x_i and y is defined as

$$r_{xy}(i) = \frac{\sum_{j=1}^{ns}(x_{j,i} - \bar{x}_i)(y_{j,1} - \bar{y})}{\left[\sum_{j=1}^{ns}(x_{j,i} - \bar{x}_i)^2\right]^{\frac{1}{2}}\left[\sum_{j=1}^{ns}(y_{j,1} - \bar{y})^2\right]^{\frac{1}{2}}} \quad \text{Equation 4.9}$$

Where $\bar{x}_i = \frac{1}{ns}\sum_{j=1}^{ns} x_{j,i}$, $\bar{y} = \frac{1}{ns}\sum_{j=1}^{ns} y_{j,1}$

Standardized Regression Coefficient (SRC) is defined as Equation 4.10. The absolute value of SRC is used to provide a measure of variable importance.

$$SRCs(i) = \frac{b_i \hat{y}_{x_i}}{\hat{s}_y} \quad \text{Equation 4.10}$$

The standardized derivations are defined as

$$\hat{s}_y = \left[\sum_{j=1}^{ns} \frac{(y_{j,1} - \hat{y}_{x_i})^2}{ns - 1}\right]^{\frac{1}{2}} \text{ and } \hat{s}_{x_i} = \left[\sum_{j=1}^{ns} \frac{(x_{j,1} - \bar{x}_i)^2}{ns - 1}\right]^{\frac{1}{2}} \quad \text{Equation 4.11}$$

The regression model in Equation 4.12, is usually constructed by the least squared procedure

$$\hat{y}_{x_i} = b_0 + \sum_{j=1}^{ns} b_i x_{j,i} \quad \text{Equation 4.12}$$

And coefficients b can be determined by Equation 4.13

$$b = (X^T X)^{-1} X^T Y \quad \text{Equation 4.13}$$

Compared with the CC, which represents the linear relationship between x_i and y, the partial correlation coefficient (PCC) provides a measure of the strength of linear relationship between x_i and y after the linear effects of the other elements have been

removed. The PCC between y and x_i can be defined in the following manner. Two regression models for x_i and y are first constructed as Equation 4.14

$$\hat{x}_i = c_0 + \sum_{\substack{j=1 \\ j\neq i}}^{ns} c_i x_{j,i}, \hat{y} = b_0 + \sum_{\substack{j=1 \\ j\neq i}}^{ns} b_i x_{j,i} \qquad \text{Equation 4.14}$$

and PCC is defined as CC between $x_i - \hat{x}_i$ and $y - \hat{y}$.

The coefficient (CC, SRC, or PCC) obtained based on raw inputs and output is used to evaluate the linear relationship between inputs and output variable. On the other hand, the Rank Correlation Coefficient (RCC), Standardized Rank Regression Coefficients (SRRCs), and Partial Rank Correlation Coefficients (PRCCs), obtained based on rank-transformed data as shown in Equation 4.6 and Equation 4.8, perform better when the relationships are nonlinear but still monotonic.

4.2.3. Uncertainty Analysis (UA)

The UA can be evaluated by the Cumulative Distribution Function CDF and Complementary Cumulative Distribution Function (CCDF) [50].

The CCDF for the Monte Carlo Method using the LHS method can be determined as Equation 4.15

$$prob(y > Y) = \sum_{i=1}^{k} \delta_Y(y_{j,1}) \left(\frac{1}{ns}\right) \qquad \text{Equation 4.15}$$

where $prob(y > Y)$ is the probability that a value larger than Y will occur and

$$\delta_Y(y_{j,1}) = \begin{cases} 1 \; if \; y > Y \\ 0 \; if \; y \leq Y \end{cases} \qquad \text{Equation 4.16}$$

The CDF is defined as Equation 4.17, CDF will be used in this Chapter.

$$prob(y \leq Y) = 1 - prob(y > Y) = 1 - \sum_{i=1}^{k} \delta_Y(y_{j,1}) \left(\frac{1}{ns}\right) \qquad \text{Equation 4.17}$$

4.3. Sensitivity and Uncertainty Study of GTT and HRIT Models

In this section, the above sensitivity and uncertainty analysis techniques will be applied to the GTT model and the HRIT criterion to understand how the input parameters will affect the output. To achieve this goal, first the local SA procedure in Section 4.2.1 will be applied to the GTT and the HRIT models respectively to understand how the surface temperature and its increasing rate, and ignition zone response to the input variations separately. Then uncertainty brought by input parameter variations to the ignition prediction model (the GTT model combined with the HRIT ignition criterion) will be evaluated through both global and local sensitivity and uncertainty techniques.

4.3.1. Local SA Procedure and Results for the GTT Model

The parameters shown in TABLE 4.1are from E-glass/polyester composite material subjected to 45 kw/m^2 external heat flux under Cone Calorimeter test condition [39], and will be used as the inputs to conduct the sensitivity study for the GTT model. According to the HRIT ignition criterion, ignition is determined both by the surface temperature and its increasing rate, hence both the surface temperature and its increasing rate are considered as outputs. Their responses to the input parameter variations will be examined using the GTT model. To compare the importance within the input parameters in TABLE 4.1, the local SA was conducted by varying each parameter ±15% from the measured value while other parameters remain unchanged.

FIGURE 4.1 to FIGURE 4.7 show the surface temperature and its increasing rate response to the ±15% variation of each input parameter respectively. According to FIGURE 4.1, FIGURE 4.5 and FIGURE 4.6, the thickness (L), heat convection coefficient (h) and the effect of initial temperature (T_0) are hardly observed within ±15% variation. Both T_{surf} and *STIR* decrease with the increasing of the thickness (L)

and heat convection coefficient (h). The surface temperature (T_{surf}) and its increasing rate ($STIR$) decreases with the increasing of initial temperature (T_0).

The density ρ, heat capacity c, and heat conduction coefficient λ have the larger effect to the surface temperature and its increasing rate than the effect of L and h, based on FIGURE 4.2, FIGURE 4.3 and FIGURE 4.4. The external heat flux (q_e) is the most important factor to affect the T_{surf} and $STIR$ as shown in FIGURE 4.7.

In summary, within ±15% variation, q_e, ρ, c, and λ can significantly affect T_{surf} and STIR, and thickness (L), heat convection coefficient (h) and initial temperature (T_0) have the minimal impact on the outputs as shown in TABLE 4.1. According to the observations in FIGURE 4.1 to FIGURE 4.7, the importance index of each parameter in terms of its effects to surface temperature (T_{surf}) and the increasing rate ($STIR$) are also summarized in TABLE 4.1. The index of importance is comparative value within the 7 input parameters. The larger the index implies the larger the effect to the output it has. And the positive sign (+) means T_{surf} (or STIR) increases with the increasing of the parameter; the negative sign (-) shows the opposite is true.

TABLE 4.1: Input parameters of E-glass/polyester composite material for the GTT model

No.	Parameter [unit]	Symbol	Value	Importance Index	
				T_{surf}	STIR
1	Thickness [mm]	L	6.35	-2	-2
2	Density [kg/m3]	ρ	1888	-3	-3
3	Heat Capacity [J/(kg K)]	c	2068	-3	-3
4	Heat Conductivity [W/m K]	λ	0.2	-3	-3
5	Heat Convection Coefficient [W/m2 K]	h	10	-2	-2
6	Initial Temperature [K]	T_0	25	+1	-1
7	External Heat Flux [kW/m²]	$\dot{q}''_e$,	45	+4	+4

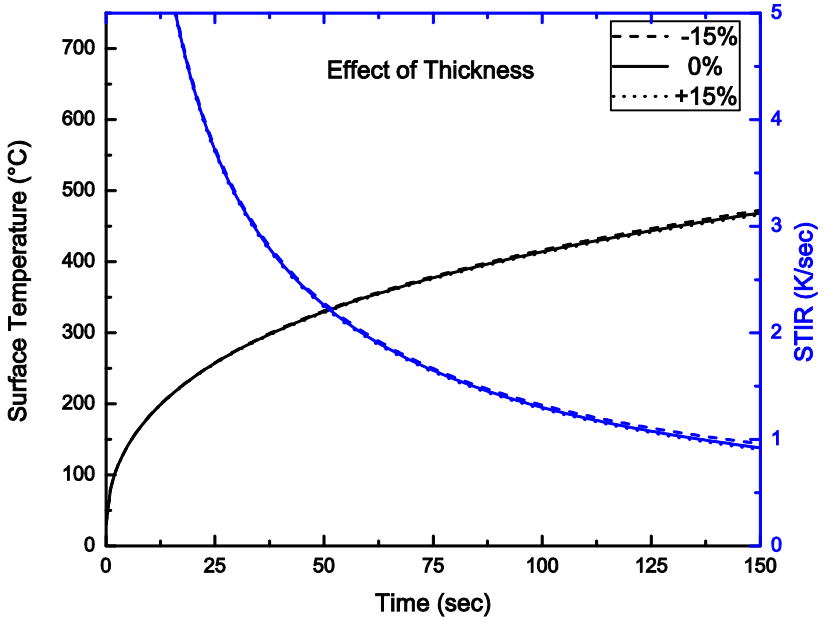

FIGURE 4.1: The effect of thickness on surface temperature

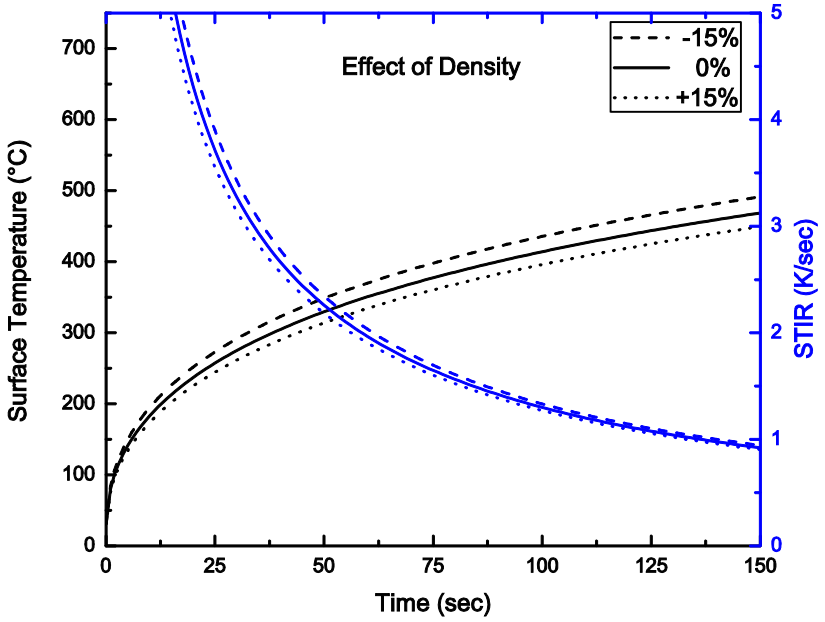

FIGURE 4.2: The effect of density on surface temperature

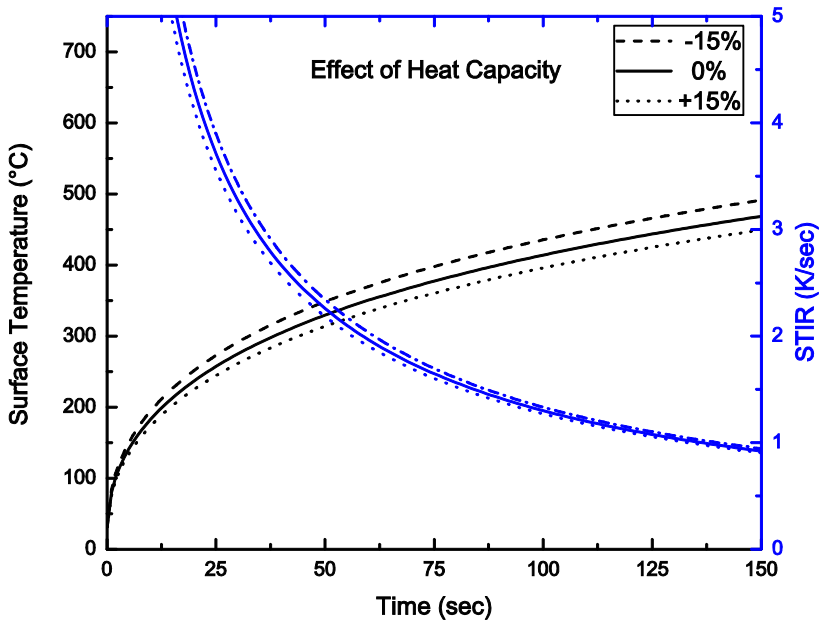

FIGURE 4.3: The effect of heat capacity on surface temperature

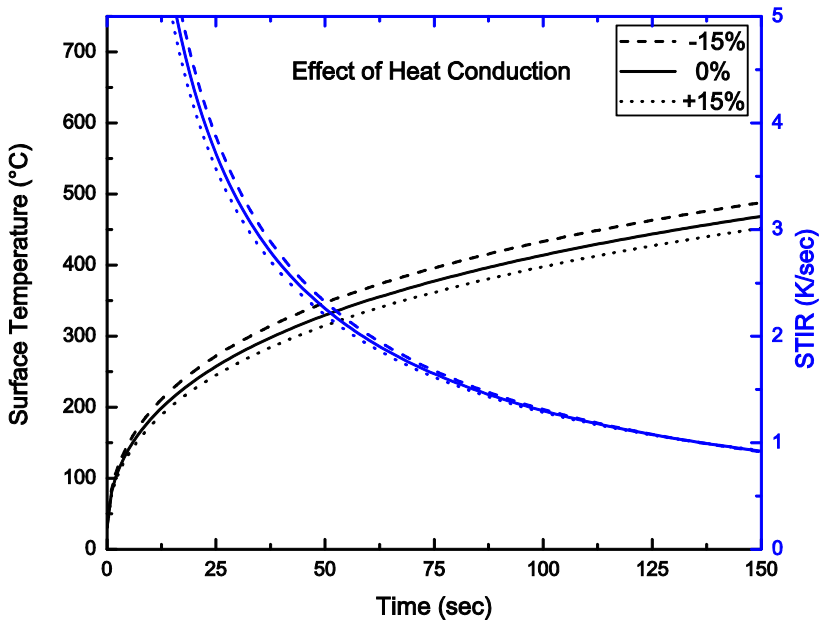

FIGURE 4.4: The effect of heat conduction on surface temperature

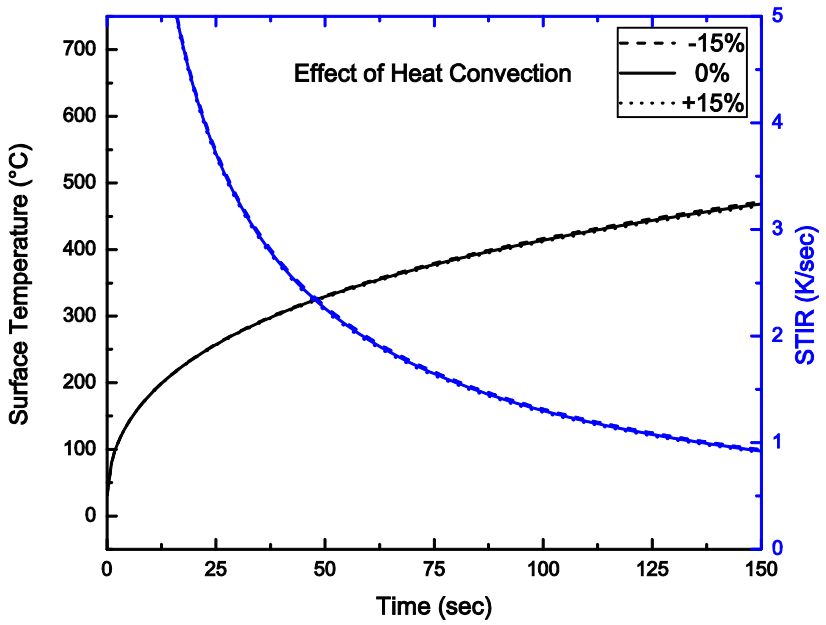

FIGURE 4.5: The effect of heat convection coefficient on surface temperature

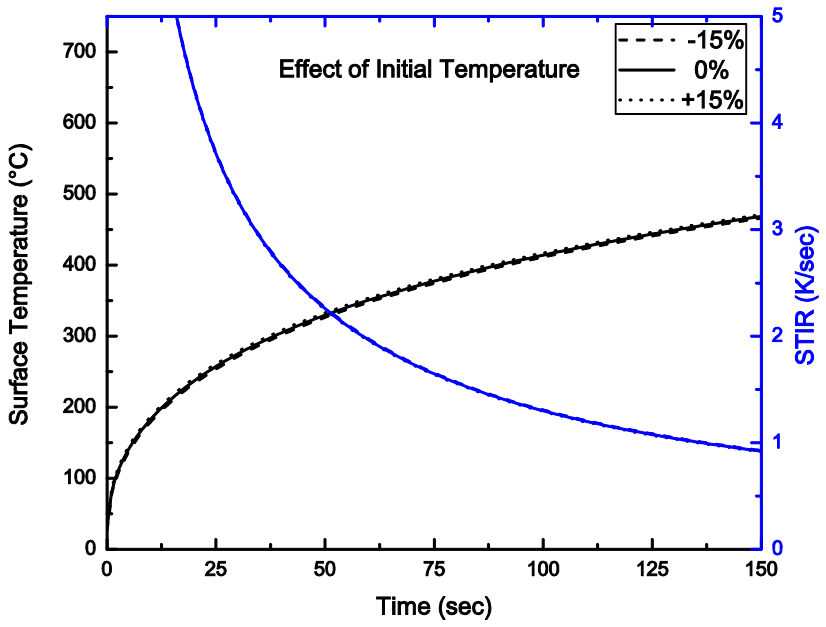

FIGURE 4.6: The effect of initial temperature on surface temperature

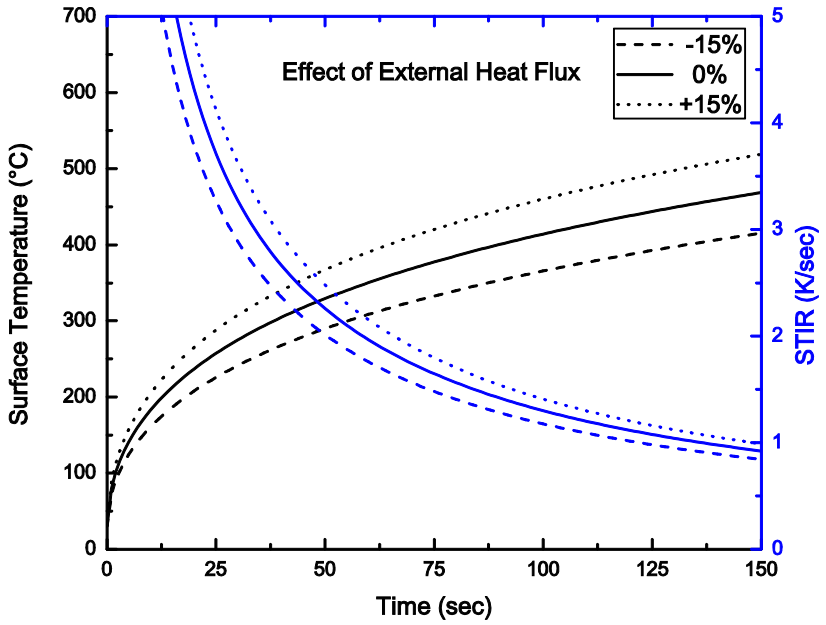

FIGURE 4.7: The effect of external heat flux on surface temperature

4.3.2. Local SA Procedure and Results for the HRIT Model

As discussed in Chapter 3, the parameters in the HRIT model are not always constant for the same material; they may change due to the surrounding environmental conditions, moisture content and others. For example the ignition temperature will increase with moisture. Hence it is important to investigate how the input parameters of the HRIT model will affect the ignition zone. By relating the surrounding environmental conditions, moisture content or others to the input parameters of HRIT criterion, the ignition behavior can be better understood. To achieve this goal, in this section, the parameters of the HRIT ignition criterion obtained in Chapter 3 (TABLE 4.2) for the E-glass/polyester composite material are used as basis to conduct the sensitivity study. The Ignition Zone (output) response to the input parameter variations will be investigated by varying ±15% each parameter in TABLE 4.2 while other parameters remain unchanged.

TABLE 4.2: Input parameters of E-glass/polyester composite material for the HRIT ignition Criterion

No.	Parameter [unit]	Symbol	Value	Importance Index
1	Critical Surface Temperature Increasing Rate at ignition [K/sec]	$STIR_{ig}^{c}$	0.46	1
2	[sec/K]	β	1.365	-2
3	Ignition Temperature at Critical Heat Flux [°C]	T_{ig}^{c}	307	-3
4	Ignition Temperature at infinite Heat Flux [°C]	T_{ig}^{inf}	363	-4

FIGURE 4.8 to FIGURE 4.11 show changes of the Ignition Zone corresponding to the input parameter variations. It can be seen that the ignition zone changed significantly corresponding to the T_{ig}^{inf} and T_{ig}^{c} variations. The ignition zone decreases with the increasing of T_{ig}^{inf} and T_{ig}^{c} (FIGURE 4.10 and FIGURE 4.11). β has the least positive effect on the ignition zone compared with other parameters. $STIR_{ig}^{c}$ has bigger effect to the ignition zone than β, but less effect compared to T_{ig}^{inf} and T_{ig}^{c}. However, the effect of $STIR_{ig}^{c}$ on ignition zone is more complicated compared with the other three parameters. As shown in FIGURE 4.9 to FIGURE 4.11, the smaller ignition zone due to the larger value of β, T_{ig}^{inf} and T_{ig}^{c} is included in the larger ignition zone, which implies for all the situations the material with larger β, T_{ig}^{inf} and T_{ig}^{c} will be more difficult to ignite; However, the smaller ignition zone resulting from $STIR_{ig}^{c}$ is not included in the larger ignition zone as shown in FIGURE 4.8, which means for some material with smaller ignition zone caused by $STIR_{ig}^{c}$ only may be easier to ignite than the one with larger ignition zone. As discussed in Chapter

3, $STIR_{ig}^{c}$ is directly related to the critical heat flux ($\dot{q}''_{cr,}$). Hence we can further conclude that the material with smaller critical heat flux is not necessarily easier to ignite compared with the material with larger critical heat flux at any circumstance.

The importance index of HRIT inputs to ignition zone are summarized in TABLE 4.2 based on the observations in FIGURE 4.8- FIGURE 4.11. The larger the index means the larger the effect. And the positive sign (+) means ignition zone increases with the increasing of the parameter; the negative sign (-) implies the opposite is true. Since it is hard to determine the effect of $STIR_{ig}^{c}$ is positive or negative, no sign is assigned to $STIR_{ig}^{c}$ as shown in TABLE 4.2.

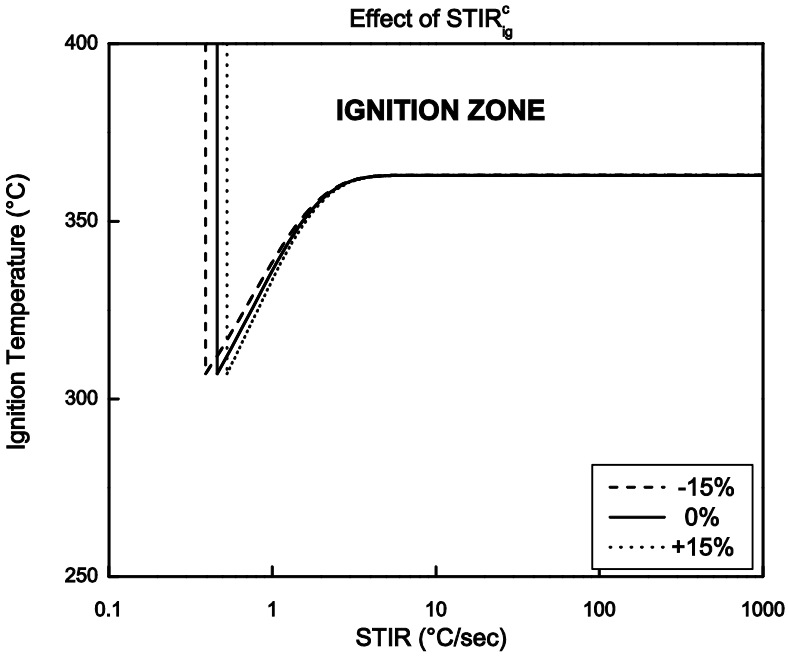

FIGURE 4.8: The effect of critical surface temperature increasing rate at ignition on ignition zone

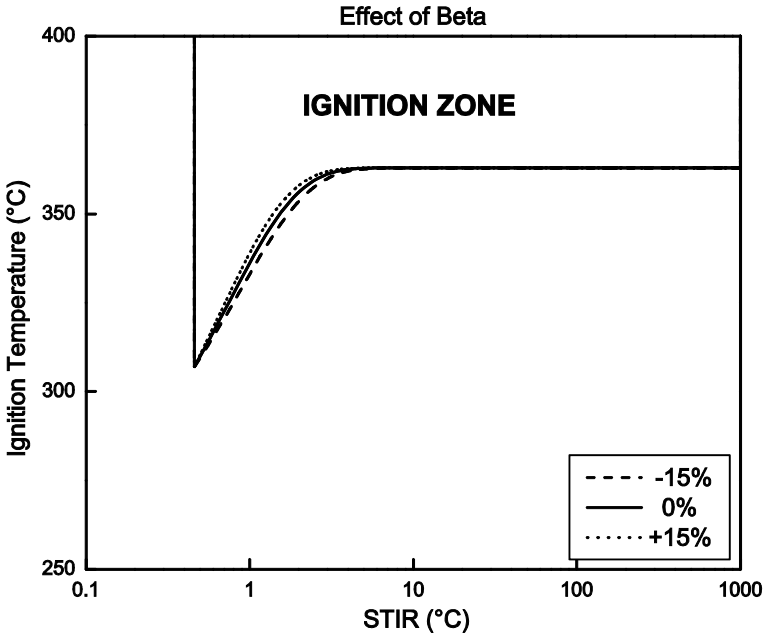

FIGURE 4.9: The effect of beta on ignition zone

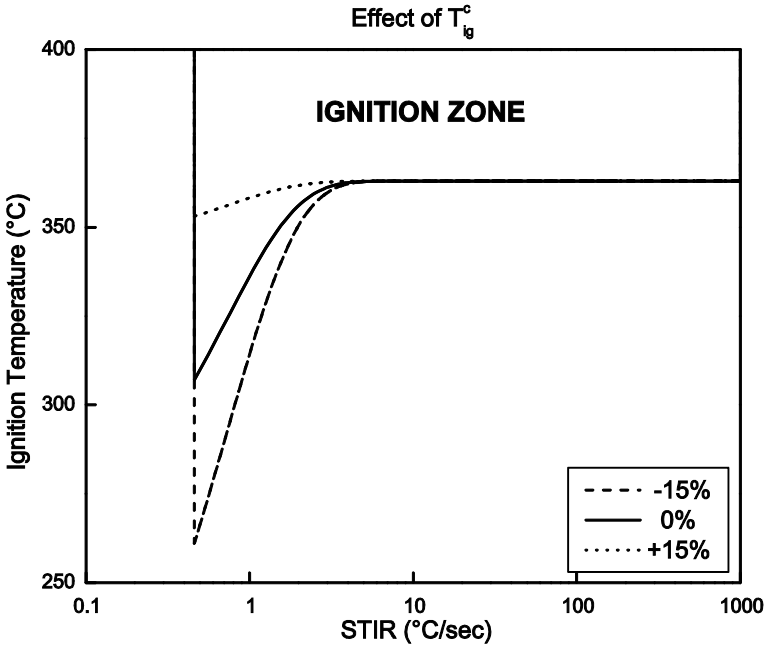

FIGURE 4.10: The effect of ignition temperature at critical heat flux on ignition zone

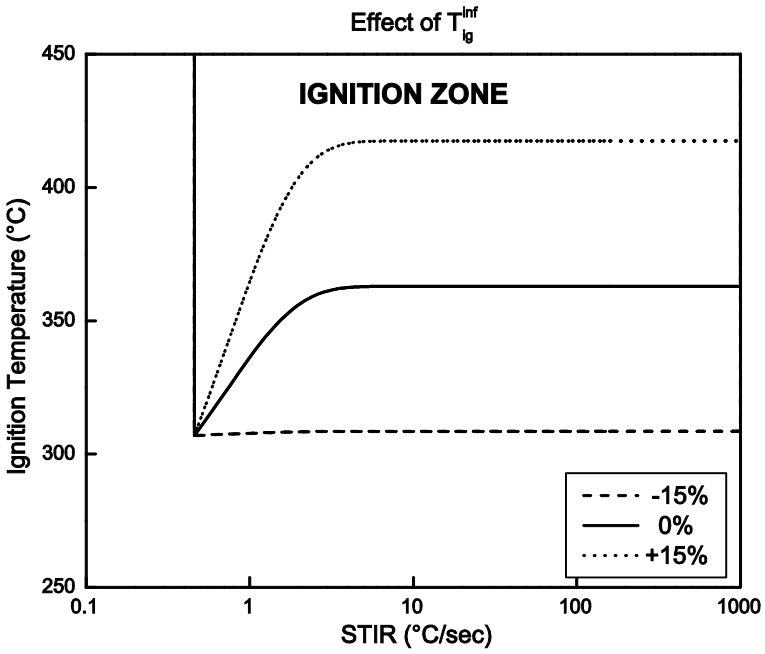

FIGURE 4.11: The effect of ignition temperature at infinite heat flux on ignition zone

4.3.3. Sensitivity and Uncertainty of the Integrated Ignition Prediction Model

In this section, we integrate the temperature prediction GTT model with the HRIT ignition criterion to determine the ignition. The resulting mode is referred as the integrated ignition prediction model. The parameters of the E-glass/polyester composite material are used as inputs to conduct sensitivity and uncertainty study, as listed in TABLE 4.1 and TABLE 4.2. The time-to-ignition (TTI) is considered as the output parameter. The distribution is assigned as varying ±15% of the experimental values.

Both local and global analysis will be conducted to investigate the sensitivity and uncertainty of the integrated ignition prediction model. For local SA study, each input will vary within its range while other parameters remain constant, and the TTI will be calculated each time through integrated ignition prediction model.

In the global Monte Carlo analysis, the size of sampling (*ns*) is set to 1000. Then a 1000×11 input parameter matrix ($X_{ns\times nx}$) is generated using the LHS method by varying ±15% of the input parameters listed in TABLE 4.1 and TABLE 4.2. 1000 sample points are run through the integrated ignition prediction model to obtain the output (TTI) vector ($Y_{ns\times 1}$). Then the $X_{ns\times nx}$ and $Y_{ns\times 1}$ are used as the basis to conduct the global sensitivity and uncertainty analysis.

Uncertainty Analysis Results

FIGURE 4.12 shows the CDF curve calculated based on the input matrix $X_{ns\times nx}$ and output vector $Y_{ns\times 1}$. It can be seen the ignition most likely (80%) occur at the range of TTI within 55 to 110 sec. This CDF curve can give the designer a roughly idea when ignition may occur under certain external heat flux range (within±15% of 45 kW/m^2).

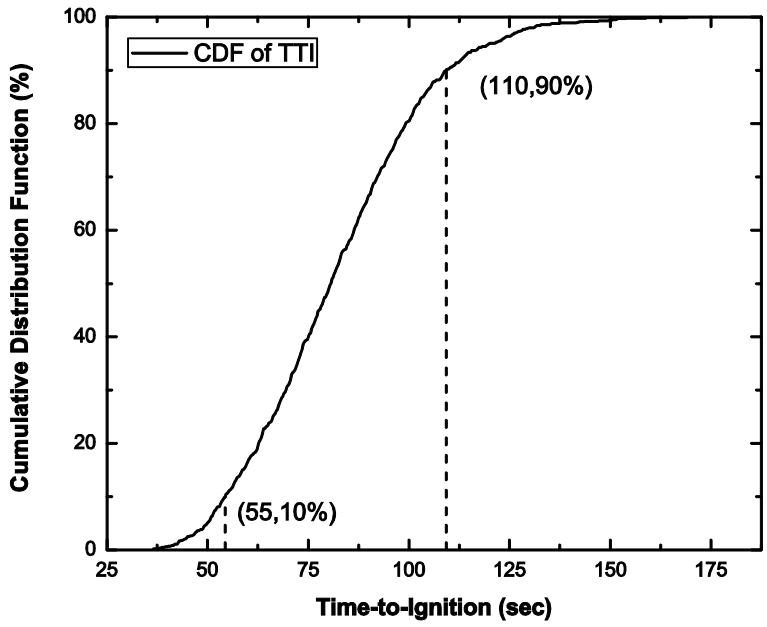

FIGURE 4.12: The cumulative distribution function curve of time-to-ignition

Sensitivity Analysis Results

The results of the global and local sensitivity results are plotted as shown in FIGURE 4.13 to FIGURE 4.23. The global sensitivity index (CC, RCC, SRC, SRRC, PCC, and RPCC) calculated from the input matrix $X_{ns\times nx}$ and their corresponding outputs $Y_{ns\times 1}$, are shown in TABLE 4.3. They can be used as the measurement of the importance of the input parameters to the output TTI. Negative sign of the index means TTI decreases with increasing of the input parameter, and positive sign implies that the TTI increases with increasing of the input parameter. The absolute value of the index is the measurement of its importance to the output (TTI). It may be noticed that the signs in TABLE 4.3 are different from the ones in TABLE 4.1 and TABLE 4.2. That's because the faster surface temperature increases and the larger ignition zone is, the shorter the TTI will be.

Based on the results in TABLE 4.3 and FIGURE 4.13 to FIGURE 4.23, we can obtain similar conclusions as in Section 4.3.1 and 4.3.2: (a). The external heat flux (q_e) is the significant factor affecting TTI, and TTI decreases with the increasing of the q_e showing in TABLE 4.3 and FIGURE 4.19; (b). Density ρ, heat capacity c, and heat conductivity λ are also important factors to TTI as shown in FIGURE 4.14 to FIGURE 4.16 and TABLE 4.3; (c). Thickness (L), heat convection coefficient (h) and initial temperature (T_0) hardly changes TTI as illustrated in FIGURE 4.13, FIGURE 4.17 and FIGURE 4.18 respectively; (d). T_{ig}^{inf} and T_{ig}^{c} change the TTI greatly and TTI increases with increasing of T_{ig}^{inf} and T_{ig}^{c} showing in TABLE 4.3 and FIGURE 4.22 to FIGURE 4.23; (e). $STIR_{ig}^{c}$and β don't affect the TTI much as shown in FIGURE 4.20 and FIGURE 4.21.

TABLE 4.3: Sensitivity index of the input parameters

Index	Parameter Name	CC	RCC	SRC	SRRC	PCC	RPCC
1	L	-0.0413	-0.0395	-0.0787	-0.01	-0.0516	-0.0407
2	ρ	0.2288	0.2143	0.1788	0.2315	0.7903	0.8312
3	c	0.2581	0.2527	0.1901	0.2477	0.7984	0.8399
4	λ	0.2356	0.2215	0.2046	0.2542	0.8135	0.8494
5	h	-0.0274	-0.0331	-0.0504	0.0059	0.056	0.082
10	T_0	-0.0284	-0.0253	-0.0782	-0.0063	-0.0369	-0.0418
11	q_e	-0.5912	-0.5918	-0.6616	-0.6081	-0.9533	-0.9705
6	$STIR_{ig}^{c}$	-0.0717	-0.0616	-0.0727	-0.0135	-0.1243	-0.1688
7	β	0.0376	0.0471	-0.0281	0.0398	0.1602	0.2399
8	T_{ig}^{c}	0.2143	0.1826	0.1895	0.2349	0.8114	0.8659
9	T_{ig}^{inf}	0.5893	0.6077	0.5361	0.6239	0.9534	0.9617

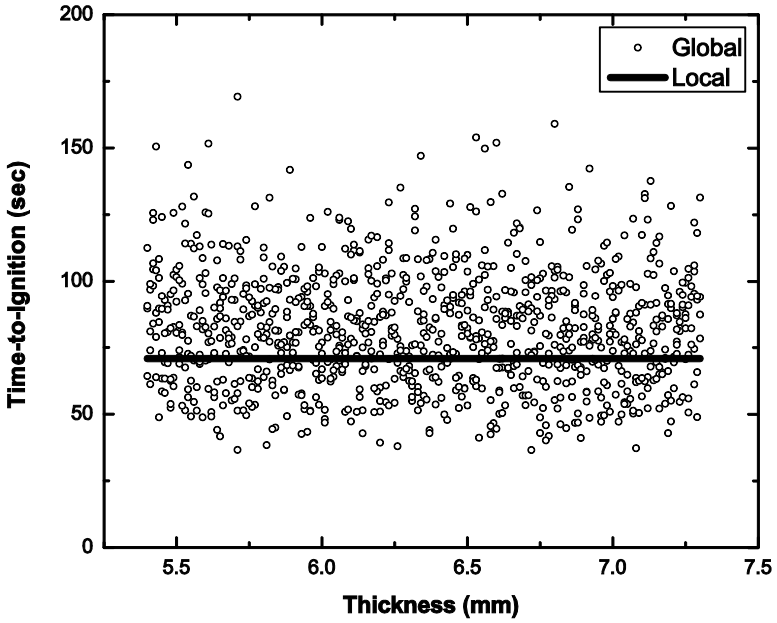

FIGURE 4.13: The effect of thickness on TTI

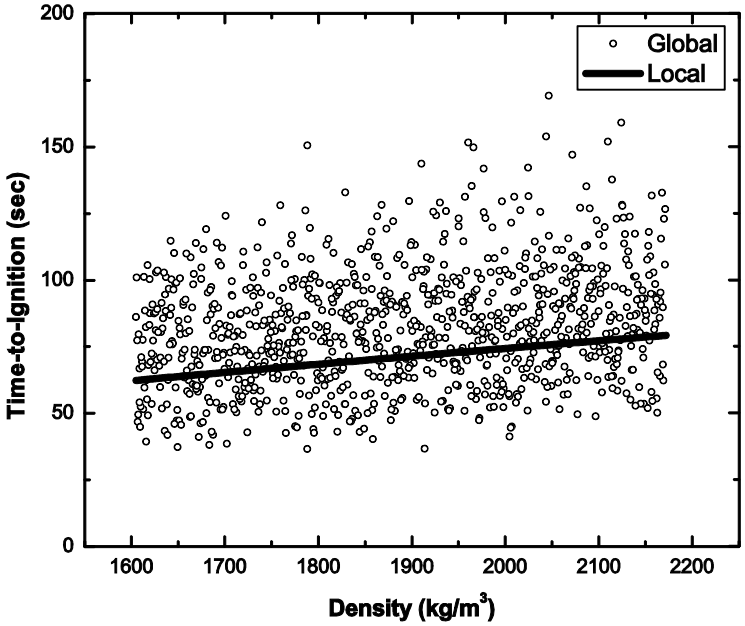

FIGURE 4.14: The effect of density on TTI

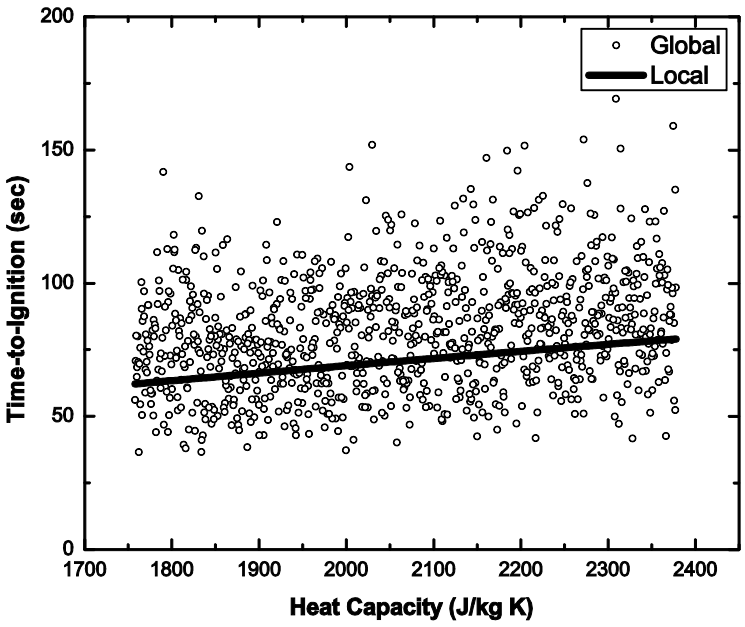

FIGURE 4.15: The effect of heat capacity on TTI

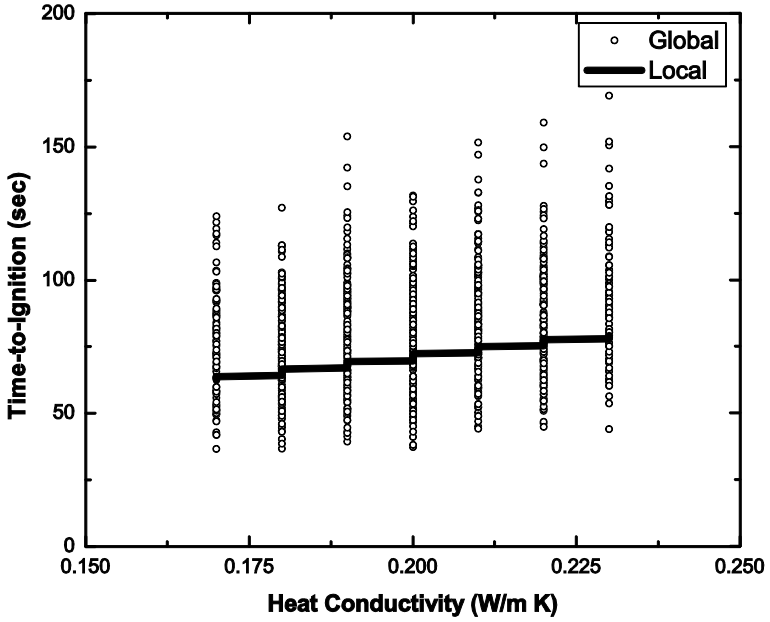

FIGURE 4.16: The effect of heat conductivity on TTI

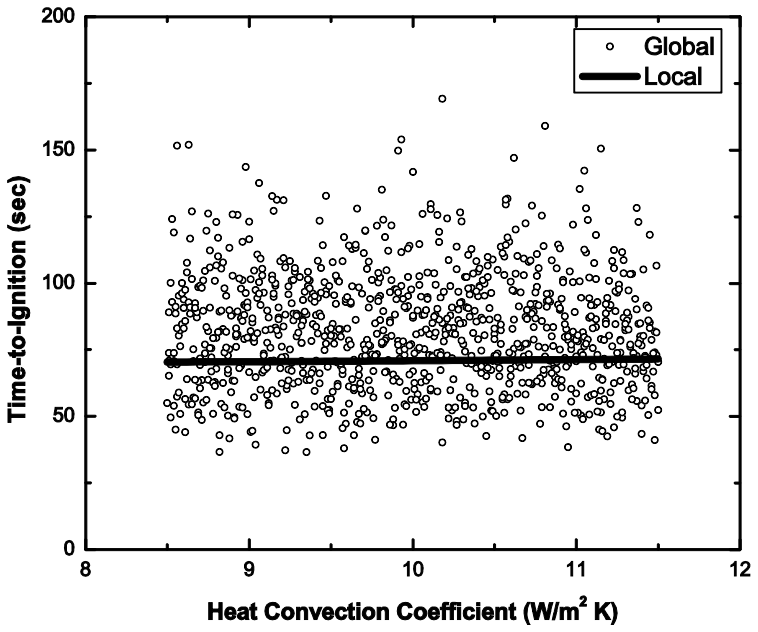

FIGURE 4.17: The effect of heat convection coefficient on TTI

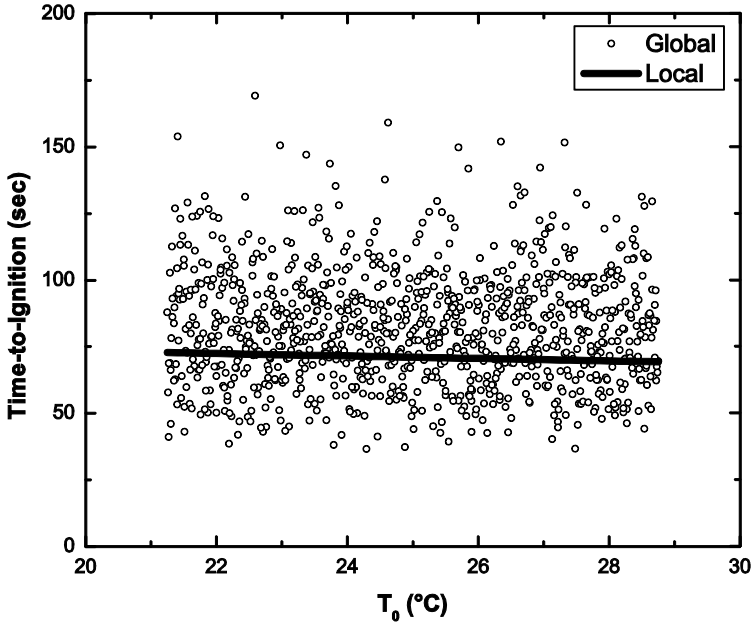

FIGURE 4.18: The effect of initial temperature on TTI

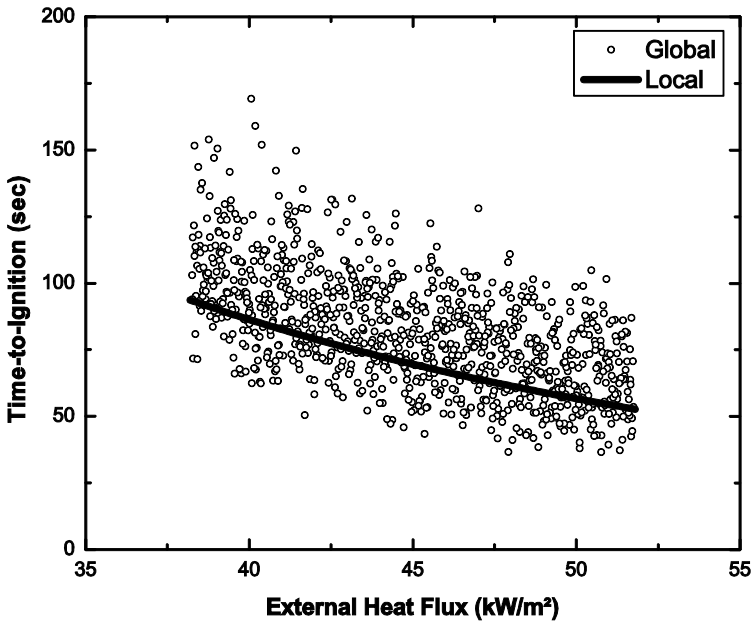

FIGURE 4.19: The effect of external heat flux on TTI

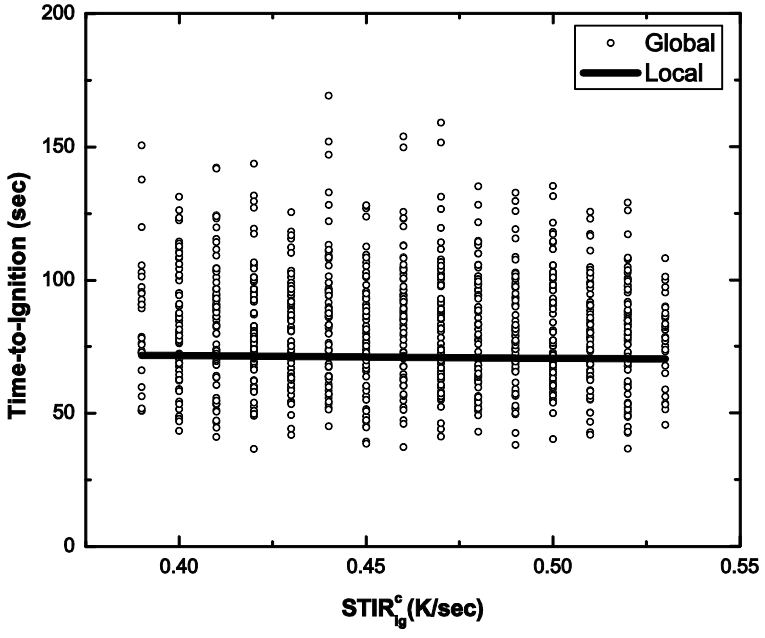

FIGURE 4.20: The effect of temperature increasing rate at critical heat flux on TTI

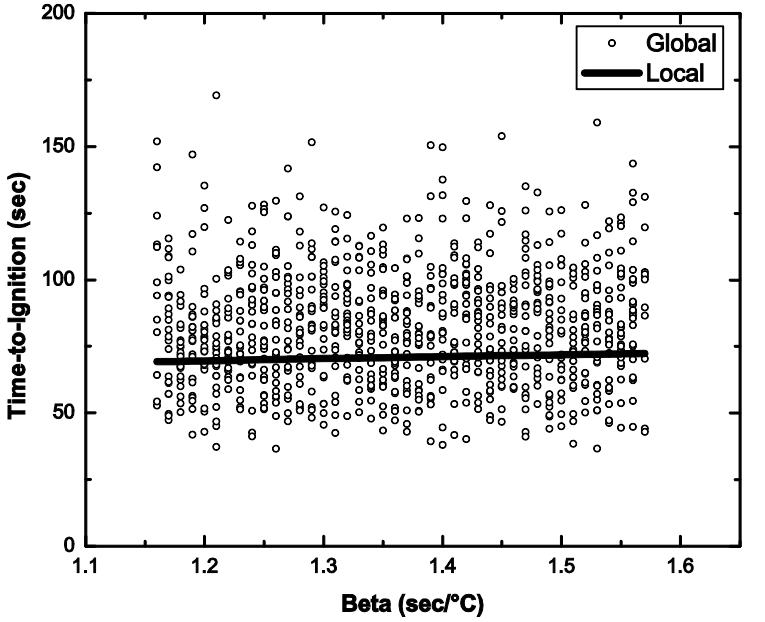

FIGURE 4.21: The effect of beta on TTI

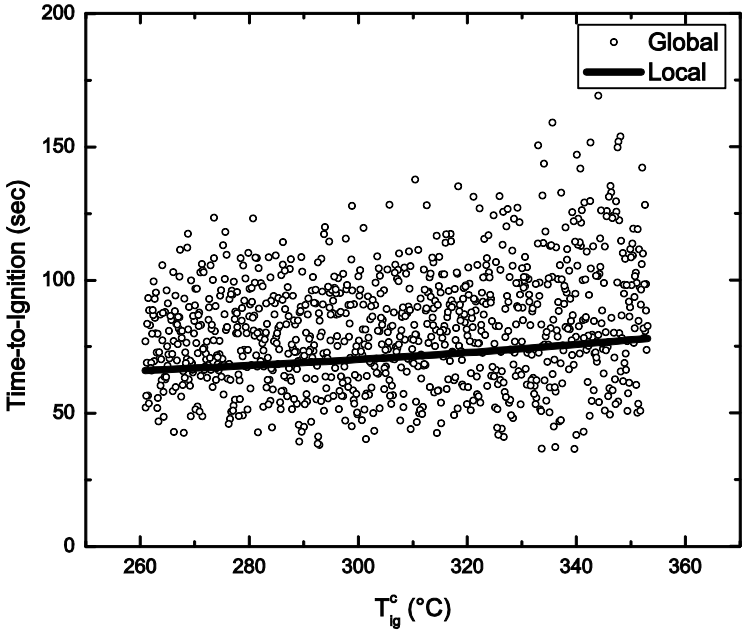

FIGURE 4.22: The effect of ignition temperature at critical heat flux on TTI

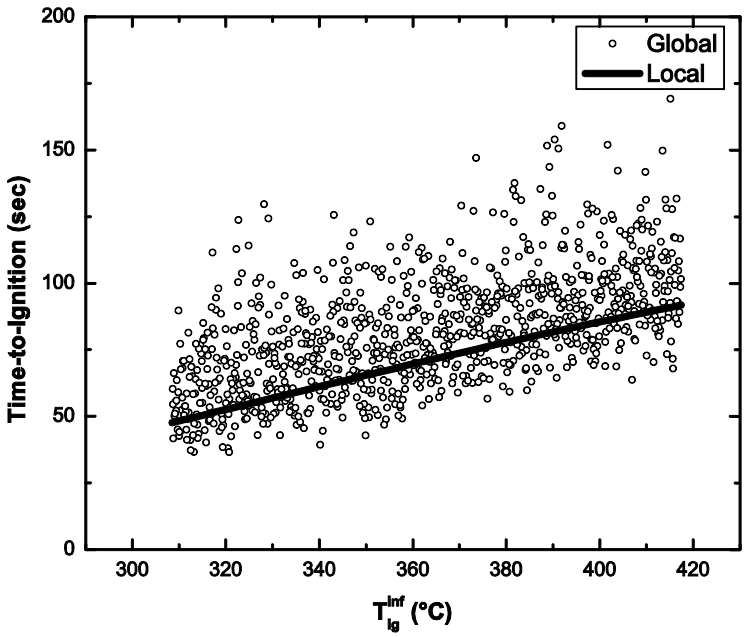

FIGURE 4.23: The effect of ignition tempratue at infinite heat flux on TTI

4.3.4. Application of Sensitivity and Uncertainty Procedures to Experimental Data

Experimental data from Mani (2011) [39] for the E-glass/polyester combustible panels (thickness from 3.175 to 12.7 mm) under heat flux from 25 to 65kw/m^2 are given in TABLE 4.4.

TABLE 4.4: Experimental data of Cone Calorimeter tests from Mani (2011)

Thickness (mm)	Time to ignition (seconds)		
	25 kW/m^2	45 kW/m^2	65 kW/m^2
3.175	125, 143, 166	44, 51, 55	24, 31, 34
6.35	164, 176, 194	78, 85, 87	34, 36, 40
12.7	299, 312, 347	85, 88, 89	40, 41, 45

Both the local and global Monte Carlo analyses are conducted according to experimental conditions and the parameters of the E-glass/polyester material as listed in TABLE 4.1 and TABLE 4.2. Since the experiment were conducted for the sample with thickness of 3.175, 6.35 and 12.7 mm, and at 25, 45 and 65kW/m^2, the thickness range is assigned as 0.1 to 15mm, and external heat flux range is 25 to 65 kW/m^2.

FIGURE 4.24 shows the CDF curve respecting to TTI. It can be seen that 80% of the ignitions will occur at the range of 34 to 150 sec. The experimental data showed 66.7% ignition happened within this range.

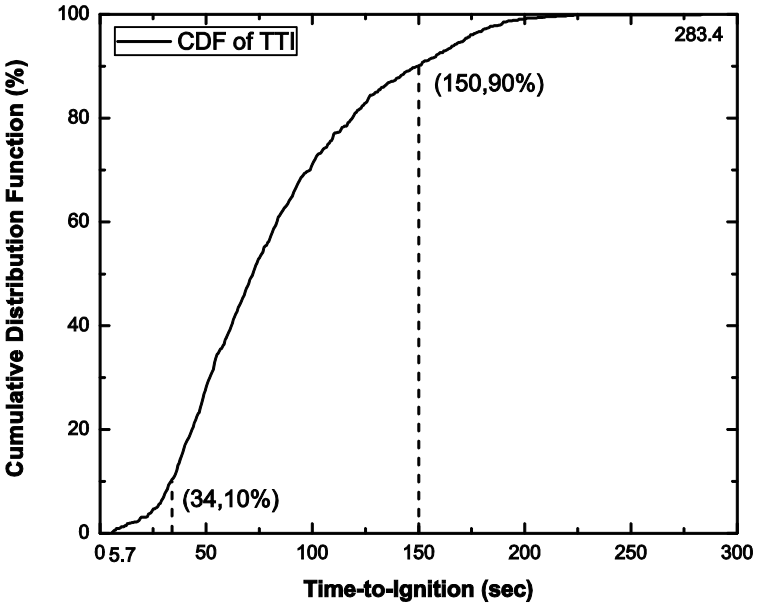

FIGURE 4.24: The CDF curve for TTI of E-glass/polyester composite

FIGURE 4.25 shows how TTI changes when thickness changes from local SA and global SA. Based on the local and global SA results, roughly when the thickness is smaller than 2.5mm, thickness is dominating factor to determine ignition. When the thickness is larger than 3.5mm, thickness hardly affects ignition. From the design point of view, the thickness range of 2.5-3.5mm can be considered as the critical thermal thickness range for this E-glass/polyester composite material, larger than which the material can be considered as thermally thick, and smaller than which the material is considered as thermally thin. Within the critical thermal thickness, the thickness may have the nonlinear relationship with TTI [20-22] (also as shown in FIGURE 4.25).

In term of the thickness choosing, the critical thermal thickness range information can be served as a guideline. For fire safety purpose, the thickness of the material is highly recommended as the maximum thickness within the critical thickness range, because of the following reasons: the critical thickness is thick enough to resist the ignition as long as possible (TTI is as long as possible); second,

after ignition, the critical thickness supplies as less fuel as possible to support the flaming.

In FIGURE 4.25, the experimental data from [39] are also shown. It can be seen that the three of experimental data are not within the ranges of the TTI. Many reasons may be responsible for this difference between experimental data and predictions, such the actually wider variations of material properties and environmental conditions variations, and etc.

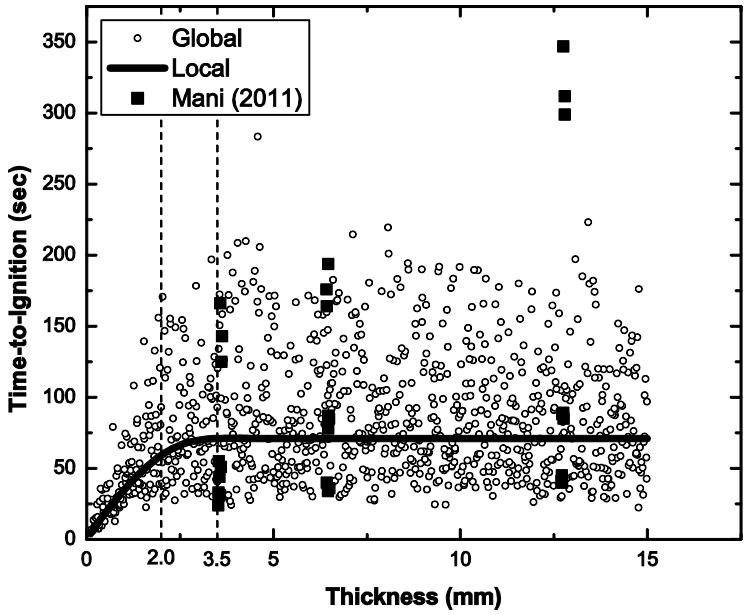

FIGURE 4.25: Predicted and experimental data of the effect of thickness on TTI

To examine our explanation why the experimental data has wider range of TTI, the most possible material property range (temperature 25°C to 300°C) and coefficients in HRIT ignition criterion are given in TABLE 4.5. The Monte Carlo simulation using LHS method is applied to integrated ignition prediction model following the same procedure above and the predicted and experimental data of the effect of thickness on TTI is shown in FIGURE 4.26. It can be seen that the prediction

model covers the range of the range of experimental data. Hence, this can be evidence for our explanation.

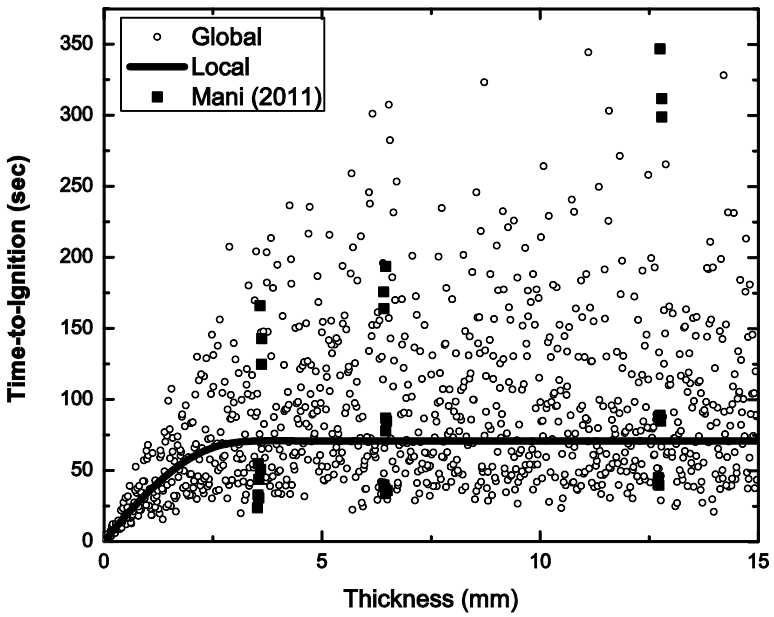

FIGURE 4.26: Predicted and experimental data of the effect of thickness on TTI with feasible variations

TABLE 4.5: The properties of E-glass/polyester composite materials

Index	Name & Unit	Symbol	Range	
1	Thickness [mm]	L	0.01	15.0
2	Density [kg/m^3]	ρ	1100	2000
3	Heat Capacity [J/(kg K)]	c	2000	2300
4	Heat Conductivity [W/m K]	λ	0.15	0.35
5	Heat Convection [W/m^2 K]	h	5	15
6	Initial Temperature [K]	T_0	25	50
7	Critical Surface Temperature Increasing Rate at ignition [K/sec]	$STIR_{ig}^{c}$	0.10	0.50
8	[sec/[°C]	β	1.00	1.50
9	Ignition Temperature at Critical Heat Flux [°C]	T_{ig}^{c}	300	320
10	Ignition Temperature at infinite Heat Flux [°C]	T_{ig}^{inf}	350	380
11	External Heat Flux [kW/m²]	$\dot{q}_e''$	25	65

In FIGURE 4.27, the external heat flux is plotted against the reverse of the square root of TTI which is a typical engineer method to analyze the ignition data. As expected, a linear relationship between external heat flux and the reverse of the square root of TTI was drawn. It can be seen in FIGURE 4.27 that the majority of the data are falling within the linear relationship. The critical thickness of the E-glass/polyester composite is around 2.5mm, and sampling thickness range is 0.1 to 15mm, hence the majority (84%) of sample points can be considered as thermally thick.

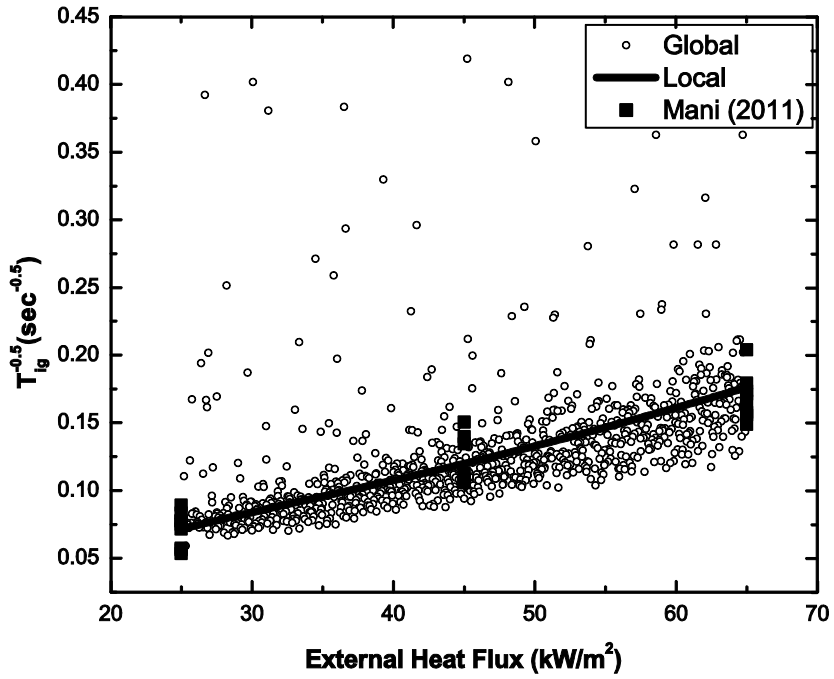

FIGURE 4.27: Prediction and experimental data of the effect of external heat flux on TTI

4.4.Conclusion

In this Chapter, sensitivity and uncertainty analysis techniques were briefly introduced and conducted on the GTT temperature prediction model, the HRIT ignition criterion, and the integrated ignition prediction model (the GTT model combined with the HRIT criterion) respectively. Based on the study of this Chapter, the following conclusions can be made:

(1) For the GTT model, external heat flux ($\dot{q}_e''$) affects the temperature and its increasing rate prediction significantly and thermal inertia parameters (ρ, c, and λ) are also important factors. Heat convection coefficient (h) and initial temperature (T_0) hardly changes GTT model prediction.

(2) For the HRIT ignition criterion, T_{ig}^{inf} and T_{ig}^{c} change the ignition zone significantly while β and $STIR_{ig}^{c}$ contribute minimal changes.

(3) For the integrated ignition prediction model, the TTI is considered as the output. The local and global Monte Carlo analyses were applied to the integrated ignition prediction model. The results show that external heat flux ($\dot{q}_e''$), T_{ig}^{inf}, T_{ig}^{c} and thermal inertia parameters (ρ, c, and λ) are important factors to affect TTI prediction. Heat convection coefficient (h), initial temperature (T_0), β and $STIR_{ig}^{c}$ have small impact on TTI. Thickness effect varies with different ranges. Thickness can be the dominating factor if the thickness is smaller than the critical thickness, and also can rarely matter when the thickness is larger than a certain value.

(4) The sensitivity and uncertainty results presented in this Chapter can serve as guideline in term of thickness choosing and experimental data evaluation or analysis for E-glass/polyester composite materials for the fire protection purpose.

CHAPTER 5: CONCLUSIONS AND FUTURE WORK

5.1. Conclusions

This research focused on the theoretical investigation of the ignition behavior of combustible solid materials.

In Chapter 2, a simplified theoretical analytical solution for predicting the temperature profile of combustible solid materials with general thermal thickness (GTT) subjected to one-sided constant heat flux was developed and it was verified and validated by experimental data of E-glass/polyester specimens in ICAL tests. Compared with the classical theoretical solutions, (such as TTK and TTN models), the GTT model is more general without the need to categorize the thermal thickness of the materials. The GTT model is valid within the whole range of thermal thickness. Its ability to predict the temperature after ignition was also shown. Since the material properties of combustible solids will change significantly after ignition, the GTT model is not recommended to predict the temperature profile after flaming ignition.

In Chapter 3, a new ignition criterion referred as the Heat Rate-related Ignition Temperature (HRIT) criterion was developed and its accuracy under the variations of external heat fluxes was validated within 8% deviation by comparing with the experimental data from thermoplastic (PMMA), thermoset (pultruded E-glass/polyester) and cellulosic material (red oak). In the HRIT criterion, the ignition temperature and its increasing rate were both used for ignition prediction. Compared with the existing ignition criteria, the HRIT criterion not only can handle the variations of external heat flux but also can deal with variation of surrounding

conditions, and meanwhile it is easy to relate to fire spread.

To identify the important factors affecting the ignition process, a comprehensive sensitivity and uncertainty analysis was conducted in Chapter 4. Sensitivity and uncertainty analysis techniques were briefly introduced. They were applied to the GTT temperature prediction model, the HRIT ignition criterion, and integrated ignition prediction model (the GTT model combined with the HRIT criterion) respectively. The following main conclusions can be made:

For the GTT model, external heat flux $\dot{q}_e''$ affects the temperature and its increasing rate prediction significantly. Thermal inertia parameters (ρ, c, and λ) are also important factors for ignition. The heat convection coefficient (h) and initial temperature (T_0) hardly changes GTT model prediction. For the HRIT ignition criterion, T_{ig}^{inf} and T_{ig}^{cr} change the ignition zone significantly while β and $STIR_{ig}^{cr}$ only contribute small changes.

For the integrated ignition prediction model, the TTI is considered as the output. The local and global Monte Carlo analyses were applied to the integrated ignition prediction model. The results showed that external heat flux ($\dot{q}_e''$), T_{ig}^{inf}, T_{ig}^{cr} and thermal inertia parameters (ρ, c, and λ) were important factors for TTI prediction. Heat convection coefficient (h), initial temperature (T_0) β and $STIR_{ig}^{cr}$ had small impact on TTI.

The importance of thickness (L) for ignition varied with different thickness ranges. It could be the dominating factor if the thickness was smaller than a certain critical thickness.

The sensitivity and uncertainty results presented in Chapter 4 can serve as a guideline in terms of choosing the correct thickness for E-glass/polyester composite materials.

5.2. Future Work

While the GTT temperature profile prediction is mathematically accurate, it is not simple enough for direct engineering applications on a day-to-day hand calculation basis. Therefore, a simplified yet accurate function approximation is preferred for engineering practice use. Future research should be undertaken to find an appropriate approximation for a simplified analytical solution of the GTT model.

As discussed in Chapter 3, the coefficients in the HRIT ignition criterion are not constant for all conditions. These coefficients will change with the moisture concentration of the material, the flow speed of the gas phase, and other factors. A systematic study of how the coefficients can be related to these factors is needed, so that the HRIT criterion can be more widely applied under various surrounding environmental conditions.

In addition, the author is interested in seeing whether this HRIT ignition can be applied for auto-ignition prediction. More experiments of the auto-ignition are needed to validate this hypothesis.

Thirdly, in the HRIT ignition criterion, both surface temperature and its increasing rate are used to determine when ignition will occur. The new HRIT criterion compared well with the available experimental data. Potentially it should be more accurate to predict fire spread. The research should be conducted to investigate whether the fire spread prediction in full scale fire simulation can be improved by using this HRIT criterion.

Another possible research area is to use the CDF curves discussed in Chapter 4, to identify the possible time-to-ignition range of real objects (e.g. furniture) in fires.

REFERENCES

[1]. ASTM, Standard Terminology of Fire Standards (E176 - 10a), 2012.

[2]. Daniel Madrzykowski DWS. Flammability Hazard of Materials. In. Flammability Hazard of Materials. Quincy, National Fire Protection Association, 2008.

[3]. Atreya A, Ignition of Fires, Philosophical Transactions: Mathematical, Physical and Engineering Sciences, 1998;356: 2787 - 813.

[4]. Babrauskas V, Ignition of Wood: A Review of the State of the Art, Journal of Fire Protection Engineering, 2002;12: 163 - 89.

[5]. The Society of Fire Protection Engineers (SFPE), The SFPE Handbook of Fire Protection Engineering (Forth Edition), National Fire Protection Association, Quincy, Massachusetts, 2008.

[6]. Babrauskas V, Ignition Handbook, Fire Science Publishers & the Society of Fire Protection Engineers, Issaquah, WA, USA, 2003.

[7]. Mouritz AP, Gibson AG, Fire Properties of Polymer Composite Materials, Springer, Dordrecht, The Netherlands, 2006.

[8]. Bamford CH, Crank J, Malan DH, The Combustion of Wood .I, Mathematical Proceedings of the Cambridge Philosophical Society, 1946;42: 166 - 82.

[9]. Kashiwagi T, A Radiative Ignition Model of a Solid Fuel, Combustion Science and Technology, 1974;8: 225-36.

[10]. Gandhi PD, Kanury AM, Criterion for Spontaneous Ignition of Radiantly Heated Organic Solids, Combustion Science and Technology, 1986;55: 233 - 54.

[11]. Zhou A, Yu Z, Validating Thermal Response Models Using Bench-scale and Intermediate-scale Fire Experiment Data, Mechanics of Advanced Materials and Structures, 2013.

[12]. Lawson DI, Simms DL, The Ignition of Wood by Radiation, Brit. J. Appl. Phys, 1952;3: 288 - 92.

[13]. Simms DL, On the Pilot Ignition of Wood by Radiation, Combustion and Flame, 1963;7: 253 - 61.

[14]. Quintiere JG, Harkleroad MF. New Concepts for Measuring Flame Spread Properties. In. New Concepts for Measuring Flame Spread Properties. 1984.

[15]. Janssens ML. Fundamental Thermophysical Characteristics of Wood and Their Role in Enclosure Fire Growth. Dissertation. Department of Flow, Heat and Combustion Mechanics, University of Gent, Belgium, 1991.

[16]. Fangrat J, Hasemi Y, Yoshida M, Hirata T, Surface temperature at ignition of wooden based slabs, Fire Safety Journal, 1996;27: 249-59.

[17]. Andrew TG, Nicholas AD, Jonathan RB, Fire Characteristics of Cored Composite Materials for Marine Use, Fire Safety Journal, 1998;30: 137-59.

[18]. Atreya A. Prolysis, ignition and fire spread on horizontal surfaces of wood. Division of Applied Sciences, Harvard University, 1983.

[19]. Theodore L. Bergman ASL, Frank P. Incropera, David P. DeWitt, Fundamentals of Heat and Mass Transfer, 2011.

[20]. Koohyar AN. Ignition of Wood by Flame Radiation. Ph.D dissertation. Univ. Oklahoma, Norman, 1967.

[21]. Mikkola E, Wichman IS, On the thermal ignition of combustible materials, Fire and Materials, 1989;14: 87-96.

[22]. Wesson HR, Welker JR, Sliepecevich CM, The Piloted Ignition of Wood by Thermal Radiation, Combustion and Flame, 1971;16: 303 - 10.

[23]. Linan A, Williams FA, Theory of Ignition of a Reactive Solid by Constant Energy Flux, Combustion Science and Technology, 1971;3: 91 - 98.

[24]. Martin S, Diffusion-controlled Ignition of Cellulosic Materials by Intense Radiant Energy, 10th Symposium (International) on Combustion,, 1965: 877 - 96.

[25]. Nelson MI, Brindley J, McIntosh A, The dependence of critical heat flux on fuel and additive properties: a critical mass flux model, Fire Safety Journal, 1995;24: 107-30.

[26]. Koohyar AN, Welker JR, Sliepcevich CM, The irradiance and ignition of wood by flame, Fire Technol, 1968;4: 284 - 91.

[27]. Rasbash DJ, Drysdale DD, Deepak D, Critical heat and mass transfer at pilot ignition and extinction of a material, Fire Safety Journal, 1986;10: 1-10.

[28]. Tewarson A, Experimental evaluation of flammability parameters of polymeric materials, Flame-Retardant Polymeric Materials, 1982;3: 97 - 153.

[29]. Drysdale DD, Thomson HE, Flammability of Plastics II: Critical Mass Flux at the Firepoint, Fire Safety Journal, 1989;14: 179-88.

[30]. Sauer FM, Ignition of Black alpha-cellusoe Papers by Thermal Radiation, Square Wave Pulse, Report AFSWP-869, 1956.

[31]. Tsai T-H, Li M-J, Shih IY, Jih R, Wong S-C, Experimental and numerical study of autoignition and pilot ignition of PMMA plates in a cone calorimeter, Combustion and Flame, 2001;124: 466-80.

[32]. Kashiwagi T, Experimental Observation of Radiative Ignition Mechanisms, Combustion and Flame, 1979;34: 231-44.

[33]. NIST, Fire Dynamics Simulator (Version 5) User's Guide, 2010.

[34]. Delichatsios MA, Flame Heights in Turbulent Wall Fires with Significant Flame Radiation, Combustion Science and Technology, 1984;39: 195-214.

[35]. Thomson HE, Drysdale DD, An Experimental Evaluation of Critical Surface Temperature as a Criterion for Piloted Igntion of Solid Fuels, Fire Safety Journal, 1988;13: 185 - 96.

[36]. Rhodes BT. Burning Rate and Flame Heat Flux for PMMA in the Cone Calorimeter. Fire Protection Engineering, University of Maryland at College Park, 1994.

[37]. Wang X, Wang X, Cui J, Wang X, Zhang J, Theoretical Calculation on the Piloted Ignition of PMMA, Journal of Macromolecular Science, Part B: Physics, 2007;46: 475-85.

[38]. Zhou YY. Computational Analysis of Pyrolysis and Ignition of Polymeric Material. Engineering Mechanical Engineering, University of California, Berkeley, Berkeley, 2001.

[39]. Mani A. Effect of Thickness on the Flammability of Pultruded Fiber. Mechanical Engineering, University of North Carolina at Charlotte, Charlotte, 2011.

[40]. Price EW, Bradely J, H. H, L. DG, Ibirigu MM, Theory of ignition of solid propellents, AIAA Journal, 1966;2: 1153.

[41]. Williams CC. Damage initiation in organic materials exposed to high intensity thermal radiation. Chemical Engineering, Massachusetts Institute of Technology, 1953.

[42]. Shen DK, Fang MX, Ignition of Wood-based materials by Thermal Radiation, International Journal on Engineering performance-based Fire Codes, 2006;8: 69 - 83.

[43]. Deverall LI, Lai W, A criterion for thermal ignition of cellulosic materials, Combustion and Flame, 1969;13: 8-12.

[44]. Lyon RE, Quintiere JG, Criteria for piloted ignition of combustible solids, Combustion and Flame, 2007;151: 551-59.

[45]. Moghtaderi B, Novozhilov V, Fletcher DF, Kent JH, A New Correlation for Bench-scale Piloted Ignition Data of Wood, Fire Safety Journal, 1997;29: 41-59.

[46]. Bilbao R, Mastral JF, Aldea ME, Ceamanos J, Betrán M, Lana JA, Experimental and theoretical study of the ignition and smoldering of wood including convective effects, Combustion and Flame, 2001;126: 1363-72.

[47]. Zhou YY, Walther DC, Fernandez-Pello AC, Numerical analysis of piloted ignition of polymeric materials, Combustion and Flame, 2002;131: 147-58.

[48]. J.C. Heltona, FJD, Latin hypercube sampling and the propagation of uncertainty in analyses of complex systems, Reliability Engineering and System Safety, 2003;81: 23-69.

[49]. Simeone Marino IBH, Christian J. Ray, Denise E. Kirschner, A methodology for performing global uncertainty and sensitivity analysis in systems biology, Journal of Theoretical Biology, 2008;254: 178-96.

[50]. Saltelli A, Chan K, Scott E, Introduction to sensitivity analysis. In: Saltelli A (ed.) Sensitivity analysis, Wiley, New York, 2004.

[51]. Kong Depeng JNvHPLSLS, A Monte Carlo analysis of the effect of heat release rate uncertainty on available safe egress time, Journal of Fire Protection Engineering;23: 5-29.

[52]. Kong D, Lu S, Feng L, Xie Q, Uncertainty and Sensitivity Analyses of Heat Fire Detector Model Based on Monte Carlo Simulation, Journal of Composite Materials, 2011.

[53]. Ramroth WT, Krysl P, Asaro RJ, Sensitivity and uncertainty analyses for FE thermal model of FRP panel exposed to fire, Composites Part A: Applied Science and Manufacturing, 2006;37: 1082-91.

[54]. Clark RE, Hope AS, Tarantola S, Gatelli D, Dennison PE, Moritz MA, Sensitivity Analysis of a Fire Spread Model in a Chaparral Landsca pe, Fire Ecology, 2008;4: 1 - 13.

[55]. International Code Council (ICC), International Building Code, International Code Council, Inc, Washington, DC, 2009.

[56]. Society of FireProtection Engineers (SFPE), SFPE Engineering Guide to Performance-Based Fire Protection (2nd edition), SFPE, Bethesda, Maryland, 2007.

[57]. Carslaw HS, Jaeger JC, Conduction of Heat in Solid, 1959.

[58]. Yu Z. Thermal and Mechanical Responses of Fiber Reinforeced Polymer Composites under One-sided Fire Expsoure. Mechanical Engineer, University of North Carolina at Charlotte, Charlotte, 2012.

[59]. Urbas J, Luebbers GE, The intermediate scale calorimeter development, Fire and Materials, 1995;19: 65-70.

[60]. American Society for Testing and Materials (ASTM),E 1623: Standard Test Method for Heat and Visible Smoke Release Rates for Materials and Products Using an Intermediate Scale Calorimeter (ICAL), 2011.

[61]. Yu Z, Zhou A, Effect of Flame Heat Flux on Thermal Response and Fire Properties of Char-Forming Composite Materials, Fire and Materials, In press.

[62]. Rich D, Lautenberger C, Torero JL, Quintiere JG, Fernandez-Pello C, Mass Flux of Combustible Solids at Piloted Ignition, Proceedings of the Combustion Institute, 2007;31: 2653-60.

[63]. Nelson MI, Brindley J, McIntosh A, Polymer Ignition, Mathematical and Computer Modelling, 1996;24: 39-46.

[64]. American Society for Testing and Materials (ASTM),E 1354-11: Standard Test Method for Heat and Visible Smoke Release Rates for Materials and Products Using an Oxygen Consumption Calorimeter, ASTM International, West Conshohocken, PA,USA, 2011.

[65]. Donald Hopkins J. Predicting the Ignition Time and Burning Rate of Thermoplastic in the Cone Calorimeter. Department of Fire Protection Engineering, University of Maryland, 1995.

[66]. Tian N, Zhou A, A Simplified Model for Predicting the Ignition of FRP Composites with Validation Using Intermediate-scale Fire Experiment Data, Fire and Materials, 2013.

[67]. Quintiere JG. Principles of Fire Behavior. In. Principles of Fire Behavior. Delmar Publishers, 1998, pp. 79.

[68]. Tran HC, White RH, Burning Rate of Solid Wood Measured in a Heat Release Rate Calorimeter, Fire and Materials, 1992;16: 197-206.

[69]. Mckay MD, Beckman FJ, Conover WJ, A Comparison of Three Methods for Selecting Values of Input Variables in the Analysis of Output From a Computer Code Technometrics, 1979;21: 239-45.

[70]. Ramroth WT, Krysl P, Asaro RJ, FE modelling of FRP sandwich panels exposed to heat: uncertainty analysis, Composites Part A: Applied Science and Manufacturing, 2006;37: 1082 - 91.

[71]. Hillen T, Leonard IE, van Roessel H, Partial Differential Equations for Engineers and Scientists, Uniersity of Alberta, 2010.

APPENDIX: ANALYTICAL SOLUTION OF GTT MODEL

Governing equation

$$\frac{\partial T}{\partial t} = \frac{\lambda}{\rho c}\frac{\partial^2 T}{\partial x^2} \tag{A.1.a}$$

with

$$T(x,0) = T_0, for\ x \geq 0, t = 0 \tag{A.1.b}$$

$$-\lambda\frac{\partial T}{\partial x} = -h_{eff}(T - T_0) + \dot{q}''(t), for\ x = 0, t > 0 \tag{A.1.c}$$

$$-\lambda\frac{\partial T}{\partial x} = h_{eff}(T - T_0), for\ x = L, t > 0 \tag{A.1.d}$$

If $T(x,t)$ is the solution of (A.1), it can be written in the form of (A.2)

$$T(x,t) = v(x,t) + \omega(x,t) \tag{A.2}$$

Let $v(x,t)$ satisfy the boundary conditions (A.1.c and A.1.d) and the second order differential of x equal to zero

$$-\lambda\frac{\partial v(0,t)}{\partial x} = -h_{eff}[v(0,t) - T_0] + \dot{q}''(t), for\ x = 0, t > 0 \tag{A.3.a}$$

$$-\lambda\frac{\partial v(L,t)}{\partial x} = h_{eff}[v(L,t) - T_0], for\ x = L, t > 0 \tag{A.3.b}$$

$$\frac{\partial^2 v}{\partial x^2} = 0, for\ all\ x \tag{A.3.c}$$

For $t \geq 0$, we can obtain the simplest possible function form of $v(x,t)$ as

$$v(x,t) = A(t) + B(t)x \tag{A.4}$$

Substitute (A.4) into (A.3.a) and (A.3.b),

$$-\lambda B(t) = -h_{eff}[A(t) - T_0] + \dot{q}''(t), for\ x = 0, t > 0 \tag{A.5.a}$$

$$-\lambda B(t) = h_{eff}[A(t) + B(t)L - T_0], for\ x = L, t > 0 \tag{A.5.b}$$

We can get

$$A(t) = T_0 + \dot{q}''(t)\left[\frac{\lambda + h_{eff}L}{h_{eff}(2\lambda + h_{eff}L)}\right] \tag{A.6.a}$$

$$B(t) = -\frac{\dot{q}''(t)}{2\lambda + h_{eff}L} \tag{A.6.b}$$

Substitute (A.6.a) and (A.6.b) into (A.4) to obtain

$$v(x,t) = T_0 + \dot{q}''(t)\left[\frac{\lambda + h_{eff}(L-x)}{h_{eff}(2\lambda + h_{eff}L)}\right] \tag{A.7}$$

Then (A.2) can be written as

$$T(x,t) = T_0 + \dot{q}''(t)\left[\frac{\lambda + h_{eff}(L-x)}{h_{eff}(2\lambda + h_{eff}L)}\right] + \omega(x,t) \tag{A.8}$$

Substitute (A.8) into (A.1),

$$\frac{\partial \omega}{\partial t} = \alpha \frac{\partial^2 \omega}{\partial x^2} + F(x,t) \tag{A.9.a}$$

with $F(x,t) = -\frac{\partial \dot{q}''(t)}{\partial t}\left[\frac{\lambda + h_{eff}(L-x)}{h_{eff}(2\lambda + h_{eff}L)}\right], \alpha = \frac{\lambda}{\rho c}$

$$\omega(x,0) = \theta(x), for\ x \geq 0, t = 0 \tag{A.9.b}$$

with $\theta(x) = -\dot{q}''(0)\left[\frac{\lambda + h_{eff}(L-x)}{h_{eff}(2\lambda + h_{\mathrm{eff}}L)}\right]$

$$\left(-\lambda \frac{\partial}{\partial x} + h_{eff}\right)\omega(0,t) = 0, for\ x = 0, t > 0 \tag{A.9.c}$$

$$\left(-\lambda \frac{\partial}{\partial x} - h_{eff}\right)\omega(L,t) = 0, for\ x = L, t > 0 \tag{A.9.d}$$

Then we get the Robin boundary condition problem for $\omega(x,t)$consisting of the nonhomogeneous partial differential equation with time-dependentsource $F(x,t)$. To solve this nonhomogeneous Equation (A.9), first we find the solution to the homogeneous problem (A.10), and then use homogeneous solutions to solve the nonhomogeneous equations.

$$\frac{\partial \omega_h}{\partial t} = \alpha \frac{\partial^2 \omega_h}{\partial x^2} \tag{A.10.a}$$

$$\omega(x,0) = \theta(x), for\ L \geq x \geq 0, t = 0 \tag{A.10.b}$$

$$\left(-\lambda \frac{\partial}{\partial x} + h_{eff}\right)\omega_h(0,t) = 0, for\ x = 0, t > 0 \tag{A.10.c}$$

$$\left(-\lambda \frac{\partial}{\partial x} - h_{eff}\right)\omega_h(L,t) = 0, for\ x = L, t > 0 \tag{A.10.d}$$

The Equation set (A.10) can be solved by the separation variable method, by assuming a solution form as Equation (A.11)

$$\omega_h(x,t) = X(x)R(t) \tag{A.11}$$

Substitute (A.11) into (A.10.a), we get

$$X(x)R'(t) = \alpha X"(x)R(t) \tag{A.12.a}$$

or

$$\frac{X"(x)}{X(x)} = \frac{R\prime(t)}{\alpha R(t)} = -\mu^2 \tag{A.12.b}$$

where μ is the separation constant or eigenvalues.

The (A.12.b) leads to the two ordinary differential equations:

$$X"(x) + \mu^2 X(x) = 0, L \geq x \geq 0 \tag{A.13.a}$$

$$-\lambda X'(0) + h_{eff}X(0) = 0 \tag{A.13.b}$$

$$\lambda X'(L) + h_{eff}X(L) = 0 \tag{A.13.c}$$

And

$$R'(t) + \alpha\mu^2 R(t) = 0, t \geq 0 \tag{A.14}$$

Equation (A.13) is a regular Sturm-Liouville problem, and the general solution [71] is

$$X(x) = C_1\cos(\mu x) + C_2\sin(\mu x) \tag{A.15}$$

Apply (A.15) into boundary conditions (A.13.b) and (A.13.c) respectively

$$-\lambda\mu C_2 + h_{eff}C_1 = 0 \; or \; \frac{C_1}{C_2} = \frac{\lambda\mu}{h_{eff}} \tag{A.16.a}$$

$$\lambda[-C_1\mu\sin(\mu L) + C_2\mu\cos(\mu L)] + h_{eff}[C_1\cos(\mu L) + C_2\sin(\mu L)] = 0 \tag{A.16.b}$$

Substitute (A.16.a) into (A.16.b), we can get

$$tan\mu L = \frac{2\lambda h_{eff}\mu}{\lambda^2\mu^2 - h_{eff}^2} \tag{A.17}$$

Assuming $C_1 = 1$ and μ_n is one of eigenvalues, the corresponding eigenfuction Equation (A.15) can be written as

$$X_n(x) = \cos(\mu_n x) + B_n \sin(\mu_n x), n \geq 1, B_n = \frac{h_{eff}}{\lambda \mu_n} \quad \text{(A.18.a)}$$

with

$$tan\mu_n L = \frac{2\lambda h_{eff}\mu_n}{\lambda^2 \mu_n^2 - h_{eff}^2} = \frac{2B_n}{1-B_n^2} \quad \text{(A.18.b)}$$

In [57] a different method to solve Equation set (A.10) was given, and properties of Equation (A.18.b) were also discussed.

Now we write the solution $\omega(x,t)$ of the nonhomogeneous problem (A.9) in terms of the eigenfuctions of the homogenous problem (A.10)

$$\omega(x,t) = \sum_{n=1}^{\infty} a_n(t) X_n(x) \quad \text{(A.19)}$$

Where $a_n(t)$ is unknown function, depending on *t*.

Since Equation (A.19) is the solution of Equation set (A.9), it must satisfy Equation set (A.9). And because $X_n(x)$ in Equation (A.19) is eigenfuction of the homogenous problem (A.10), Equation (A.19) will satisfy the boundary Equation (A.9.c) and (A.9.d) automatically. So now what we need to do here is to force solution (A.19) to fulfill Equation (A.9.a) and (A.9.b) and then solve for the unknown $a_n(t)$.

To achieve this, first substitute (A.19) into the governing Equation (A.9.a)

$$\sum_{n=1}^{\infty} \left[\frac{da_n(t)}{dt} + \alpha a_n(t)\mu_n^2\right] X_n(x) = F(x,t) \quad \text{(A.20)}$$

Next we will simplify Equation (A.20) by utilizing the orthogonality of the eigenfucitons $X_n(x)$ within the interval $[0, L]$.

Multiplying equation (A.20) by Equation (A.21)

$$X_m(x) = cos(\mu_m x) + B_m\, sin(\mu_m x) \quad \text{(A.21)}$$

and integrating both sides over x from 0 to L, the Equation (A.20) becomes Equation (A.22)

$$\int_0^L \sum_{n=1}^{\infty} \left[\frac{da_n(t)}{dt} + \alpha a_n(t)\mu_n^2\right] X_m(x)X_n(x)\,dx = \int_0^L X_m(x)F(x,t)dx \tag{A.22}$$

From orthogonality of $X_n(x)$

when $m \neq n$

$$\int_0^L X_m(x)X_n(x)dx = 0 \tag{A.23.a}$$

when $m = n$,

$$\int_0^L X_n(x)X_n(x)dx = \int_0^L [cos(\mu_n x) + B_n\, sin(\mu_n x)]^2 dx$$

$$= \frac{L}{2}(1 + B_n^2) + \frac{(1-B_n^2)}{2\mu_n} sin(\mu_n L)\, cos(\mu_n L) + \frac{B_n}{\mu_n} sin^2(\mu_n L) \tag{A.23.b}$$

To further simplify Equation (A.23.b), Equation (A.24) is given by rewriting Equation (A.18.b).

$$sin(\mu_n L) = \frac{2B_n}{1-B_n^2} cos(\mu_n L) \tag{A.24}$$

Substitute Equation (A.24) into Equation (A.23.b). Then the integral Equation (A.23.b) can be reduced to Equation (A.25)

$$\int_0^L X_n(x)X_n(x)dx = \frac{L}{2}(1 + B_n^2) + \frac{B_n}{\mu_n} \tag{A.25.a}$$

or

$$\int_0^L X_n(x)X_n(x)dx = \frac{L\left(\lambda^2\mu_n^2 + h_{eff}^2\right) + 2\lambda h_{eff}}{2\lambda^2\mu_n^2} \equiv C_n \tag{A.25.b}$$

Then Equation (A.26.a) can be obtained by substituting Equation (A.23.a) and (A.25) into Equation (A.22)

$$\frac{da_n(t)}{dt} + \alpha a_n(t)\mu_n^2 = \frac{1}{C_n}\int_0^L F(x,t)X_n(x)dx = F_n(t) \tag{A.26.a}$$

where $C_n = \frac{L\left(\lambda^2\mu_n^2 + h_{eff}^2\right) + 2\lambda h_{eff}}{2\lambda^2\mu_n^2}$

Following the Similar procedure, substitute (A.19) into initial condition (A.9.b), we can have

$$a_n(0) = \frac{1}{C_n}\int_0^L \theta(x)X_n(x)dx = \theta_n \quad \text{(A.26.b)}$$

Combine Equations (A.26.a) and (A.26.b), we get the ordinary differential Equation set (A.27) respecting to $a_n(t)$

$$\frac{da_n(t)}{dt} + a_n(t)\alpha\mu_n^2 - F_n(t) = 0 \quad \text{(A.27.a)}$$

$$a_n(0) = \theta_n \quad \text{(A.27.b)}$$

With *n=1,2,3…*

Now by solving Equation set (A.27), we can obtain the unknown terms $a_n(t)$ in Equation (A.19). To complete that, first multiply both sides of (A.27.a) by $e^{\alpha\mu_n^2 t}$,

$$\frac{d}{dt}\left[a_n(t)e^{\alpha\mu_n^2 t}\right] = e^{\alpha\mu_n^2 t}F_n(t) \quad \text{(A.28.a)}$$

Integrate both sides from *0* to *t*,

$$a_n(t)e^{\alpha\mu_n^2 t} - a_n(0) = \int_0^t e^{\alpha\mu_n^2 s}F_n(s)ds \quad \text{(A.28.b)}$$

Using initial condition (A.27.b), we can get

$$a_n(t) = \theta_n e^{-\alpha\mu_n^2 t} + \int_0^t e^{\alpha\mu_n^2(s-t)}F_n(s)\text{ds} \quad \text{(A.29)}$$

Then substitute Equation (A.29) into Equation (A.19), the solution of nonhomogeneous Equation set (A.9) can be written as Equation (A.30)

$$\omega(x,t) = \sum_{n=1}^{\infty}[\theta_n e^{-\alpha\mu_n^2 t} + \int_0^t e^{\alpha\mu_n^2(s-t)}F_n(s)ds]\left[\cos(\mu_n x) + \frac{h_{eff}}{\lambda\mu_n}\sin(\mu_n x)\right] \quad \text{(A.30)}$$

And substitute Equation (30) in Equation (A.8), finally the solution of Equation set (A.1) can be obtained as Equation (31)

$$T(x,t) = T_0 + \dot{q}''(t)\left[\frac{\lambda + h_{eff}(L-x)}{h_{eff}(2\lambda + h_{eff}L)}\right] +$$

$$\sum_{n=1}^{\infty}[\theta_n e^{-\alpha\mu_n^2 t} + \int_0^t e^{\alpha\mu_n^2(s-t)} F_n(s)ds]\left[\cos(\mu_n x) + \frac{h_{eff}}{\lambda\mu_n}\sin(\mu_n x)\right] \quad \text{(A.31.a)}$$

With

$$F_n(s) = -\frac{2\lambda}{\left[\mu_n^2\lambda^2 + h_{eff}^2\right]L + 2h_{eff}\lambda}\frac{d\dot{q}^{"}(s)}{ds} \quad \text{(A.31.b)}$$

$$\theta_n = -\frac{2\lambda}{\left[\mu_n^2\lambda^2 + h_{eff}^2\right]L + 2h_{eff}\lambda}\dot{q}^{"}(0) \quad \text{(A.31.c)}$$

$$\tan(\mu_n L) = \frac{2\lambda\mu_n h_{eff}}{\lambda^2\mu_n^2 - h_{eff}^2} \quad \text{(A.31.d)}$$

Equation (A.31.b) is simplified from Equation (A.26.a), and the simplification procedure is as following:

$$F_n(t) = \frac{1}{C_n}\int_0^L F(x,t)X_n(x)dx$$

substitute $F(x,t)$ and $X_n(x)$ as described in Equation (A.9.a) and (A.18.a)

$$= -\frac{1}{C_n}\frac{d\dot{q}^{"}(t)}{dt}\int_0^L \left[\frac{\lambda + h_{eff}(L-x)}{h_{eff}(2\lambda + h_{eff}L)}\right][\cos(\mu_n x) + B_n\sin(\mu_n x)]dx$$

$$= -\frac{1}{C_n}\frac{d\dot{q}^{"}(t)}{dt}\frac{2h_{eff}\lambda\mu_n + \mu_n h_{eff}^2 L + \lambda^2\sin(\mu_n L)\mu_n^2 - 2h_{eff}\cos(\mu_n L)\lambda\mu_n - h_{eff}^2\sin(\mu_n L)}{h_{eff}(2\lambda + h_{eff}L)\mu_n^3\lambda}$$ substitute Equation (A.24)

$$= -\frac{1}{C_n}\frac{d\dot{q}^{"}(t)}{dt}\frac{1}{\lambda\mu_n^2}$$

then substitute Equation (A.25.b)

$$= \frac{1}{\frac{L\left(\lambda^2\mu_n^2 + h_{eff}^2\right) + 2\lambda h_{eff}}{2\lambda^2\mu_n^2}}\frac{d\dot{q}^{"}(t)}{dt}\frac{1}{\lambda\mu_n^2} = -\frac{2\lambda}{\left[\mu_n^2\lambda^2 + h_{eff}^2\right]L + 2h_{eff}\lambda}\frac{d\dot{q}^{"}(t)}{dt}$$

(A.32)

Similarly, Equation (A.31.c) can be simplified from Equation (A.26.b)

$$\frac{1}{C_n}\int_0^L \theta(x)X_n(x)dx = -\frac{1}{C_n}\dot{q}''(0)\int_0^L \left[\frac{\lambda+h_{eff}(L-x)}{h_{eff}(2\lambda+h_{eff}L)}\right][\cos(\mu_n x) +$$

$B_n \sin(\mu_n x)]dx$

$$= -\frac{2\lambda}{\left[\mu_n^2\lambda^2+h_{eff}^2\right]L+2h_{eff}\lambda}\ \dot{q}''(0) \qquad \text{(A.33)}$$